

NORTHWESTERN UNIVERSITY

Processing of Superconducting Metal/MgB₂ Composites

A DISSERTATION

SUBMITTED TO THE GRADUATE SCHOOL
IN PARTIAL FULFILLMENT OF THE REQUIREMENTS

for the degree

DOCTOR OF PHILOSOPHY

Field of Materials Science and Engineering

By

John David DeFouw

EVANSTON, ILLINOIS

December 2007

© Copyright by John David DeFouw 2007

All Rights Reserved

ABSTRACT

Processing of Superconducting Metal/MgB₂ Composites

John David DeFouw

In this work, the processing of the superconductor MgB₂ was studied to create a fundamental scientific background for the production of superconducting composite wires. The synthesis of MgB₂ from Mg and B powders was investigated in situ to determine reaction rates and kinetic parameters for the application of powder-in-tube technology where powders are combined within a metal tube and drawn into a wire. A technique was developed using synchrotron x-rays to study the reaction within a tube at high temperature. To enhance powder-in-tube technology, the high temperature compressive properties of MgB₂ were measured and large ductile strains were achieved suggesting that MgB₂, despite being brittle at ambient temp can be deformed plastically at high temperature to create dense core, powder-in-tube wires.

An additional process was developed where commercial boron fibers were reacted in situ within liquid Mg, which was subsequently solidified to create a Mg matrix composite with superconducting MgB₂ fibers aligned continuously though the length. The synthesis was also studied in situ using the synchrotron technique as well as ex situ with interrupted

reactions and metallography to determine diffusion coefficients and activation energies for the formation of MgB_2 . To determine reaction mechanisms, a numerical model was developed that incorporated microstructural observations of cracking to enhance reaction rate and the model was applied successfully to the reaction of fibers.

Additional processing variables were investigated with respect to these fundamental kinetics studies including the effect of fiber diameter, surface treatment, dopant, and reaction under thermal cycling conditions. Based on these observations, future research is described where enhanced superplastic deformation of MgB_2 may be achieved along with enhanced superconducting properties, reaction mechanisms can be determined for carbon doped fibers, reaction kinetics can be determined for solid state reactions, as well as other possible developments for MgB_2 wire technology.

Acknowledgements

This research was first made possible through a first year Walter P. Murphy graduate student fellowship in Materials Science and Engineering which allowed research to proceed while proposals for continued funding were written. The bulk of the research was then funded by the National Science Foundation through a one year exploratory grant followed by full funding. Studies on reactions with doped boron were funded by an SBIR grant through the Department of Energy. Experiments performed at the Dupont-Northwestern-Dow Collaborative-Access-Team Synchrotron Research Center (DND-CAT) were supported by the E.I. DuPont de Nemours & Co., The Dow Chemical Company, the U.S. National Science Foundation through Grant DMR-9304725 and the State of Illinois through the Department of Commerce and the Board of Higher Education Grant IBHE HECA NWU 96. Use of the Advanced Photon Source was supported by the U.S. Department of Energy, Basic Energy Sciences, Office of Energy Research under Contract No. W-31-102-Eng-38.

This research was also made possible through the effort of many great minds and hands. Firstly, I would like to acknowledge my advisor, Prof. David Dunand for his guidance and always fruitful brain storming sessions. If only we had time to investigate all the research paths we discussed and if only they all worked as we would like. Secondly, I would like to acknowledge the support of my qualifying and PhD defense committee members; John Quintana, Prof. D. Lynn Johnson, Prof. David Seidman, and Prof. Scott

Barnett. I also need to recognize the work of many undergraduates including Nirand Pisutha-Arnond (NU 2002-2005), Greg LeMay (UPenn Summer 2003), Tim Lau (Cornell Summer 2004), Geok Hui Koh (NU Spring 2006), Jordan Kwok and George Scott (NU 2006-07). Doped fiber work was done in collaboration with Jim Marzik of Specialty Materials Inc.. Ben Myers expertise with SEM produced many of the great images in this text. Experiments performed at DND-CAT could not have been accomplished without the help of Denis Keane, Qing Ma, and the DND-CAT staff. Samples would not exist without the delicate handywork of Jeff and Thang in the machine shop. Finally, many praises go to Mark Seniw for his help with mechanical testing, fixing of equipment and general brainstorming to solve the most unconventional of problems.

The support of the many past and current members of the Dunand research group cannot be overlooked, especially that of Alan Brothers and Scott Oppenheimer in Cook 1021 where many of the worlds problems from science to religion were solved if we could only impose our will onto society. The 2001 Dunand group, which was full of brilliant scientists that familiarized me with the lab and high quality research, especially Dorian Balch, Chris San Marchi, Aria Kouzeli, Emmanuelle Marquis, Naomi Davis, Catherine Noble, Andrea Hodge, and Christian Fuller. This work was also supported by the interaction and great discussion with the many group members who have come and gone including Rando, Cedric, Christian, Yasu, Yoshi, Keith, Marsha, Rick, Marcus, Hipolito, Ampika, Heeman, Olivier, Ofer, Qi-zhen, Vee, Justin, Jess, Marie and Matt.

Besides those who aiding in my research efforts, I must also acknowledge all of the great friends I met while at Northwestern. We had many great times that helped ease those periods when experiments were not going so well and I thank all of your for being

there for me, especially Marko, Tammy, Ingram, Leta, Chris, Zack, Keith, Cohen, Becca, Grocholski, Rachel, Nelson, Stephan, Bmad, Scribbles, Emma, Dorian, Catherine, Naomi, Yongwoo, Dimitris, Alan, Sharon, Michelle, Neil, Aleta, Courtney, Marina, Murat, Tim, Scott, Q, James, Kristen, Mae, Tom, Jon, Julie, Bo, Melanie, Les, Andy, Harder, Lance, Blake, Eric, Ben, Justin, Michelle, Ian, Alison, Andrea, Lilliya, Sofia, Shara, Simona, Angela, Anita, Dan, Beth, Andrea, Derek, Noble, Mikey, Stacy, Andrea, Annie, Andy and Phil at Prairie Moon and of course Cindy, Salvia, and Sara.

I would also like to thank Mom, Dad, Jeff, and the rest of my family for their support even though they probably still don't know what I am doing. I also extend that thanks to all my old friends from high school and undergrad that are around the country, who have continued to provide support, and are as proud of my accomplishments as I am of theirs, especially Brian, Brad, Alex, Brent, and Winnie.

Contents

ABSTRACT	3
Acknowledgements	5
List of Figures	12
Chapter 1. Introduction	24
1.1. Properties of MgB ₂	24
1.2. Bulk Synthesis of MgB ₂	26
1.3. Macrocomposite Processing	27
1.3.1. Reactive In Situ PIT Processing	29
1.3.2. Ex Situ PIT Processing	30
1.4. Microcomposite Processing	31
1.5. MgB ₂ wires from boron fibers	33
1.6. Doping of PIT MgB ₂	35
1.7. Reaction Kinetics	36
1.8. Advancement of Scientific and Technological Research	40
Chapter 2. MgB ₂ Reaction Kinetics from Elemental Powders	42
2.1. Experimental Procedures	43
2.2. Results	46

	9
2.3. Discussion	48
2.4. Conclusions	57
Chapter 3. Compressive Ductility at High Temperature	58
3.1. Experimental Procedures	61
3.2. Results	63
3.3. Discussion	64
3.4. Conclusions	68
Chapter 4. In Situ Synthesis of Mg/MgB ₂ Fiber Composites	72
4.1. Processing	72
4.2. Characterization Procedures	73
4.3. Results and Discussion	74
4.4. Process Comparison	78
4.5. Conclusions	80
Chapter 5. Reaction Mechanisms and Kinetics of MgB ₂ Fiber Synthesis	82
5.1. Experimental Procedures	82
5.2. Results and Discussion	84
5.2.1. In Situ Reaction Kinetics	84
5.2.2. Ex Situ Reaction Kinetics Measurements	86
5.2.3. Reaction Modeling	99
5.3. Conclusions	112
Chapter 6. Processing Variable Effects on the Reaction Kinetics of MgB ₂ Fibers	114
6.1. Experimental Procedures	114

	10
6.2. Results and Discussion	115
6.2.1. Effect of Fiber Diameter	115
6.2.2. Effect of Mg Vapor	117
6.2.3. Effect of Nitrided Surface	118
6.2.4. Effect of 0.4 at% C-doping	120
6.2.5. Effect of Thermal Cycling	123
6.2.6. Broken Fibers	126
6.3. Conclusions	127
Chapter 7. Future Research	130
7.1. MgB ₂ from powder	130
7.1.1. Reactions in the solid state	130
7.1.2. Superplastic Forming	131
7.2. MgB ₂ from fibers	134
7.3. Reaction of fibers under stress	137
7.4. Improving Reaction Rates	138
7.5. MgB ₂ from liquid	139
References	141
Appendix A. Java Codes for Synchrotron Data Analysis	153
A.1. Background Subtraction	153
A.2. Combining XRD Peak Analysis Files	157
Appendix B. Carter Style Derivation of Film and Cylinder Reactions	160
B.1. Film Reaction	160

B.2. Cylinder Reaction

List of Figures

- 1.1 Scanning Electron Micrograph showing a typical powder-in-tube (PIT) processed wire produced by Wang et al [25]. 28
- 1.2 Micrograph showing lamella of Mg/MgB₂ synthesized from Mg and B powders by Ermolov et al [44]. 32
- 1.3 Mg - B thermodynamic phase diagram from Balducci et al [45]. 32
- 1.4 Image showing deformed MgB₂ fibers produced from reacting straight B fibers with Mg vapor at 950 °C taken from Canfield et al [7]. 34
- 1.5 Scanning electron micrograph showing a non-uniform front of MgB₂ formation in a B fiber from reaction with Mg vapor at 950 °C. The lighter area labeled A is MgB₂ and is located near the center as well as the edge of the fiber with isolated Mg deficient borides labeled B also shown [73]. 38
- 1.6 Normalized synchrotron diffraction intensity vs temperature plot from Baranov et al [83] showing S-shaped reaction curves for the formation of MgB₂ under a heating rate of 0.3 °C/s. 39
- 1.7 Normalized integrated intensity vs time plot from Grivel et al [84] showing MgB₂ formation before isothermal conditions were reached due to a slow heating rate of 0.06 °C/s. 40

- 2.1 Schematic of experimental set-up for in situ synchrotron x-ray diffraction experiment. A CCD camera experimental image shows MgB₂, Ti, and quartz rings. 45
- 2.2 Plots of intensity vs 2θ for example experiment where a pattern collected during heat up is used as the background for future patterns. 46
- 2.3 Scanning Electron Microscope images of (a) undoped commercial B powder with average particle size of 400 nm. Particle size analysis of SEM images show sizes range from 100 to 500 nm. (b) undoped plasma-synthesized B powder. Particle size analysis of SEM images show sizes range from 100 to 500 nm as found with the commercial powder. Inset shows particles are agglomerates of 10 to 50 nm spheres. (c) C-doped plasma-synthesized B powder. Particle size analysis of SEM images show sizes range from 100 to 500 nm as found with the commercial powder 47
- 2.4 Degree of reaction vs. time plots generated using synchrotron x-ray diffraction technique for powder compacts of Mg powder and (a) 400 nm amorphous boron powder reacted between 700 and 900 °C showing completed reaction between 10 min and 2 hours, (b) undoped plasma-synthesized powders reacted between 670 °C and 800 °C, and (c) C-doped plasma-synthesized powders reacted between 670 °C and 800 °C 49
- 2.5 Degree of reaction vs. time plots showing a linear relation to reaction time using the Carter diffusion limited reaction of spheres model

[92] for (a) un-doped commercial B powder, (b) un-doped plasma synthesized B powder, and (c) C-doped plasma synthesized B powder. Best fit lines were used to determine reaction rate constant k .

52

2.6 MgB₂ thickness data vs time at 800 °C from Kim et al [74] fitted with planar reaction equation to determine the reaction rate constant k . The rate constant was $4.8 \cdot 10^{-17} m^2/s$ which compared well with powder reactions at 800 °C.

53

2.7 Arrhenius plot of reaction rate constants k vs. inverse temperature showing activation energy for un-doped commercial, un-doped plasma-synthesized, and C-doped plasma-synthesized B powders. A data point from a thin film experiment [74] (Figure 2.6) is shown for comparison.

54

2.8 Scaled diffusion thickness vs. time plots with fits of the Entchev sphere reaction model [94] with $z = 1$ and diffusion coefficient D as the fitting parameter for (a) un-doped commercial B powder, (b) un-doped plasma synthesized B powder, and (c) C-doped plasma synthesized B powder.

55

2.9 Arrhenius plot of diffusion coefficients D vs. inverse temperature showing activation energy for un-doped commercial, un-doped plasma-synthesized, and C-doped plasma-synthesized B powders. A data point from a thin film experiment [74] is shown for comparison.

56

- 3.1 Plot of melting temperature vs Gibbs free energy of formation for AlB_2 type borides showing linear relationship used to estimate an MgB_2 melting temperature of 2307 K. 60
- 3.2 Stress vs Strain plot of 950 °C data at a strain rate of $4.3 \times 10^{-5} \text{ s}^{-1}$ showing $\sigma = \sigma_0 - b\epsilon$ equation fit to data for determination of flow stress in cases where the stress does not reach a slope of 0. Here the flow stress was determined to be 99 MPa although the data did not level off at that value. 62
- 3.3 Optical micrographs showing as-HIP'd commercial MgB_2 powders. (a) shows dense microstructure with arrows indicating a few small pores. (b) shows fine grain microstructure under cross-polarized light. 63
- 3.4 HIP'd MgB_2 true compressive stress vs true strain plots of multiple strain rates at (a) 900 °C, (b) 950 °C and (c-d) 1000 °C with (d) showing 0.41 true strain at 1000 °C and a strain rate of $6.9 \times 10^{-4} \text{ s}^{-1}$. 65
- 3.5 Images of HIP'd MgB_2 (a) before and (b-c) after 41% compressive strain at 1000 °C and a strain rate of $6.9 \times 10^{-4} \text{ s}^{-1}$ with arrow indicating plastic crack formed during testing. 66
- 3.6 Plot of strain rate vs stress in double logarithm diagram showing stress exponents between 1.0 and 1.8 during constant strain rate creep experiments between 900 °C and 1000 °C. 67
- 3.7 Optical micrographs showing fine grained MgB_2 microstructure after compressive creep testing at (a) 900 °C and (b) 1000 °C. 68

- 3.8 Plot of XRD patterns for as-received, as-HIP'd and creep tested MgB_2 showing some MgO in the tested samples and a few other unknown peaks likely contamination from powder preparation but not MgB_7 or MgB_4 . 69
- 3.9 Plot of Strain Rate vs Stress in log space showing lines of predicted relationships based on the parameter fits of $n = 1.36$, $Q = 241 \text{ kJ/mol}$, and $A = 1.34 \times 10^{-5} \text{ m}\cdot\text{s}/\text{kg}$ along with experimental data between $900 \text{ }^\circ\text{C}$ and $1000 \text{ }^\circ\text{C}$. 70
- 4.1 Scanning electron micrographs showing shape and morphology of infiltrated B fibers before and after heat-treatment. (a), Un-reacted composite showing magnesium matrix with $140 \text{ }\mu\text{m}$ diameter B fibers. (b), Reacted composite showing a $193 \text{ }\mu\text{m}$ diameter MgB_2 fiber in Mg matrix, with radial cracks infiltrated with Mg. (c), Deep-etched reacted composite showing parallel, cylindrical MgB_2 fibers with radial cracks. (d), Reacted fiber near iron crucible wall with (i) MgB_2 , (ii) un-reacted B, and (iii, iv) two Fe-Mg-B phases with various amounts of Mg. 76
- 4.2 Magnetic moment vs. temperature under zero field conditions for single MgB_2 fiber extracted from the reacted composite. Inset shows T_c slightly above 39 K . 77
- 4.3 Optical micrograph of $200 \text{ }\mu\text{m}$ MgB_2 fiber in Mg matrix under cross-polarized light. Arrows indicate slivers of non-birefringent

material (MgB_4). A $15 \mu\text{m}$ W-B core is located at the center of the MgB_2 fiber. The interface between the matrix and fiber is well bonded.

78

- 4.4 SIMS elemental maps in reacted composite. (a), Total ion image. (b), Mg ion image, showing Mg in both matrix and fibers (except fiber cores). (c), B ion image, showing B exclusively within the fibers (and fiber cores). (d), W ion image, showing fiber cores. 79
- 5.1 Synchrotron x-ray diffraction degree of reaction vs time curves for $140 \mu\text{m}$ diameter B fibers reacted in situ in liquid Mg. 85
- 5.2 Fits of Carter cylinder model (Equation (5.1)) to in situ synchrotron data with (a) showing fits to the data after removal of incubation data and (b) showing fits to the middle most linear section of reaction curves. 87
- 5.3 Arrhenius style plot of reaction rate constants vs inverse temperature showing activation energies between 106 and 180 kJ/mol. 88
- 5.4 Optical micrographs of fibers reacted at $1000 \text{ }^\circ\text{C}$ for (a) 1 min, (b) 2 min, (c) 3 min, and (d) 5 min showing MgB_2 , MgB_4 , and MgB_7 growth fronts as indicated by white arrows. The blue arrow highlights a crack in the MgB_2 infiltrated by Mg with the red arrow indicating a fiber crack not due to reaction but likely from sectioning or metallographic preparation. 90

- 5.5 Optical micrographs of fibers reacted at 900 °C for (a) 15, (b) 40, (c) 60, and (d) 100 min showing MgB₂, MgB₄, and MgB₇ growth fronts. 91
- 5.6 Optical micrographs of fibers reacted at 800 °C for (a) 1, (b) 2, (c) 3, (d) 4, and (e) 5 days showing only MgB₂ and MgB₇ growth fronts. 92
- 5.7 Optical micrographs of fibers reacted at 700 °C for (a) 21, (b) 54, and (c) 123 days showing only MgB₂ and MgB₇ growth fronts. 92
- 5.8 Fits of Entchev model [94] for reaction of a cylinder to ex situ thickness measurements of boride growth fronts on fibers reacted at 1000 °C. 94
- 5.9 Fits of Entchev model [94] for reaction of a cylinder to ex situ thickness measurements of boride growth fronts on fibers reacted at 900°C. 95
- 5.10 Fits of Entchev model [94] for reaction of a cylinder to ex situ thickness measurements of boride growth fronts on fibers reacted at 800 °C. 96
- 5.11 Fits of Entchev model [94] for reaction of a cylinder to ex situ thickness measurements of boride growth fronts on fibers reacted at 700 °C. 96
- 5.12 Arrhenius style plot of diffusion coefficients vs inverse temperature for the growth fronts of MgB₂, MgB₄, and MgB₇ showing activation energies of 362 kJ/mol, 477 kJ/mol, and 319 kJ/mol respectively. 97

- 5.13 Plots of Carter cylinder derivation (Equation (5.1)) for $-kt$ vs time for ex situ thickness measurements on interrupted reactions of B fibers at 700 - 1000 °C. 99
- 5.14 Arrhenius plot of Carter cylinder derivation fit of reaction rate constant k vs inverse temperature for ex situ MgB_2 thickness measurements on interrupted reactions of B fibers at 700 - 1000 °C showing activation energy of 360 kJ/mol. 100
- 5.15 Predicted reaction curves using measured diffusion coefficients and Entchev cylinder reaction model [94] showing reaction times much longer than observed experimentally. 101
- 5.16 Schematics describing reaction model design where the amount of MgB_2 reacted depends on the growth front of MgB_4 where MgB_2 wedges will grow into cracks in the MgB_4 region as well as the MgB_2 growth front from diffusion through the product layer on the outside of the fiber. 103
- 5.17 Drawings showing geometric parameters used for the calculation of degree of reaction vs time curves given the diffusion coefficients for the growth fronts of MgB_2 and MgB_4 and the number of cracks, N . 104
- 5.18 Plots of model output degree of reaction vs time showing contributions of shell and wedge reactions where (a) shows wedge reaction dominating the total reaction with 30 cracks per fiber and (b) showing the more significant contribution of the shell reaction as

- well as a kink in the wedge reaction curve corresponding to when the wedge reaches the center of the fiber for 7 cracks per fiber. 105
- 5.19 Optical micrograph showing wedges reaching center of fiber given 50% reaction at 1000 °C for 20 min. 106
- 5.20 Plots of model output showing the effect of cracks on reaction time. (a) shows the effect of cracks with diffusion coefficients at 900 °C on degree of reaction, (b) shows the effect of cracks with diffusion coefficients at 1000 °C on degree of reaction, and (c) and (d) showing exponential relationship between the reaction time and number of cracks. 107
- 5.21 Plots of model output degree of reaction vs time showing effect of diffusion coefficient within uncertainty determined from thickness measurements on the reaction rate of B fibers in liquid Mg. 108
- 5.22 Plots of model output showing the effect of individual diffusion coefficients of MgB_2 and MgB_4 showing that the diffusion coefficient of MgB_4 controls the initial reaction rate and the MgB_2 controls the final reaction rate after wedges reach the center of fibers. 109
- 5.23 Model fits of diffusion coefficients and number of cracks to experimental in situ data from Figure 5.1. 110
- 5.24 Optical micrograph showing unreacted slivers of MgB_4 near end of reaction which does not correlate to the 20-30 cracks seen early in reactions. 111

- 5.25 Illustration of 9 non uniformly distributed cracks merging into 3 wedge regions showing short distances between cracks reacting quickly to form the merged wedge with large distances between cracks remaining. 111
- 5.26 Fit of adjusted model where 50% of fiber reacted by cracks to experimental in situ data to simulate the effect of cracks merging during the reaction of fibers. 112
- 6.1 Sample temperature vs time plot showing two cycles for reactions under thermal cycling conditions. 116
- 6.2 Degree of reaction vs time plot for 100 μm B fibers reacted in liquid Mg between 900 and 1000 $^{\circ}\text{C}$ with diffusion and cracking model fits using diffusion coefficients within the uncertainty measured in Chapter 5. 118
- 6.3 Optical micrograph showing 100 μm B fibers reacted for 3 min at 1000 $^{\circ}\text{C}$. 119
- 6.4 Degree of reaction vs time showing reactions of 100 μm B fibers reacted between 900 and 1000 $^{\circ}\text{C}$ in Mg vapor (closed symbols) compared to fibers reacted in Mg liquid (open symbols). 120
- 6.5 Degree of reaction vs time plots showing 140 μm B fibers with nitrided surface reacted between 900 and 1000 $^{\circ}\text{C}$ in Mg liquid. 121
- 6.6 Scanning electron micrographs showing (a) 140 μm B fiber with lighter shaded nitride ring on the outer edge of the fiber. (b) shows a

- higher magnification image of the nitride layer that was determined to be 1.8 - 2.2 μm thick. 122
- 6.7 Optical micrographs showing 0.4 *at%* C-doped 85 μm B fibers reacted in Mg liquid at 1000 °C for (a) 5 min, (b) 2.5 h, and (c) 16.5 h. 122
- 6.8 Measured MgB_2 thickness vs time for 85 μm C-doped B fibers reacted in liquid Mg at 1000 °C. Lines show poor fits of Entchev et al [94] cylinder reaction model. 124
- 6.9 Degree of reaction vs time plots showing 140 μm B fibers reacted under thermally cycled conditions compared to isothermal reaction at 900 °C where thermal cycling enhanced cracking and reduced the reaction time. 125
- 6.10 Degree of reaction vs time plots comparing different thermal cycling conditions. (a) shows the effect of cycle amplitude (ΔT) on reaction and (b) shows the effect of cycle time on the reaction. 126
- 6.11 Degree of reaction vs time plot showing 100 μm diameter B fibers that were ground and sieved to 25 - 45 μm and reacted at 900 °C. Reactions of unbroken 140 μm diameter cylindrical B fibers and 400 nm B powders are shown for comparison. 127
- 6.12 Degree of reaction vs time plot using data converted to the Carter sphere model [92] where the slope is related to the reaction rate constant k . 128

- 6.13 Optical micrograph of large crystalline B powders (60 - 140 μm) reacted with liquid Mg at 800 $^{\circ}\text{C}$ for 2 h with arrows indicating regions where MgB_2 grew into cracked regions of a single particle. 128
- 7.1 Needle shaped tip (circled) of MgB_2 created by dual beam FIB of a section of a 190 μm MgB_2 fiber. 136
- 7.2 Optical micrograph showing microstructure of Cu-Mg-B melt quenched from 1200 $^{\circ}\text{C}$ determined by XRD to be a copper alloy matrix with MgB_4 and MgB_7 precipitates. 140

CHAPTER 1

Introduction

In this chapter, the fundamental science and technical research of superconducting MgB_2 is reviewed to provide a basis of knowledge to understand the field that is relevant for the following chapters. The field of MgB_2 superconductivity is only 6 years old but has moved very fast in both the physics behind the properties as well as advancement of properties based upon this knowledge. References are provided for readers who desire a more detailed background.

1.1. Properties of MgB_2

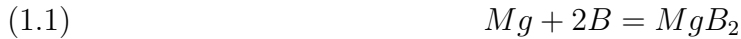
The discovery of superconductivity near 39 K in magnesium diboride (MgB_2) in January 2001 [1] has initiated range of research into scientific and technical merit of this discovery. The transition temperature of 39 K was well above that of previously known binary intermetallic superconducting compounds (NbTi : 10 K, Nb_3Sn : 18 K, and Nb_3Ge : 23 K), which remain to date the workhorse alloys for superconducting magnets for medical imaging. Several studies investigated the source of this unusually high transition temperature. It was found that MgB_2 followed traditional BCS type superconductivity theories when experiments showed that lighter boron isotopes led to a higher transition temperature. [2] Although, MgB_2 appeared very traditional at first compared to still-unexplained superconducting behavior in cuprate type compounds, later experiments showed the existence of two superconducting band gaps that contribute to the overall

transition temperature. [3, 4] Though research continues, the scientific understanding of MgB₂'s superconducting mechanisms is fairly well known with the science and synthesis of improved MgB₂ films and wires driving most of the current engineering studies.

From an engineering point of view, MgB₂ is of interest due to its relatively high superconducting transition temperature which makes practical use near 20 K feasible with liquid hydrogen, neon, or thermoelectric refrigeration. It is a chemically simple binary compound made up of inexpensive, non-toxic and abundant elements. The compound itself is lightweight with a density of 2.62 g/cc [5]. It has been shown to have a low normal state resistivity (10 $\mu\Omega$ cm, RT) [6] in pure forms [6, 7] comparable to bulk Cu (1.7 $\mu\Omega$ cm, RT) [8]. Unlike the cuprates, grain boundaries in MgB₂ act as pinning sites for superconducting fluxes and do not inhibit superconducting current flow [9, 10]. In simple forms, MgB₂ is also easy to synthesize by merely exposing any film, wire, or powder of boron to magnesium vapor. MgB₂ has also responded to engineering its performance with improvements in important properties such as the critical current density by incorporating more grain boundaries or impurities to pin the flux vortices as well as increasing upper critical field by creating point defects in substituting for B in the crystal lattice. In response to the advantages of MgB₂, several groups have sought to create high quality MgB₂ in bulk, wire, and thin film form for research and potential current carrying applications such as power transmission and superconducting magnets for medical imaging, particle accelerators, motors, or magnetic levitation [11].

1.2. Bulk Synthesis of MgB₂

The most common processing method for the production of magnesium diboride is through the reaction of magnesium and boron powders or pieces (typically between 600 and 1000 °C) according to the equation



The reactive processing of bulk MgB₂ can be done under elevated or ambient pressure. Difficulties arise due to the high vapor pressure of magnesium at these temperatures (T_m = 650 °C, T_b = 1100 °C). This and the negative volume change that occurs when Mg and B react (24% [12]) often results in a porous material without pressure assistance. Bulk synthesis studies generally attempt to optimize the superconducting properties with different time, temperature and pressure.

Those who discovered the superconducting properties of MgB₂ manufactured the material through reacting a mixture of magnesium powder and amorphous boron powders at 700 °C for 10 h under an isostatic pressure of 196 MPa [1]. This material had a superconducting transition temperature of 39 K. Several studies have attempted to improve this processing route, both through improving superconducting properties such as transition temperature and critical current density and through improving ease of fabrication. Some methods have used ambient pressure at temperatures between 650 and 950 °C which would be an easier and cheaper fabrication method [13]. Others have improved properties by reducing porosity using hot deformation between 700 C [14] and 900 °C [15]. Hot pressing at 700 °C up to 640 MPa resulted in 80% density achieved [14]. Temperatures as low as 450 °C for ball milled Mg + B powders [16] and as high as 1400 C [17] have been

used to fabricate bulk MgB_2 . Systematic studies of bulk in situ MgB_2 synthesis show best results for critical current density at low synthesis temperatures, i.e. $550\text{ }^\circ\text{C}$ for 1200 hr, due to the small grain size associated with reacting at low temperatures. [18] Studies comparing $600\text{ }^\circ\text{C}$ and $850\text{ }^\circ\text{C}$ reactions reported the same findings with improvements in upper critical field and critical current density for solid state reactions [19].

Non-reactive processing of bulk MgB_2 utilizes commercial powders or the material formed in the above methods as a starting powder followed by a densification step. A simple hot isostatic pressing of MgB_2 powder under 100 MPa argon gas at $950\text{ }^\circ\text{C}$ produced a MgB_2 sample with a density of 2.63 g/cc , critical current density of 10^6 A/cm^2 , and a transition temperature of 37 K [20]. Temperatures from 775 to $1000\text{ }^\circ\text{C}$ at pressures up to 3.5 GPa [21] as well as milled and unmilled MgB_2 starting powders [22] have also been studied. Milled powders were believed to produce a more homogeneous product [23] and higher temperatures such as $1000\text{ }^\circ\text{C}$ were shown to produce better superconducting properties than lower temperatures given the same pressure conditions [21, 22]. Densification at very high temperatures ($1250\text{ }^\circ\text{C}$) resulted in a microstructure that did not resemble the typical MgB_2 [21]. Systematically, densification at 3 GPa improved grain connectivity as shown by SEM and superconducting transition as temperature increased from 500 to $800\text{ }^\circ\text{C}$ with $950\text{ }^\circ\text{C}$ also showing results comparable to $800\text{ }^\circ\text{C}$ [24].

1.3. Macrocomposite Processing

Since MgB_2 is a ceramic and continuous wires or tapes are needed for most applications, some advanced processing method is needed to create wires besides the drawing of bulk MgB_2 , which is impossible at room temperature due to its brittleness. Wires

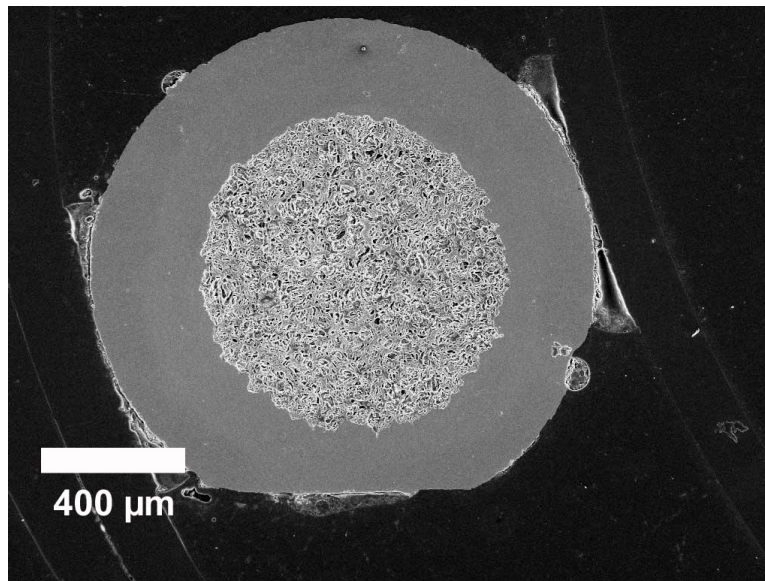


Figure 1.1. Scanning Electron Micrograph showing a typical powder-in-tube (PIT) processed wire produced by Wang et al [25].

of MgB_2 are most commonly produced through the powder-in-tube (PIT) method originally developed for cuprate based superconductors such as Bi(Pb)-Sr-Ca-Cu-O (BSCCO). This method can include both reactive and non-reactive routes. Reactive routes involve combining stoichiometric mixtures of magnesium and boron powders in a metal tube, mechanically deforming the tube into a wire, and then using a high temperature heat-treatment to form a MgB_2 core within a metal sheath [25] (Figure 1.1). Non-reactive processing methods pack MgB_2 powders in a metal tube, deform it into a wire, and then sinter the MgB_2 at high temperature. Typical deformation involves drawing a 10 mm tube filled with powder down to about 1-2 mm [25].

1.3.1. Reactive In Situ PIT Processing

Although ex situ PIT produces high performance MgB_2 wires with minimal processing, similarly processed in situ PIT has proved to achieve higher critical currents in higher magnetic fields [26, 27]. Most reactive (in situ) PIT processing involves selecting the appropriate starting powders and metal sheath material in terms of mechanical properties and chemical stability and optimizing the heat-treatments. Heat-treatments have been compared between metal sheaths of silver, copper, and iron with the optimum heat-treatment dependent on limiting the reaction between the sheath and Mg or B [12]. Often, a more desirable sheath metal (such as Cu) easily reacts with Mg or B to form undesirable phases (such as Cu_2Mg). This type of reaction can be prevented by a diffusion barrier such as Nb or Ta [28]. Iron or steel are the most studied sheaths since there is little reaction with Mg and B and it is also fairly inexpensive. Best results have been shown for composite sheaths such as Nb/Cu/Stainless Steel where the Nb is the least reactive with MgB_2 , Cu adds thermal and electrical stability, and stainless steel provides mechanical strength and compresses the MgB_2 during cooling from the reaction step which improves properties [29]. Reactive PIT heat-treatments have ranged from 600 to 1000 °C and from 3 min to 48 h [25, 30, 31]. No systematic correlation was shown between heat-treatment time and properties. The short 3 min heat-treatments were as good as any of the long treatments.

In situ MgB_2 PIT conductors have also been improved by modifications of the Mg. Commercial Mg is heavily oxidized and this oxidation is believed to reduce grain connectivity when reacting boron to MgB_2 [32]. Thermal plasma melting of Mg creates nanoscale Mg powder that has shown to improve critical current and upper critical field

capability of MgB_2 due to improved grain connectivity [32, 33]. A similar effect is shown by reaction with MgH_2 according to the equation



where the H_2 was shown to evolve and diffuse out of tubes around 500 °C leaving pure Mg to react with B [34–36, 36]. However, this reaction creates an even more porous microstructure due to a volume contraction of 40% [37].

1.3.2. Ex Situ PIT Processing

As discussed, non-reactive (ex situ) PIT processing packs MgB_2 powder into tubes, deforms the tubes into wires and sometimes provides a heat-treatment to help sinter the powder. Similar to reactive in situ PIT, ex situ PIT research often involves studying the effects of different sheath materials in terms of the reaction with the MgB_2 and also the extent of deformation on the MgB_2 and the resulting effects on properties. Different tube drawing deformation methods effect the transition temperature and critical current density of the MgB_2 wire [38]. Two axial rolling was found to be the best mode of deformation compared to drawing and rotary swaging [39]. Increased sheath strength improved MgB_2 properties in PIT wires since more of the deformation stress was transferred to the MgB_2 further densifying the powders [40]. The goal of these procedures is to reduce the porosity between MgB_2 powders and increase grain connectivity. An additional 30 min, 200 MPa and 900 °C HIP treatment after drawing can accomplish this and results in critical current densities on the order of $10^6 A/cm^2$ [41]. Critical current densities of as deformed

PIT MgB₂ without additional heat treatments exceed $10^5 A/cm^2$ [40, 42] at 4.2 K and 0 T.

1.4. Microcomposite Processing

Besides the powder-in-tube method, another method used to increase toughness of MgB₂ consists of creating an MgB₂ composite with a percolating ductile metal. One processing route to an MgB₂ composite was to combine MgB₂ powder with 11 vol% Al powder [43]. The powder mixture was pressed into pellets and vacuum sintered at 320 °C. The resulting critical temperature was 37.5 K. It was observed that the addition of aluminum broadened the superconducting temperature transition width (an indication of impurities) but did not impede superconductivity as measured by a magnetometer. No microstructural effects, mechanical properties, or reactions between the aluminum and MgB₂ were discussed. A composite of magnesium and MgB₂ was also investigated, but for use as a sputtering target [44](Figure 1.2). For the sputtering target, magnesium and boron powders were stoichiometrically mixed and compacted. A magnesium plate was placed on the powder compact and both were heated to 900 °C in a vacuum induction furnace for 30 min under several atmospheres of argon gas pressure. The sputtering target exhibited a structure consisting of lamella of magnesium within the reacted MgB₂. According to the phase diagram [45] (Figure 1.3), Mg is in thermodynamic equilibrium with MgB₂ so no additional phases formed. Since it was used as a sputtering target only, no superconductivity measurements were made.

An MgB₂/Mg nanocomposite was created by chemical vapor infiltration of a pressed submicrometer boron powder perform with Mg in a gradient furnace where the Mg vapor

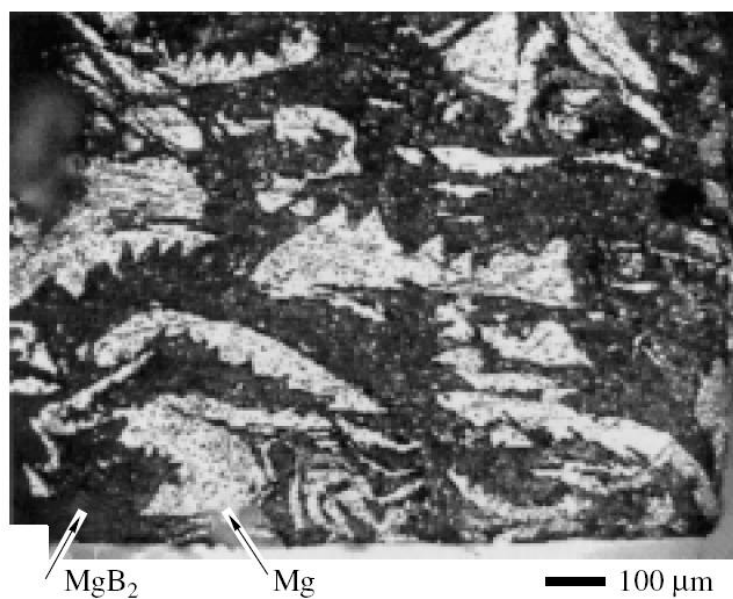


Figure 1.2. Micrograph showing lamella of Mg/MgB₂ synthesized from Mg and B powders by Ermolov et al [44].

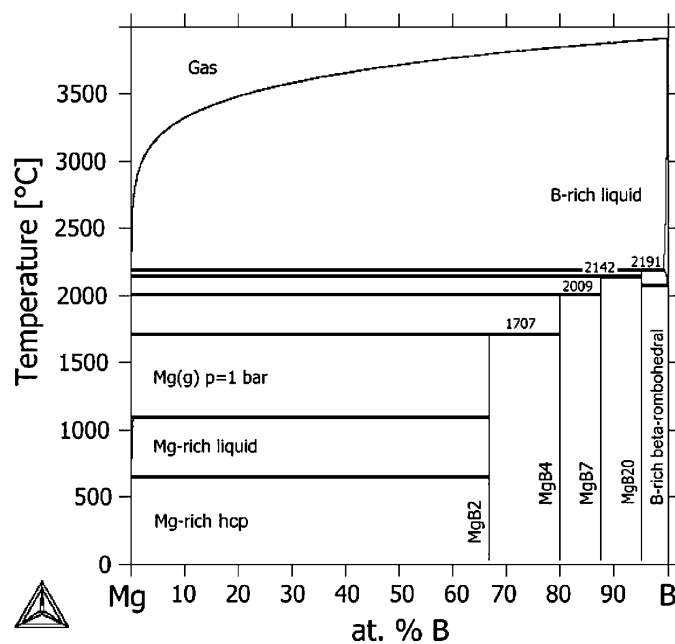


Figure 1.3. Mg - B thermodynamic phase diagram from Balducci et al [45].

was maintained at 1200 °C and the B at 600 °C [46]. This provided a high flux of Mg vapor while reacting the B at low temperature. The composite was shown to be 75% MgB₂ and 25% Mg with a critical current density of $10^6 A/cm^2$ at 10 K under self-field. In situ MgB₂/Mg composites were also created by liquid infiltration of boron powder both under Mg vapor pressure [47] and high pressure Ar gas [48]. A slight excess in Mg greatly improved mechanical strength and superconducting properties by increasing grain connectivity [49].

1.5. MgB₂ wires from boron fibers

Commercial B fiber is produced continuously through chemical vapor deposition (CVD) of B onto a W wire at 1100-1300 °C by passing the wire through a chamber of BCl₃ and H₂ gasses. The B fibers are strong (3-4 GPa tensile strength [50]), which is good for handling and winding and as with other forms of boron, MgB₂ wires can be created by reacting the boron fiber with magnesium at high temperature. By exposing 100 μm diameter boron filaments to magnesium vapor at 950 °C for 2 h in a sealed tantalum tube, MgB₂ wires were produced [7] (Figure 1.4). Their diameter swelled to 160 μm and the normally straight and flexible boron filaments became deformed and brittle MgB₂ wires. The superconducting transition temperature of the wires was 39.4 K with a critical current density of $4 \cdot 10^5 A/cm^2$ at 4.2 K under zero-field with upper critical field of 16 T. This process was also applied to boron nanowires, hundreds of μm long and 50 to 100 nm in diameter, to create 50 to 400 nm diameter MgB₂ wires with a superconducting transition at 33 K [51].

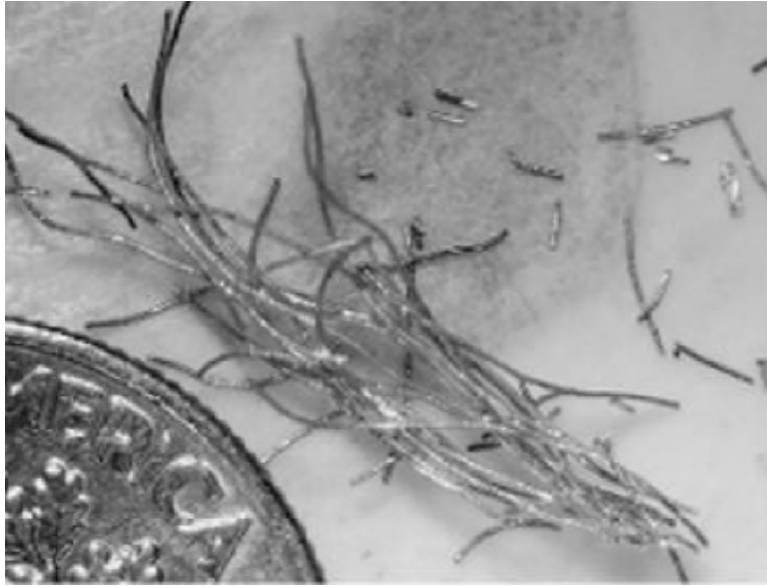


Figure 1.4. Image showing deformed MgB_2 fibers produced from reacting straight B fibers with Mg vapor at $950\text{ }^\circ\text{C}$ taken from Canfield et al [7].

Critical current density of MgB_2 wires synthesized from boron fibers was improved through additions of titanium into the boron synthesis process [52, 53]. With 5% Ti codeposited with B through adding TiCl_4 gas during the CVD boron filament creation process, a fine dispersion of TiB and TiB_2 formed within the B fiber. After subsequent reaction with Mg vapor the critical current density was measured to be $5 \cdot 10^6 \text{ A/cm}^2$ [53], an order of magnitude increase from using pure B fibers as starting material. Increased critical current densities were also maintained at higher fields further indicating an increase in flux pinning.

Upper critical field performance was increased by doping B fibers with carbon through additions of methane gas to the reaction chamber. Systematic study of carbon doping after conversion of fibers to MgB_2 showed that carbon substitutes on the B lattice and caused T_c suppression of $1 \text{ K/at}\% \text{C}$ but upper critical field performance was enhanced

by 5 $T/at\%C$ [54]. A 5.2at% C doped MgB₂ fiber had T_c of 35 K and $H_{c2}(T=0)$ of 36 T which was more than double that of pure MgB₂ [55].

Codeposition of Ti and C found that both dopants work independently with a 2.1% C, 0.5% Ti sample having the upper critical field of a carbon doped sample with an enhanced critical current density [56]. Critical current density was less than without C doping but was maintained in higher applied magnetic fields. While properties of doped B fibers are excellent, they come at the cost of reaction time. Reactions in Mg vapor at 950 °C for 4 h resulted in only 1 μm of MgB₂ on the surface of a 80 μm 0.4at% C doped fiber which increased to 10 μm of MgB₂ after 48 h [55]. Full conversion of fibers to MgB₂ was achieved by reacting at 1100 °C for 72 h [56], 1200 °C for 48 h [55, 56] or by ramping from 650 to 1200 °C over 96 h [55].

1.6. Doping of PIT MgB₂

Like the processing of B fibers into MgB₂, PIT MgB₂ technology also incorporates additional compounds to serve as dopants in MgB₂. Although only three dopants have proved to substitute on the MgB₂ lattice (Mn, Al, C) [57] many studies add elements or compounds such as Ti, Zr, Y₂O₃, or SiC that improved critical current density by segregating at grain boundaries [58–60]. Critical current densities have reached the mid- $10^6 A/cm^2$ level with these improvements. Although these are great improvements from the value of $0.85 \cdot 10^5 A/cm^2$ reported in early studies [61], the pair breaking critical current density of MgB₂ is believed to be near $2 \cdot 10^7 A/cm^2$ [62]. Only epitaxially grown thin films processed under very clean conditions and producing 100 nm size grains have approached

this level [63]. For comparison, critical current densities of Nb_3Sn are 10^6 A/cm^2 with YBCO superconductors 10^7 A/cm^2 [11].

Carbon is also used to increase upper critical field capability of PIT MgB_2 and is introduced into MgB_2 through the use of SiC particles [36, 58, 64, 65], carbon nanotubes (CNT) [64, 66–68], nano carbon particles [69], B_4C particles [70, 71], and carbon doped plasma synthesized boron powder [72]. The most widely studied addition is SiC where improvements in upper critical field capability come with improvements to critical current density due to the Mg reaction with Si to form Mg_2Si precipitates that enhance pinning [58]. The C substitutes for B on the lattice and serves as a point defect that pushes the upper field over 33 T [65]. Carbon nanotubes align due to drawing of PIT MgB_2 and provide enhanced thermal and electrical conductivity in addition to improved superconducting properties [68]. Carbon doped plasma synthesized powders were created by plasma decomposition of BCl_3 and CH_4 gases similar to the production of doped fibers. Plasma powders reacted to MgB_2 incorporated 7.4at% C and have $H_{c2}(T=0)$ of 37 T with J_c over 10^5 A/cm^2 out to beyond an applied field of 5 T [72].

1.7. Reaction Kinetics

Few systematic processing and kinetics studies have been carried out into the formation of MgB_2 . These studies did not record the degree of reaction as a function of time, so that kinetic parameters, such as reaction rate constants and activation energy, remain mostly unknown. One study examined the reaction between magnesium vapor and boron powder using magnesium lumps and crystalline ^{11}B powder [73]. This mixture was sealed in a tantalum tube under a partial pressure of argon. The sealed tube was then enclosed in a

quartz tube under argon and heated in a box furnace to 950 °C. Using conventional x-ray diffraction at room temperature on samples heat treated for specific times, it was shown that the reaction proceeds rapidly between 30 and 60 min and after 60 min there is little change to the MgB_2 peak, suggesting that the reaction was complete after 60 min. The same authors studied the synthesis of MgB_2 wires from Mg vapor and boron filaments using 100 and 140 μm diameter fibers [73]. These fibers were placed in a tantalum tube with excess magnesium and sealed under a partial pressure of argon gas. The tantalum package was then sealed in a quartz tube under argon and reacted at 950 °C in a box furnace. The 100 μm fiber was about 50% reacted after 60 min and fully reacted after 120 min. The larger fibers were reacted for 36 h and had similar results. Magnesium was believed to diffuse along the tungsten-boride core of the boron filaments and also through cracks and then react to form MgB_2 . This observation was made from micrographs of partially reacted fibers where MgB_2 was visible near the center of the fiber and also in isolated areas away from the surface as shown in Figure 1.5. During the reaction, it was believed that first a front of MgB_7 forms followed by a front of MgB_4 and then finally MgB_2 results [53]. This speculation was made based upon spot EDX measurements but data was not shown.

Only one study has investigated growth of MgB_2 and also measured kinetic parameters such as the diffusion coefficient. A 300 nm amorphous B thin film was reacted with Mg vapor at 800 °C and the thickness growth modeled with time [74]. The effective diffusion coefficient was determined to be $10^{-16}\text{m}^2/\text{s}$.

Synchrotron x-ray diffraction has been used to study chemical synthesis, phase transitions, and reaction kinetics of a wide range of alloys, ceramics and compounds (e.g.,

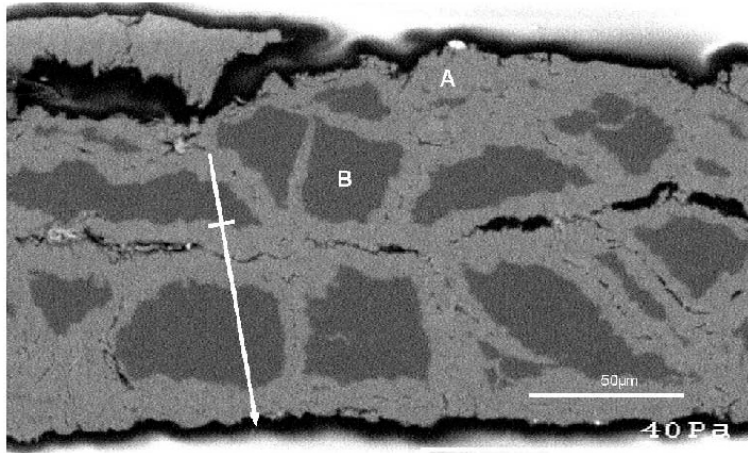


Figure 1.5. Scanning electron micrograph showing a non-uniform front of MgB_2 formation in a B fiber from reaction with Mg vapor at $950\text{ }^\circ\text{C}$. The lighter area labeled A is MgB_2 and is located near the center as well as the edge of the fiber with isolated Mg deficient borides labeled B also shown [73].

Ti-6Al-4V [75], steel [76], ZrO_2 [77], SnO [78], NiWO_4 [79], Na_2PdC_2 [80], silicate [81], and BiSCCO superconductor [82]). With this technique, the degree of reaction can be measured as a function of time in a single in-situ experiment. Two in-situ synchrotron studies of the reaction of MgB_2 from powders have measured degree of reaction vs time.

Baranov et al. [83] used a constant rate of $0.3\text{ }^\circ\text{C/s}$ throughout their experiments which were performed under very high hydrostatic pressures (2.8 GPa and 5.5 GPa). High pressures affect phase stability - in particular the melting point of Mg is increased by 50 K/GPa - making these reactions much different than reaction at ambient pressures commonly used for PIT synthesis of MgB_2 . Reaction curves were S-shaped as shown in Figure 1.6 and started at 587 and $887\text{ }^\circ\text{C}$ (with solid Mg) and finished at 927 and $1127\text{ }^\circ\text{C}$ (with liquid Mg) for pressures of 2.8 and 5.5 GPa, respectively. For these heating rates, reaction times were then 1100 s and 800 s.

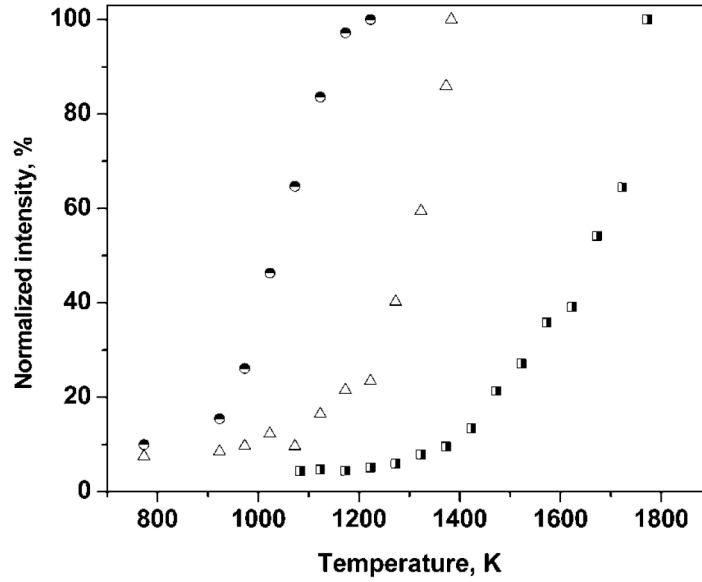


Figure 1.6. Normalized synchrotron diffraction intensity vs temperature plot from Baranov et al [83] showing S-shaped reaction curves for the formation of MgB_2 under a heating rate of $0.3 \text{ }^\circ\text{C/s}$.

Grivel et al. [84] reacted Mg and B powders in a Fe sheath at final temperatures of 780 and 650 $^\circ\text{C}$ which were reached at a slow rate of $0.06 \text{ }^\circ\text{C/s}$, with substantial formation of MgB_2 before the experiment became isothermal as shown in Figure 1.7. The latter reaction temperature corresponds exactly to the melting point of Mg, so it is unclear to what extent the metal was liquid during reaction. These experiments were also complicated by the formation of MgO , due to presence of oxygen in the system, and Fe_2B , through reaction with the sheath material, which may have depleted Mg and/or B and thus affected MgB_2 synthesis; however, these authors did not report the presence of MgB_4 .

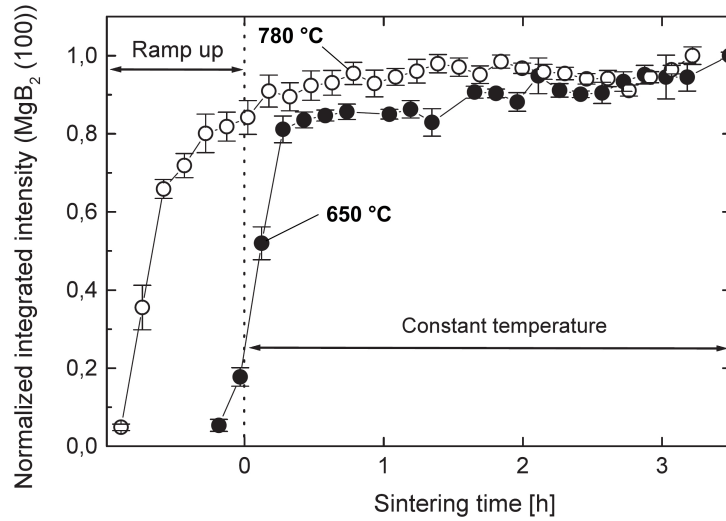


Figure 1.7. Normalized integrated intensity vs time plot from Grivel et al [84] showing MgB_2 formation before isothermal conditions were reached due to a slow heating rate of $0.06 \text{ }^\circ\text{C/s}$.

1.8. Advancement of Scientific and Technological Research

Considering the research outlined above, there is considerable room for advancement in both scientific and technological MgB_2 research. Scientifically, there has been no systematic study of bulk MgB_2 synthesis, whether from powders or fibers, to determine diffusion coefficients and activation energies. Kinetic parameters will provide predictive power to determine the reaction temperature and time required to synthesize MgB_2 given powder shape and size. Technologically, PIT wires have dominated the processing research, although new fabrication techniques such as high temperature deformation may show improved properties and easier, cheaper synthesis. Cores of most PIT wires are heavily porous and densification as shown by hot isostatic pressing (HIP) significantly enhances superconducting properties but HIP is an expensive batch process. The mechanical properties of MgB_2 at high temperature have not been studied and mechanical deformation

rather than HIP may be applicable to continuous densification of PIT cores. Additionally, synthesizing MgB_2 fibers from continuous commercial B fibers shows promising results in both doped and undoped cases, however, the MgB_2 is very thin and brittle. Reacting these fibers within Mg liquid forming an MgB_2 composite after solidification is a more technologically viable application of this style of MgB_2 processing with further development of the technology available in continuous fiber infiltration techniques [85]. The following chapters address these fundamental processing science and engineering research areas through developing new MgB_2 processing techniques and systematically studying the synthesis and properties of these new, as well as established, methods.

CHAPTER 2

MgB₂ Reaction Kinetics from Elemental Powders

As discussed in Chapter 1, the bulk of the research effort into creating MgB₂ composite wires has concentrated on the powder-in-tube (PIT) approach, where a metallic tube filled with Mg and B powders is drawn into a wire and subsequently heated to convert the powders into MgB₂ according to Equation (1.1) [31, 86–89]. Reported times for reaction completion vary from a few minutes at 840 °C [25] to 48 hours at 620 °C [86], but these studies did not record the degree of reaction as a function of time, so that kinetic parameters, such as reaction rate constants and activation energy, remain mostly unknown. Carbon-doping has emerged as an effective means for increasing the upper critical field capability of MgB₂ [54–56, 72, 90]. The reaction kinetics for full conversion of C-doped boron to MgB₂ have not been studied systematically either, with times to achieve full reaction varying widely among authors, e.g., from days at 1200 °C [55, 56] to minutes at 700–900 °C [72].

In this Chapter, the use of synchrotron x-ray diffraction to investigate, under isothermal, in-situ conditions, the effect of reaction temperature and carbon doping upon the kinetics of MgB₂ synthesis between solid B and liquid Mg (Equation (1.1)) is discussed, and results are modeled based on diffusion theory.

2.1. Experimental Procedures

Three types of high-purity B powders were studied: (i) amorphous, 99.99%-pure powders (commercially available from Sigma Aldrich, St. Louis, MO) with 400 nm average particle size, as determined by the manufacturer by the Fisher method, (ii) plasma-synthesized, amorphous powders with 99.999% purity and 400 nm average particle size (from Specialty Materials, Inc., Lowell, MA) and (iii), the same type of powders but additionally doped with 7.4at% carbon during plasma synthesis [72]. All B powders were imaged using an environmental scanning electron microscope (FEI Quanta Schottky field emission gun SEM) after having been ultrasonically dispersed in acetone, dried on a Si wafer and sputter-coated with 6 nm of Au/Pd. Particle size was determined by taking the square root of the average particle area, determined using ImageJ software.

Each B powder type was mixed with Mg powders ($> 99\%$ pure, 177-420 μm from Fisher Scientific, Hampton, NH) at a molar ratio $\text{B/Mg} = 1.8$. This ratio was below the stoichiometric value ($\text{B/Mg} = 2$), so excess Mg could react with the air sealed in the tube and then establish an equilibrium Mg vapor pressure throughout the reaction. The powder mixtures (with a total mass of 0.2 g) were uniaxially cold-pressed to 300 MPa using a 5.5 mm diameter steel die. The resulting powder compacts, 60% dense and 10 mm in height, were placed within a 100 mm long pure titanium crucible with 8 and 9.5 mm inner and outer diameters. Titanium was selected as crucible material because it does not react with liquid or gaseous Mg vapor and has much lower x-ray absorption than other metals (Fe, Ni, Cu, Nb or Ta) used as PIT tubes. A 20 mm long section at the end of the crucible was thinned to 8.5 mm outer diameter, resulting in 0.25 mm thick walls, to reduce the absorption and scattering of X-rays by the crucible. A K-type thermocouple

was introduced in a small hole machined at the lower part of the crucible which was sealed with a carbon-steel compression fit cap and placed within a quartz tube.

Diffraction experiments were performed at the Advanced Photon Source (Argonne National Laboratory, IL) using the beamline end station 5-BM-D (DuPont-Northwestern-Dow Collaborative Access Team Synchrotron Research Center). An infrared furnace heated the crucible through the evacuated quartz tube to 500°C in 5 min, followed by a 5 minute hold. The quartz tube was then backfilled with 0.33 atm of argon, maintained constant during the experiment, and the crucible was heated in 5 min to the reaction temperature chosen in the range 670-900°C (i.e., above the 650 °C melting point of Mg), with an average heating rate of 0.6 - 1.3 °C/s. Heating was rapid enough to prevent any significant reaction to occur prior to reaching the final temperature, as ascertained by diffraction. The reaction was monitored in-situ by a 65 keV ($\lambda = 0.019$ nm) synchrotron x-ray beam with a square 1 x 1 mm cross-section, positioned perpendicularly to the crucible walls and penetrating through both quartz and titanium walls, as shown schematically in Figure 2.1. Transmitted diffraction rings were recorded, after 10 - 60 s. exposures times, on a 150 mm diameter charge-coupled device camera (Photonic Science Limited, UK) placed at about 380 mm from the sample.

The intensity of the diffraction rings was first integrated over their circumferences to create plots of intensity vs. 2Θ (where Θ is the diffraction angle), using FIT2D software [91]. The intensity of the $(10\bar{1}1)$ MgB_2 peak (after background subtraction described in Appendix A and shown in Figure 2.2 and integration over a typical 2Θ range of 4.9 - 5.2° using JADE 6.5 powder diffraction software) was determined for each diffraction pattern. This intensity, divided by the integrated intensity after full reaction, provides the degree

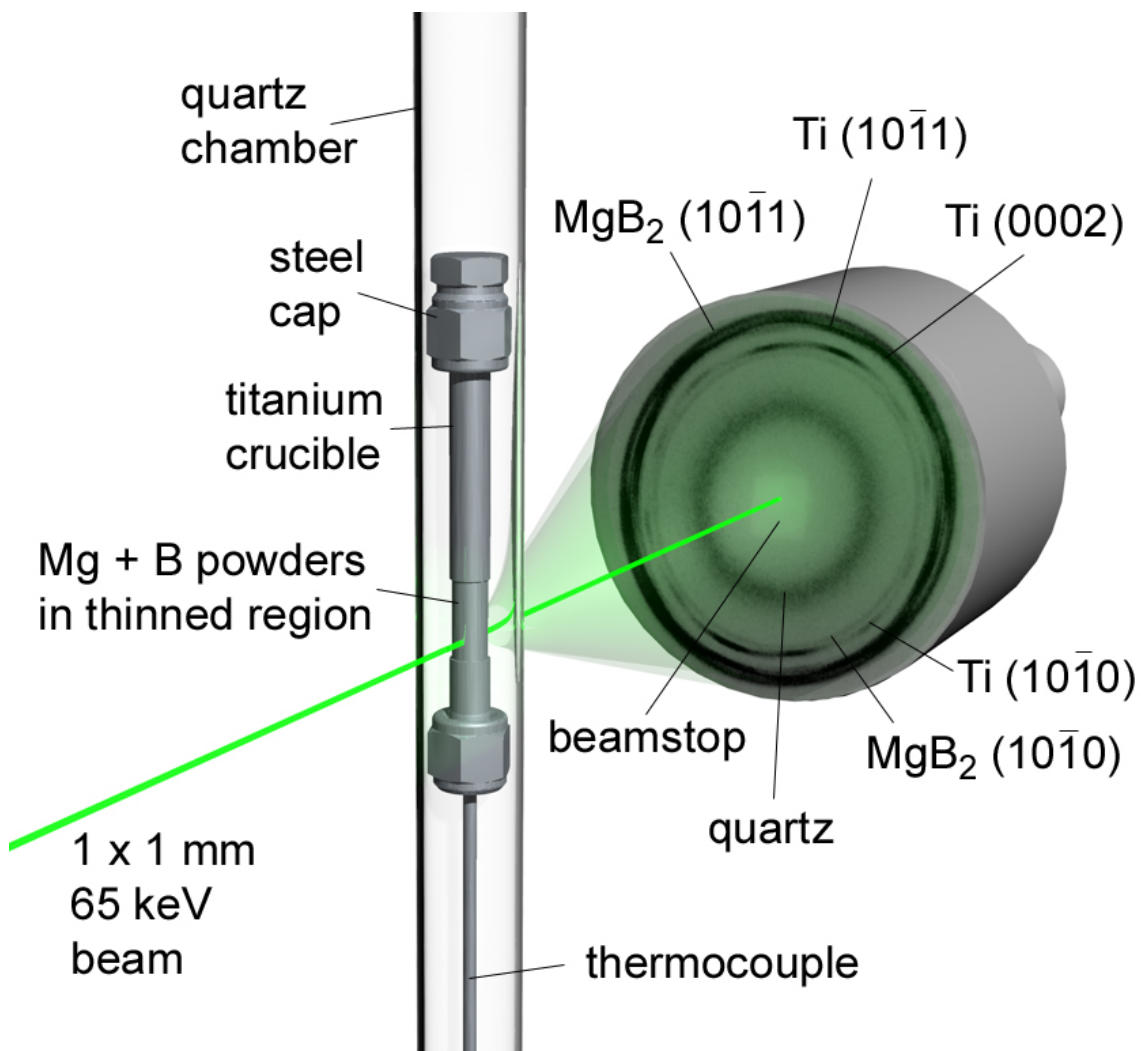


Figure 2.1. Schematic of experimental set-up for in situ synchrotron x-ray diffraction experiment. A CCD camera experimental image shows MgB₂, Ti, and quartz rings.

of reaction representing the volume fraction of reacted B. This value is different from the volume fraction of synthesized MgB₂ due to the volume change associated with B \rightarrow MgB₂ reaction.

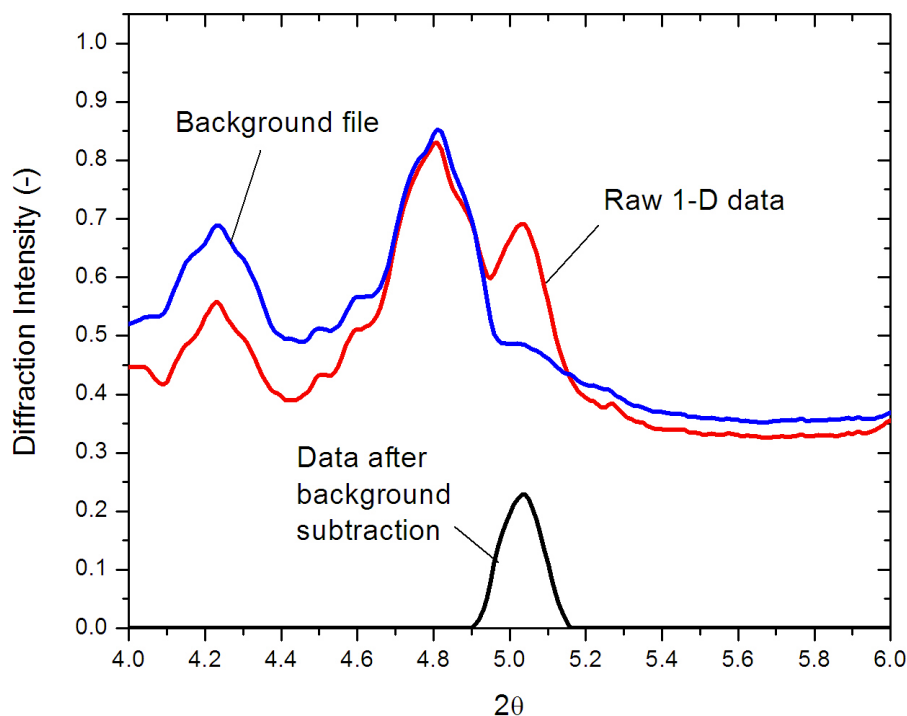


Figure 2.2. Plots of intensity vs 2θ for example experiment where a pattern collected during heat up is used as the background for future patterns.

2.2. Results

Powders for the undoped, commercial boron exhibited sizes in the 100 - 600 nm range (Figure 2.3(a)), in agreement with the 400 nm average size reported by the manufacturer. The plasma-synthesized B powders, with and without carbon-doping, were of similar size and morphology (Figures 2.3(b-c)). In all three cases, these 400 nm powders consist of agglomerates or irregularly-shaped chains of 10 - 50 nm spheroid particles (Figures 2.3(a-c)). The plasma-synthesized powders were previously reported to be agglomerates 1 - 50

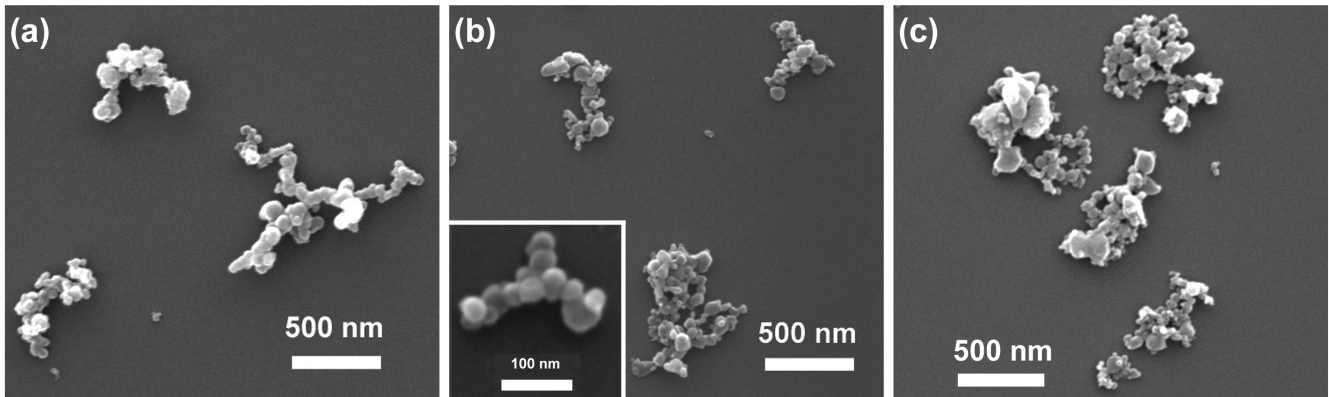


Figure 2.3. Scanning Electron Microscope images of (a) undoped commercial B powder with average particle size of 400 nm. Particle size analysis of SEM images show sizes range from 100 to 500 nm. (b) undoped plasma-synthesized B powder. Particle size analysis of SEM images show sizes range from 100 to 500 nm as found with the commercial powder. Inset shows particles are agglomerates of 10 to 50 nm spheres. (c) C-doped plasma-synthesized B powder. Particle size analysis of SEM images show sizes range from 100 to 500 nm as found with the commercial powder

μm in size [72], but such agglomerates were not found, possibly because acetone was used to disperse the powders onto single crystal Si wafers for SEM analysis.

Figure 2.1 shows a typical diffraction pattern for the undoped plasma-synthesized B powders reacted at 750 °C for 5000 s (beyond full reaction completion at 3500 s), showing a intense, smooth ring for the $(10\bar{1}1)$ MgB_2 reflection as well as rings for $(10\bar{1}1)$, (0002) , $(10\bar{1}0)$ Ti from the crucible, a weaker, smooth $(10\bar{1}0)$ MgB_2 ring, a very broad ring from the quartz tube and the square beam-stop in the center.

Plots of degree of reaction vs. time are shown in Figure 2.4(a-c) for the three types of B powders reacted isothermally between 670 and 900 °C. Curves are parabolic in shape, indicative of a diffusion limited reaction [92]. Figure 2.4(a) shows that, for the undoped commercial B powders, the time for full reaction drops from 3500 to 120 s as

the temperature increases from 700 to 900 °C. A short incubation time of 100 s is visible for the reaction at 750 °C, while the experiment performed at 700 °C seems to exhibit a much longer incubation time. However, the MgB₂ diffraction peak was weak in this particular experiment, probably because the beam did not sample a large enough volume, so degree of reaction could not be ascertained reliably below a value of 0.19 preventing a precise determination of the incubation time.

Figure 2.4(b) shows that a similar strong temperature dependence exists for the reaction of the undoped, plasma-synthesized B powders. Times to complete the reaction are similar to the undoped, commercial B powders (Figure 2.4(a)), e.g., 900 s. (as compared to 300 s.) at 800°C, and 3500 s. (vs. 3500 s.) at 700°C. Figure 2.4(c) for the C-doped plasma-synthesized powder shows curves with the same parabolic shape, but with a somewhat inconsistent temperature response, i.e., faster reaction at 670 than 700°C, and faster reaction at 750 than 800°C. No incubation times were found for either type of plasma-synthesized B powder.

2.3. Discussion

In the two existing in-situ synchrotron x-ray studies of MgB₂ synthesis (refs), slow heating rates were used, resulting in non-isothermal reaction occurring with solid Mg and, later in the experiment, with liquid Mg. Neither study attempted to model the reaction and determine kinetic parameters such as reaction rate constants or activation energies.

Because the present experiments used a relatively rapid heating rate (1 °C/s), no MgB₂ was observed in diffraction patterns before the isothermal temperature was achieved.

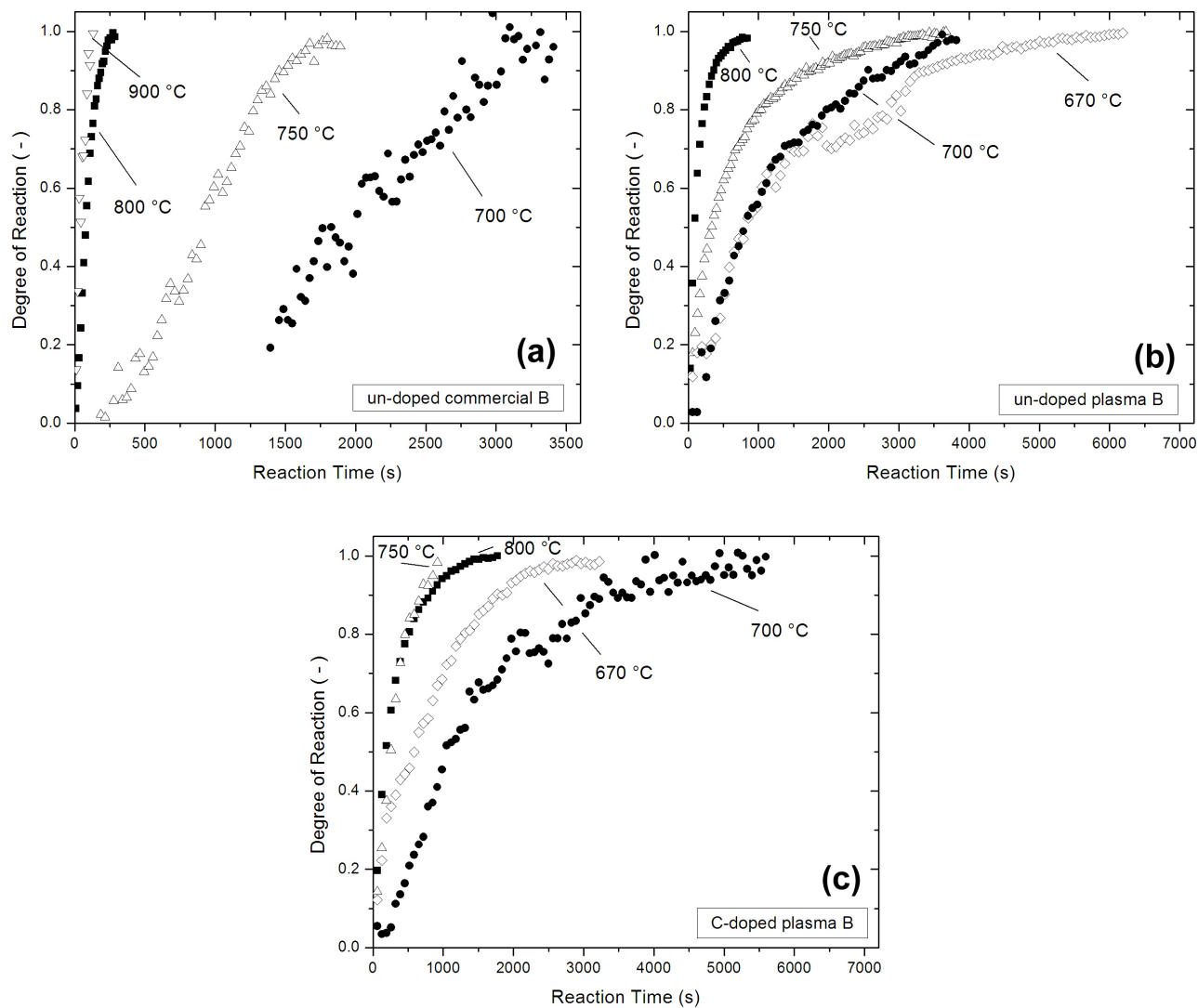


Figure 2.4. Degree of reaction vs. time plots generated using synchrotron x-ray diffraction technique for powder compacts of Mg powder and (a) 400 nm amorphous boron powder reacted between 700 and 900 °C showing completed reaction between 10 min and 2 hours, (b) undoped plasma-synthesized powders reacted between 670 °C and 800 °C, and (c) C-doped plasma-synthesized powders reacted between 670 °C and 800 °C

They thus can be considered to be isothermal, allowing the use of isothermal reaction models from which reaction constants and activation energies can be calculated. The experimental data (Figure 2.4(a-c)) were fitted to a model for the diffusion-limited reaction of spheres in a gas or liquid [92], which relates the degree of reaction x with the reaction time t as:

$$(2.1) \quad [1 + (z - 1)x]^{\frac{2}{3}} + (z - 1)(1 - x)^{\frac{2}{3}} = z + 2(1 - z)r_0^{-2}kt$$

where z is the volume expansion for the reaction given by Equation (1.1) ($z = 1.90$ [5] for Eq. (2.1)), r_0 is the powder radius ($r_0 = 200$ nm, as discussed below) and k is the reaction rate constant. Eq. (1.1) takes explicitly into account that the reaction occurs at a spherical interface with a volume change given by the parameter z , and is valid until completion ($x = 1$).

It is assumed here that liquid Mg fills the space between the 400 nm B powders, and that each powder reacts as a single sphere surrounded by liquid Mg, thus forming a surface MgB₂ layer growing by diffusion of Mg and/or B. We do not consider the reaction of individual 10 - 50 nm spheroid particles, because it is very unlikely that Mg wetted the powders allowing a direct contact between the melt and the individual spheroid particles. The lack of wetting was verified in ex situ experiments where liquid Mg was placed on top of compacted B powders; macroscopic infiltration was observed only at temperatures in excess of 1000 °C, well above the highest temperature of 900°C used here.

Plotting the left-hand side of Equation (2.1) against time provides near linear curves, as shown in Figures 2.5(a-c), except for the early parts of the experiments at 700 and 750 °C with undoped commercial B powders which exhibited incubation times. The

good fit over the whole time range of the other ten experiments without incubation time demonstrates that the model can be applied to the present data, despite the fact that the particles are far from spherical. The slope of a best-fit line then provides the rate constant k . At 800 °C, these constants are $k = 3.1 \cdot 10^{-17} m^2/s$ for the commercial undoped powders (ignoring the early data for the experiments at 700 and 750 °C), and $k = 8.1 \cdot 10^{-18} m^2/s$ for the undoped plasma powders. These values are in reasonable agreement with a value of $k = 4.8 \cdot 10^{-17} m^2/s$ for an amorphous boron thin film deposited by electron beam evaporation and exposed to Mg vapor pressure at 800 °C (20 Torr [93]) by Kim et al. [74]. The latter value was calculated, as shown in Figure 2.6 by plotting as a function of time the thickness data of the thin film reaction [74] fitted to $y = \sqrt{2zkt}$ which is valid for a planar interface as derived in Appendix B.1.

The linearity of the fits shown in Figure 2.5(a-c) for all temperatures, and good fit with the rate constant calculated from the thin film diffusion experiment are strong evidence that the MgB₂ synthesis reaction (Equation (1.1)) is diffusion-limited. In the case of the undoped commercial powders at 750 °C (Figure 2.5(a)) there is some nonlinearity at the beginning of the reaction where the reaction is proceeding much slower than the model would predict. This is possibly due to presence of oxide on the surface of the powders which must first react with Mg before the reaction to MgB₂ can proceed, thus slowing the onset of the faster bulk reaction to MgB₂. This also appears to be the case with the undoped commercial powders reacted at 700 °C (Figure 2.5(a)) although due to an overall low diffraction intensity during the experiment, a measurable peak did not appear until the reaction was nearly 20% complete. In both cases, k was determined from the linear

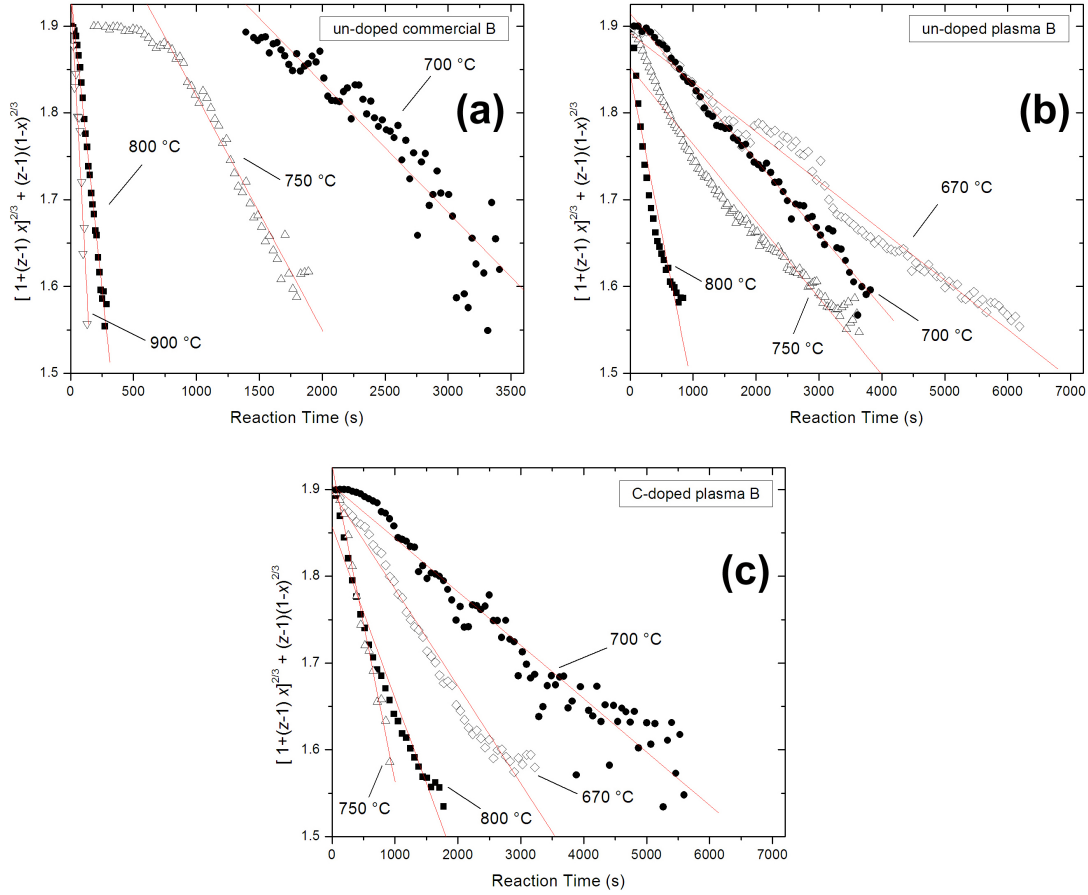


Figure 2.5. Degree of reaction vs. time plots showing a linear relation to reaction time using the Carter diffusion limited reaction of spheres model [92] for (a) un-doped commercial B powder, (b) un-doped plasma synthesized B powder, and (c) C-doped plasma synthesized B powder. Best fit lines were used to determine reaction rate constant k .

portion of the data. An Arrhenius plot of the rate constants (Figure 2.7) provides activation energies of 108 and 146 kJ/mol for the undoped plasma and commercial powders, respectively.

Additionally, the degree of reaction vs time data was converted to reaction layer thickness vs time and fitted with a model developed by Entchev et al [94] for the reaction

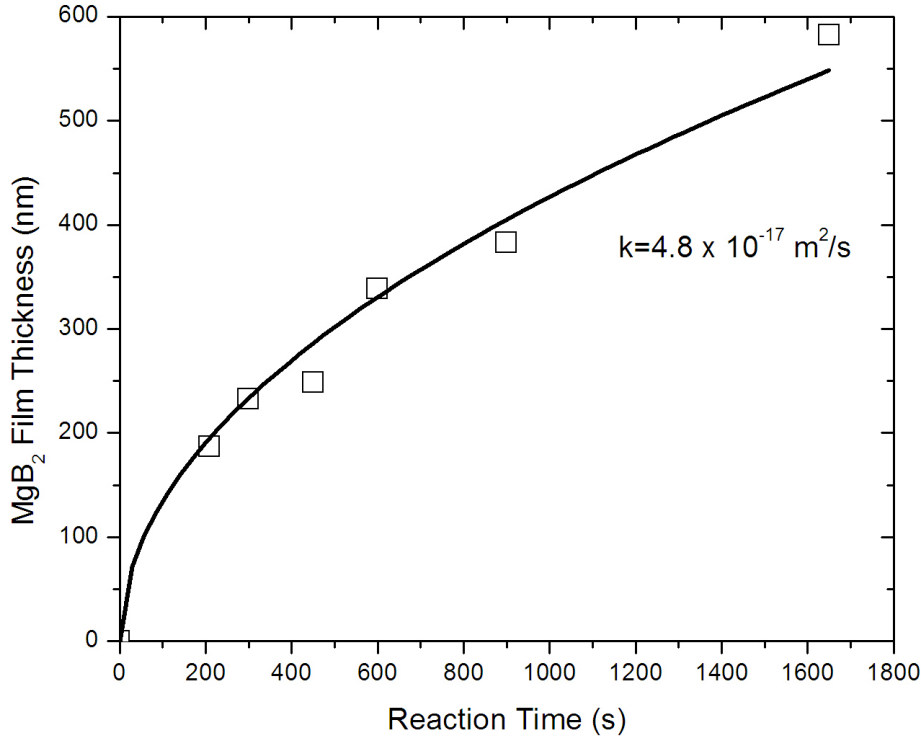


Figure 2.6. MgB₂ thickness data vs time at 800 °C from Kim et al [74] fitted with planar reaction equation to determine the reaction rate constant k . The rate constant was $4.8 \cdot 10^{-17} m^2/s$ which compared well with powder reactions at 800 °C.

of a sphere. The model was designed with volume expansion coefficients $z = 1$ and 1.766 for the growth of TiO₂ on Ti. These volume expansion coefficients were not a match for the growth of MgB₂ ($z = 1.90$) so experimental data was scaled by $\sqrt[3]{z}$ to convert the three-dimensional sphere growth to a one-dimensional thickness measurement and fitted with a 5th degree polynomial representing the $z = 1$ model. The fitting parameter was the diffusion coefficient D . Fits to scaled diffusion thickness vs time plots for the reaction of the three B powders are shown in Figures 2.8(a-c). Scaled diffusion thickness should

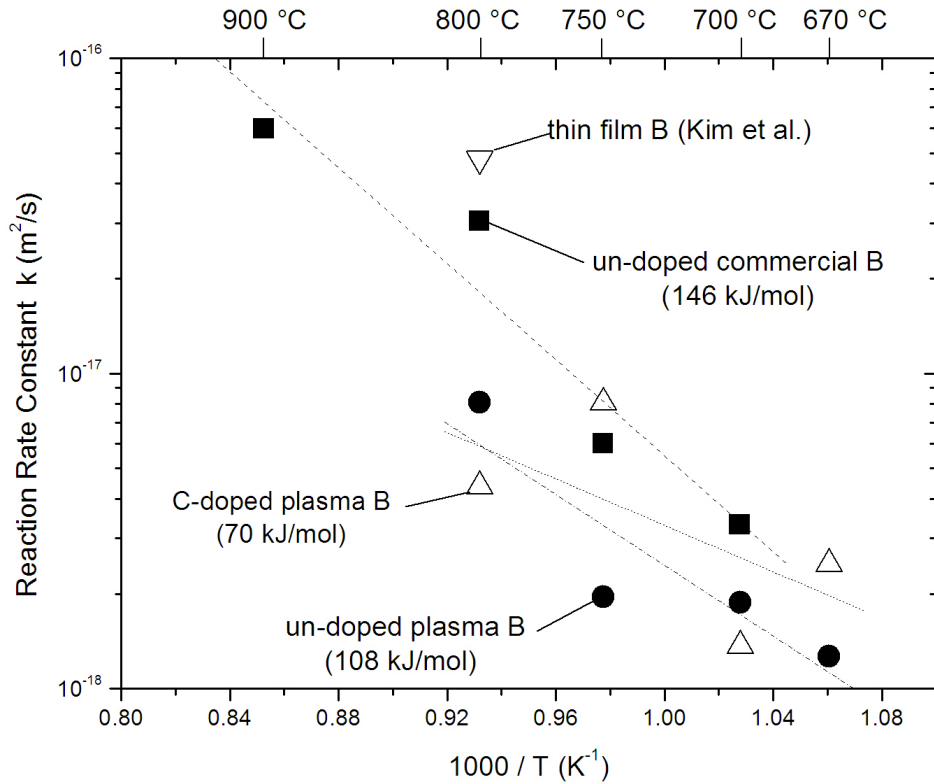


Figure 2.7. Arrhenius plot of reaction rate constants k vs. inverse temperature showing activation energy for un-doped commercial, un-doped plasma-synthesized, and C-doped plasma-synthesized B powders. A data point from a thin film experiment [74] (Figure 2.6) is shown for comparison.

end at a value of 1 but there was little data in this range considering a degree of reaction of 0.99 corresponded to a scaled diffusion thickness of only 0.8 where a degree of reaction of 1 corresponded to a thickness of 1.

Diffusion coefficients ranged from $8 \cdot 10^{-18}$ to $5 \cdot 10^{-16} \text{m}^2/\text{s}$. These values were about an order of magnitude different from the rate constants determined by the Carter model [92]. The activation energies calculated from an Arrhenius (Figure 2.9) plot of the diffusion coefficients vs temperature were similar (73 - 149 kJ/mol) to those determined from

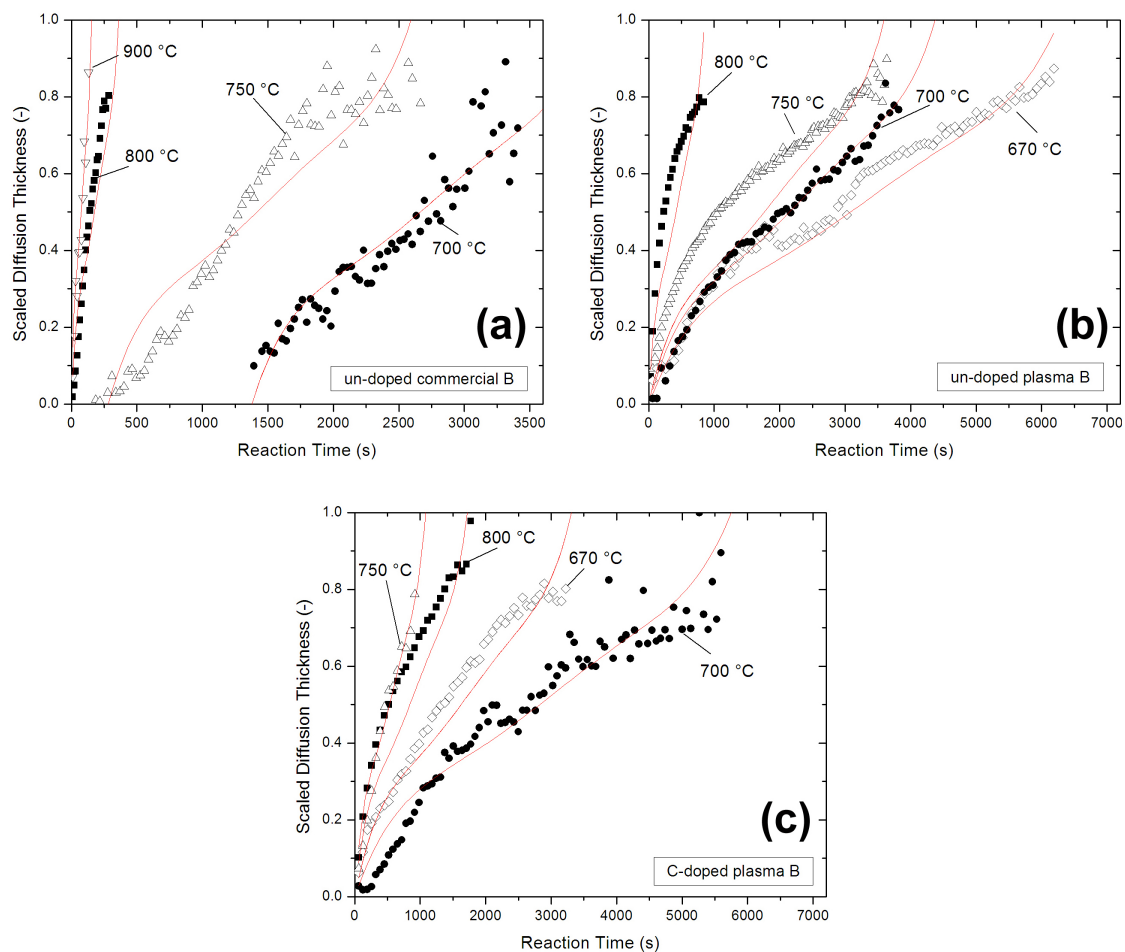


Figure 2.8. Scaled diffusion thickness vs. time plots with fits of the Entchev sphere reaction model [94] with $z = 1$ and diffusion coefficient D as the fitting parameter for (a) un-doped commercial B powder, (b) un-doped plasma synthesized B powder, and (c) C-doped plasma synthesized B powder.

rate constants using the Carter model (70 - 146 kJ/mol) showing the Entchev sphere model diffusion coefficients were scaled with respect to the reaction rate constants but dependence on temperature was the same.

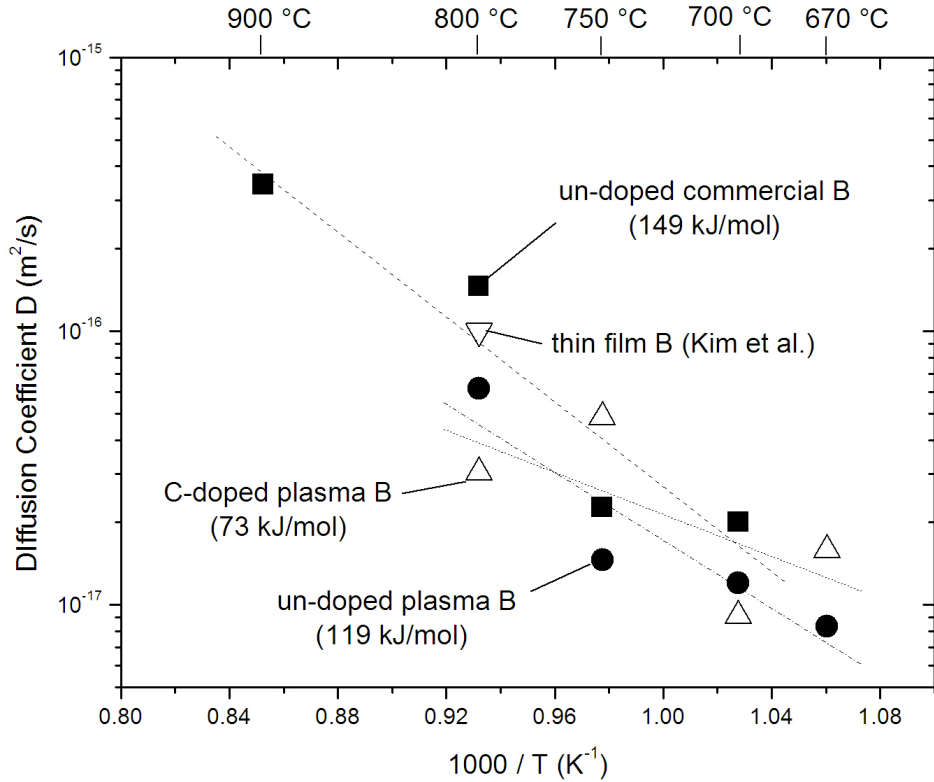


Figure 2.9. Arrhenius plot of diffusion coefficients D vs. inverse temperature showing activation energy for un-doped commercial, un-doped plasma-synthesized, and C-doped plasma-synthesized B powders. A data point from a thin film experiment [74] is shown for comparison.

The reaction times measured here for the C-doped powders (1000 - 5500 s for 670 - 800 $^{\circ}\text{C}$, Fig. 3(c)) are consistent with observations reported for similar C-doped plasma-synthesized powders [72]: in that study, reaction times of 1800 s. at 700 $^{\circ}\text{C}$ and 800 $^{\circ}\text{C}$ were speculated to have incomplete reaction with MgB_4 regions observed by energy dispersive spectroscopy (EDS). The likelihood of MgB_4 was confirmed by both samples having higher than expected superconducting T_c measurements due to some dopant remaining in the MgB_4 regions rather than the MgB_2 where it will suppress T_c [54]. Powders reacted

for 1800 s at 900 °C showed a T_c consistent with a completed reaction to C-doped MgB_2 . When plotted according to Equation (2.1), the kinetic data (Figure 2.4(c)) for the C-doped powders provide good linear fits (Figure 2.5(c)). The activation energy determined from a best-fit of the rate constants determined from these fits is however anomalously low, $Q = 70$ kJ/mol, because of the inconsistent temperature response evident in Figure 2.4(c) (i.e., more rapid kinetics at 670 than 700°C, and at 750 than 800 °C). However, when plotted in Figure 2.7, it is apparent that there is no significant difference in rate constants between the doped and undoped plasma-synthesized powders, within the large experimental error, if the value of k at 750°C is removed for the C-doped powders. Given the low levels of doping and the assumption of volume diffusion for the controlling mechanism, this result is not unexpected. The high temperature variability found for the C-doped powders remains unexplained, but may be due to variation in dopant content between batches.

2.4. Conclusions

The kinetics of the synthesis reaction of MgB_2 from elemental powders, relevant to the powder-in-tube process, were measured in situ using synchrotron x-ray diffraction at various temperatures. Reaction times for powder compacts of Mg and 400 nm amorphous B powders or plasma-synthesized B powders, both doped and undoped with carbon, ranged from 2 to 120 min at temperatures between 670 and 900 °C. Undoped B reactions were fit with two diffusion-limited models with activation energies between 108 and 146 kJ/mol. Carbon-doped B powders had similar rate constant as the undoped powders, indicating that the volume diffusion reaction mechanism is not affected by doping.

CHAPTER 3

Compressive Ductility at High Temperature

Most ceramics can be densified from powders under near-hydrostatic conditions at elevated temperature by a combination of surface and volume diffusion, and microplasticity. As expected, MgB_2 powders can be densified by hot isostatic pressing (HIP) at 950 - 1000 °C with pressure of 100-200 MPa for 3-4 h [20, 22, 41], uniaxial die hot pressing at 700 °C and 640 MPa for 10 - 90 min [14], die upsetting at 800-900 °C with strain rate of 10^{-3}s^{-1} resulting in a max stress of 450 MPa [15], and under 3 - 3.5 GPa stress in a cubic anvil press at 800-1000 °C [21, 24]. However, macroplasticity leading to high uniaxial strains is much more difficult to attain because fracture (which is inhibited under hydrostatic conditions) often occurs before the activation of the deformation mechanism operating at high temperature (dislocation climb or grain-boundary sliding). Most ceramics show some compressive ductility (1 – 10%) at elevated temperature ($T/T_m > 0.7$), but very few exhibit large-scale ductility ($> 50\%$) typical of metals.

The accepted definition of superplasticity is tensile elongation in excess of 100% [95]. Superplasticity exists at high temperatures ($T/T_m > 0.75$) in many metals and a few ceramics (YTZP (800% [95]), Al_2O_3 (65% [95]), hydroxyapatite (150% [95]), Si_3N_4 (230% [95]), and SiC (140% [96]) where microstructures are engineered to possess very fine grain structure ($< 1 \mu\text{m}$) or a high temperature liquid phase at grain boundaries. Large compressive strains (although not necessarily superplastic) are observed in similarly engineered materials such as Al_2O_3 [97], Si_3N_4 [98], and SiC [99].

Since the discovery of superconductivity in MgB_2 [1] and its lack of weak link behavior at grain boundaries [9], wires of MgB_2 have been fabricated by powder-in-tube (PIT) technology through both in situ and ex situ routes as discussed thoroughly in Chapter 1. In both processing techniques, the resulting superconducting core of the PIT wire is porous. In situ processing typically combines Mg and B powders within a metal tube, deforms the tube into a wire and reacts the powders to form MgB_2 . Even if full density was achieved during the deformation due to some ductility of Mg, the MgB_2 occupies only 76% of the volume of the original Mg and B powders [12] due to the differences between the molar volumes of the reactants and product. Ex situ PIT similarly deforms pre-reacted MgB_2 powders into a wire while contained in a metal sheath where MgB_2 is hard and brittle and the powders merely crush but do not deform plastically into full density. The use of HIP has improved the connectivity of MgB_2 grains and increased density in bulk samples [22, 23, 100] as well as PIT MgB_2 [20, 41, 101, 102], however it is an expensive batch process not applicable for continuous wire production. Superconducting properties of PIT MgB_2 wires have improved dramatically through chemical modifications [36, 65, 68, 72] but the cores of PIT MgB_2 wires continue to operate at 40 – 60% density [58, 71]. While the J_c of MgB_2 may extend to 10^6 A/cm^2 , the J_e of the wire (current over the entire wire cross section, including metallic sheath) is greatly reduced due to the porosity and the flux pinning reduced at higher fields because of the lack of grain connectivity [27, 103, 104].

Many other borides have the AlB_2 type structure of MgB_2 , with ZrB_2 and TiB_2 of the most scientific and engineering interest due to their high hardness and melting points. Melting points of AlB_2 type borides from [105] are shown in Figure 3.1 showing a linear relation to Gibbs free energy of formation. The melting point of MgB_2 is not known

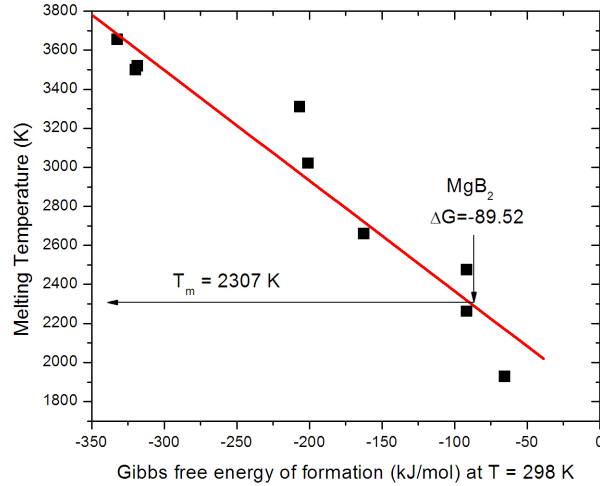


Figure 3.1. Plot of melting temperature vs Gibbs free energy of formation for AlB_2 type borides showing linear relationship used to estimate an MgB_2 melting temperature of 2307 K.

since it is listed to decompose at 900 °C and does decompose to MgB_4 and MgB_7 in vacuum [106,107]. Based on the linear relation, the MgB_2 melting point is estimated to be 2307 K. AlB_2 type borides are typically difficult to sinter and deform due to their strong covalent bonding and high Peierls stress [108], however, some compressive plasticity is observed at high temperatures. TiB_2 with 2 - 20 μm grain size exhibited compressive plastic yielding due to dislocation glide at 1700 - 2000 °C ($T/T_m = 56 - 65\%$) [109] with single crystal ZrB_2 showing 4.5% compressive plastic deformation at 2125 °C ($0.68 T_m$) with compressive yielding at 110 MPa [110], and 8.5% compressive creep strain in a 87% dense polycrystalline sample at 1600 °C ($0.53 T_m$), 220 MPa and a strain rate of $2 \cdot 10^{-7} s^{-1}$ [111]. The high temperature mechanical properties of MgB_2 have not been studied.

Ductility in MgB_2 would allow for continuous drawing of dense wire and other complex shapes without using an expensive batch HIP process and would also provide a means to wind wires into magnet coils without fracturing the MgB_2 core. In this chapter, the high temperature mechanical properties of MgB_2 measured in compression at constant strain rates are presented, showing flow stresses for plastic deformation and the demonstration of compressive strain in excess of 40% and a high strain rate of $6.9 \cdot 10^{-4} \text{s}^{-1}$ without brittle fracture.

3.1. Experimental Procedures

To create dense MgB_2 samples for testing, commercial MgB_2 powder (99%, Alfa Aesar, $< 44 \mu\text{m}$) was packed into a carbon steel tube (9.5 mm OD, x mm ID) and welded shut under vacuum. The sample was hot isostatically pressed, heating to 780 °C under 150 MPa Ar pressure for 1.5 hrs and then heated to 1065 °C under 150 MPa Ar pressure for 4 h, followed by furnace cooling. Rectangular samples $3 \times 3 \times 6 \text{ mm}^3$ were machined from the center of the HIP'd powder (avoiding the reaction layer near the steel tube wall) using a combination of electro discharge machining (EDM) and grinding. Test specimens were contained within a 19 mm ID tungsten-carbide sleeve with tight fitting tungsten carbide top and bottom anvils. Powdered Mg (99%, Fisher Scientific, 200 - 400 μm) was placed around the sample, providing an Mg atmosphere during high temperature experiments preventing decomposition of MgB_2 to MgB_4 and MgB_7 . Samples were tested under static positive pressure Ar atmosphere in compression using a MTS 810 system with servo hydraulic load control, 100 kN load cell, and Centorr vacuum furnace. Samples at 900 and 950 °C were compressed in a series of three initial strain rates from $9 \cdot 10^{-6} \text{s}^{-1}$

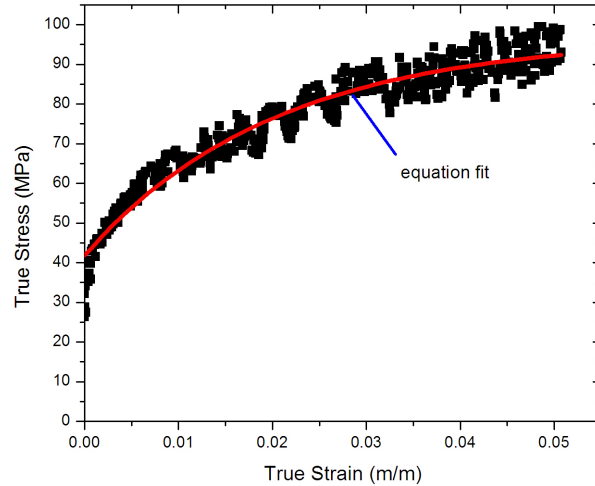


Figure 3.2. Stress vs Strain plot of 950 °C data at a strain rate of $4.3 \times 10^{-5} s^{-1}$ showing $\sigma = \sigma_0 - b^\epsilon$ equation fit to data for determination of flow stress in cases where the stress does not reach a slope of 0. Here the flow stress was determined to be 99 MPa although the data did not level off at that value.

to 0.1 mm displacement followed by $4 \cdot 10^{-5} s^{-1}$ to 0.25 mm displacement and finally at $2 \cdot 10^{-4}$ to 0.50 mm displacement. A specimen tested at 1000 °C was first compressed with the target strain rate of $4 \cdot 10^{-5} s^{-1}$ to 0.42 mm displacement followed by $2 \cdot 10^{-4} s^{-1}$ to 0.53 mm displacement. A final sample was tested at 1000 °C with a target strain rate of $6.9 \cdot 10^{-4} s^{-1}$ to 2.13 mm displacement. True stresses and strain were calculated from the stress and strain data after correction for the load-train displacement measured by generating a compressive strain vs load curve at 900, 950, and 1000 °C without a sample. In ambiguous cases, flow stress was determined by fitting the stress σ vs strain ϵ data to the exponential equation $\sigma = \sigma_0 - b^\epsilon$ where σ_0 is the asymptote of the stress data and thus the flow stress as demonstrated in Figure 3.2.

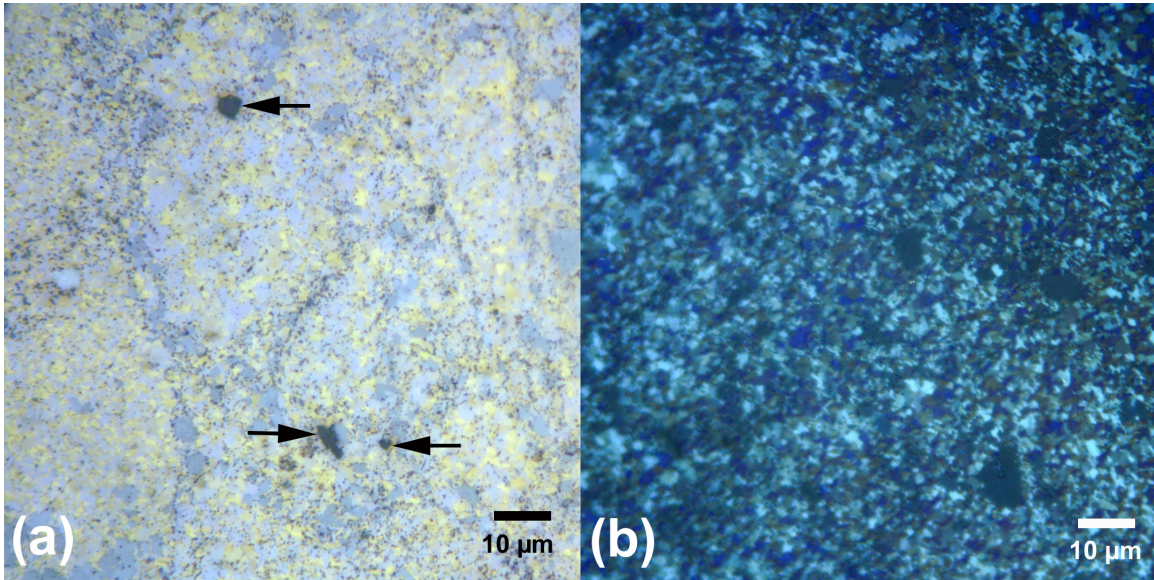


Figure 3.3. Optical micrographs showing as-HIP'd commercial MgB_2 powders. (a) shows dense microstructure with arrows indicating a few small pores. (b) shows fine grain microstructure under cross-polarized light.

3.2. Results

The HIP'd powder specimens had a bulk density of 2.60 g/cc measured from sample dimensions which is more than 99% of the theoretical density of 2.62 g/cc [5]. Optical micrographs show a dense microstructure with a few small pores (Figure 3.3(a)). Reports on commercial MgB_2 powders show agglomerated grains up to 60 μm but individual crystallite sizes of 19 nm [104]. After HIP, polarized light micrographs show small grain size approaching the resolution limit of optical microscopy ($\approx 2 \mu\text{m}$) (Figure 3.3(b)).

The MgB_2 sample tested at 900 °C had flow stresses of 67 - 373 MPa at strain rates of $8.9 \times 10^{-6} \text{s}^{-1}$ to $2.0 \times 10^{-4} \text{s}^{-1}$ as shown in Figure 3.4(a) resulting in a total true strain of 0.19. Testing at 950 °C produced flow stresses of 30 - 214 MPa at similar strain rates (Figure 3.4(b)) with 0.18 total strain. At 1000 °C, flow stresses were 33 - 100 MPa

at strain rates of $8.8 \times 10^{-6} s^{-1}$ to $1.9 \times 10^{-4} s^{-1}$ (Figure 3.4(c)), with a flow stress of 440 MPa measured at the strain rate of $6.9 \times 10^{-4} s^{-1}$ (Figure 3.4(d)). True strain was measured to 0.41 without fracture and 41% deformation was measured by caliper after testing and is visible in Figure 3.5. Large plastically formed cracks were observed after testing (Figure 3.5(c)) suggesting the strain rate might have been too high.

3.3. Discussion

By plotting the strain rate vs flow stress in double logarithm diagram for the three different temperatures, the slope of the data is the stress exponent n according to the creep equation

$$(3.1) \quad \dot{\epsilon} = A\sigma^n \exp\left(\frac{-Q}{RT}\right)$$

where $\dot{\epsilon}$ is the strain rate, σ the flow stress, Q the activation energy, R the gas constant, and T the creep temperature. Stress exponents increased from 1.0 at 1000 °C to 1.8 at 900 °C (Figure 3.6). Stress exponents were similar to the 0.6 to 1.7 found for creep of ZrB₂ at 1600 and 1500 °C respectively [111]. A stress exponent near unity is typical of diffusional creep [95] and has been shown for compressive creep of Si₃N₄ ($n = 1$ at high stress, $n = 2$ at low stress) [98] and SiC ($n = 1.5 - 1.7$) [99]. Creep stress exponents higher than unity may suggest an additional creep mechanism such as cavitation or a change in grain size [98] but an exponent between 1 and 2 is acceptable for diffusional creep [95]. The large cracks observed at the high strain rate and highly strained (41%) material (Figure 3.5) may confirm cavitation is occurring during high strain rates.

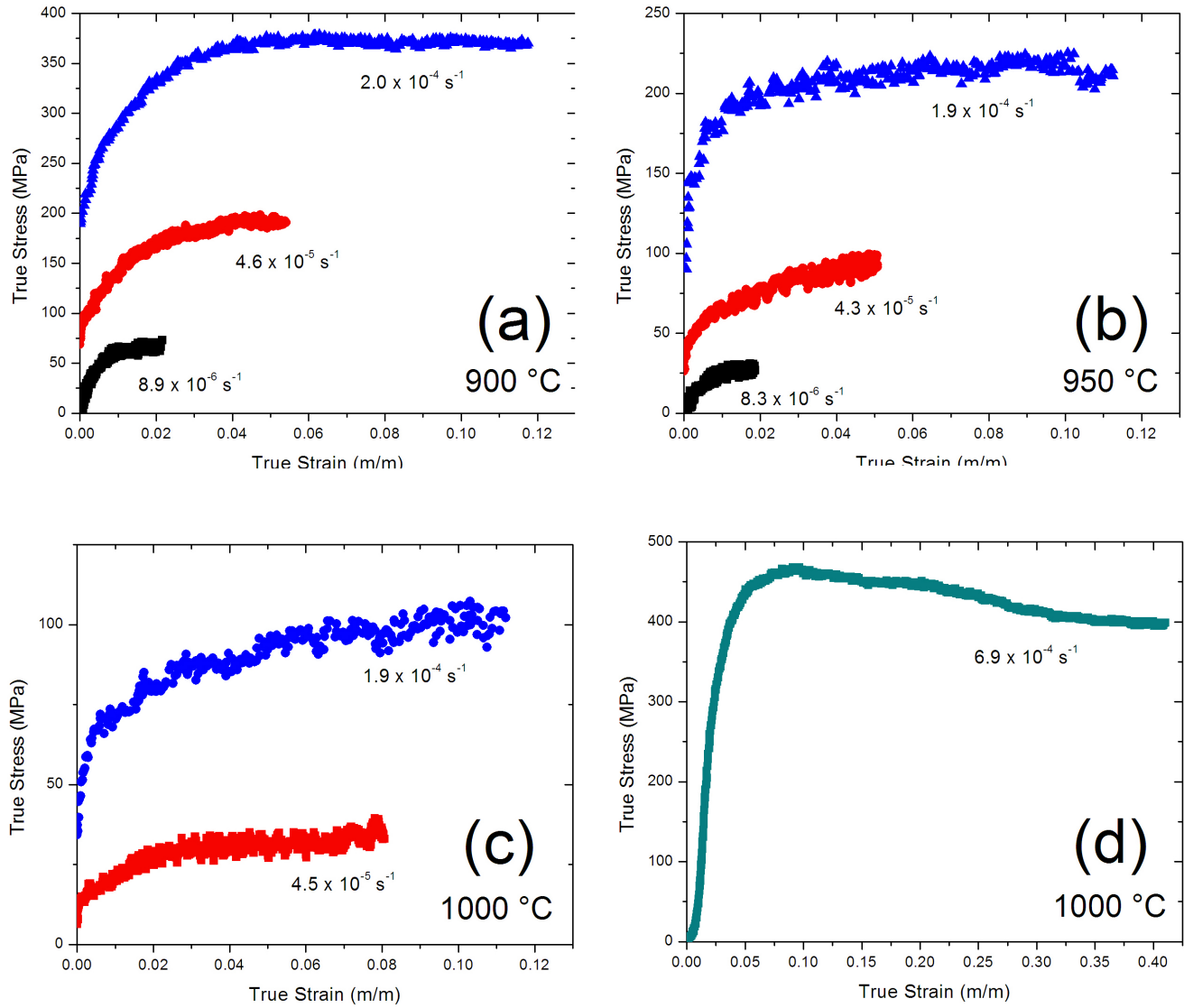


Figure 3.4. HIP'd MgB₂ true compressive stress vs true strain plots of multiple strain rates at (a) 900 °C, (b) 950 °C and (c-d) 1000 °C with (d) showing 0.41 true strain at 1000 °C and a strain rate of $6.9 \times 10^{-4} \text{ s}^{-1}$.

As far as grain growth, optical micrographs after experiments at 900 and 1000 °C (0.19 true strain sample) (Figure 3.7) show no significant change in grain size compared to the as HIP'd condition (Figure 3.3). Many ceramics exhibit grain growth during high

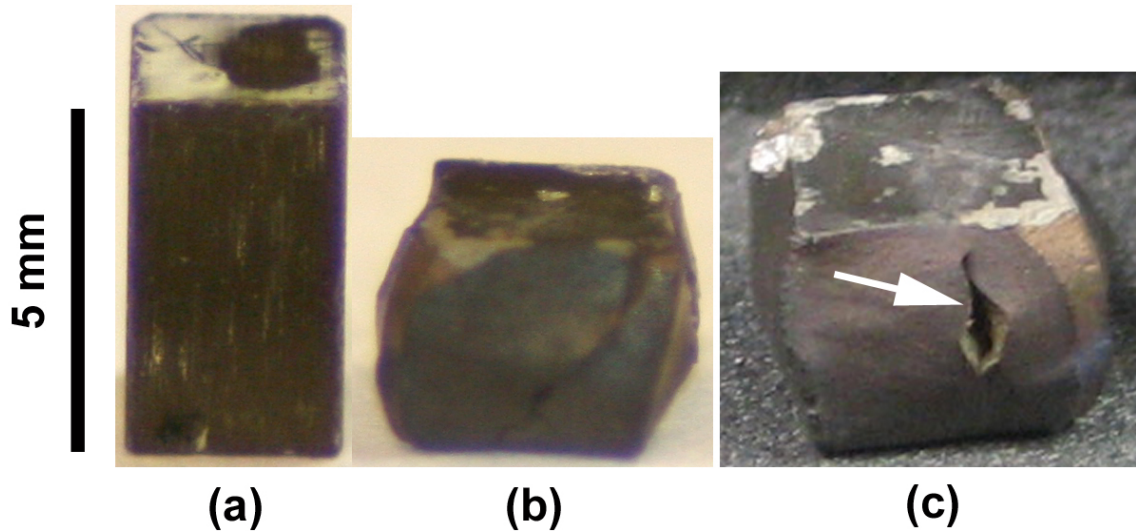


Figure 3.5. Images of HIP'd MgB_2 (a) before and (b-c) after 41% compressive strain at 1000 °C and a strain rate of $6.9 \times 10^{-4} \text{s}^{-1}$ with arrow indicating plastic crack formed during testing.

temperature creep with phases at grain boundaries limiting the growth in the best cases. Testing of MgB_2 samples were completed with less than 2 h at high temperature where grain growth might occur, suggesting 900 - 1000 °C was a low homologous temperature range ($0.51 - 0.55 T_m$ given estimated T_m of 2307 K (Figure 3.1)) and grain growth did not proceed quickly or grain boundaries were pinned by a secondary phase such as MgO or other Mg borides. Small MgO peaks were observed in x-ray diffraction of MgB_2 after experiments at 900 and 1000 °C although no higher borides such as MgB_4 or MgB_7 were detected (Figure 3.8). Other small peaks were not attributed to possible Mg-boride phases or B or Mg oxides and were possibly due to contamination by an outside substance when grinding into powders for XRD study. Studies on commercial MgB_2 powders typically report 2 – 5% MgO in as-received powders [89, 104] although as-received and as-HIP'd powders did not show MgO peaks with XRD here.

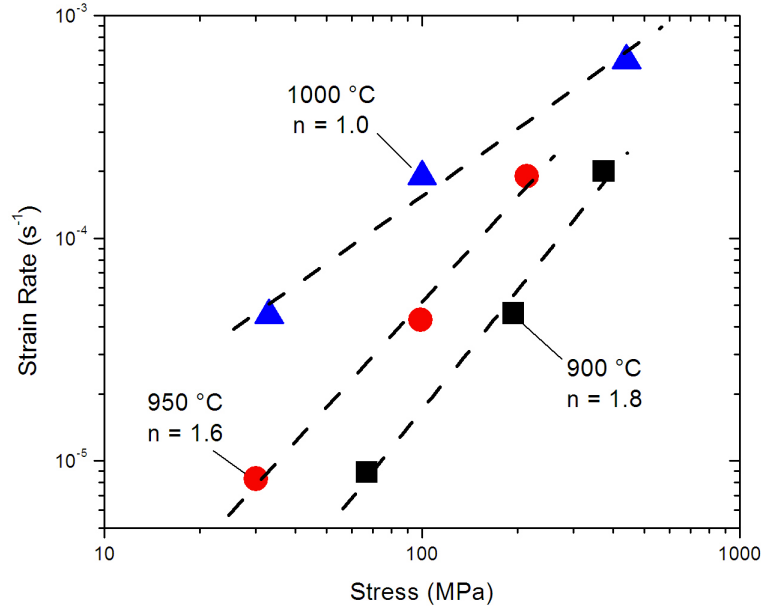


Figure 3.6. Plot of strain rate vs stress in double logarithm diagram showing stress exponents between 1.0 and 1.8 during constant strain rate creep experiments between 900 °C and 1000 °C.

Fitting equation 3.1 to all of the data, a stress exponent of 1.36 ± 0.15 and an activation energy of 241 ± 42 kJ/mol was determined for creep of MgB_2 with the pre-exponential $A = 1.34 \times 10^{-5} m \cdot s/kg$. Plots of equation 3.1 with these parameters are compared to data in Figure 3.9 showing reasonable agreement with data. The activation energy was near that reported for compressive plastic flow in TiB_2 (309 kJ/mol) [109]. The activation energy was also between values discussed for the formation of MgB_2 from Mg and B powders (70 - 146 kJ/mol) and fibers (360 kJ/mol) as discussed in Chapters 2 and 5.

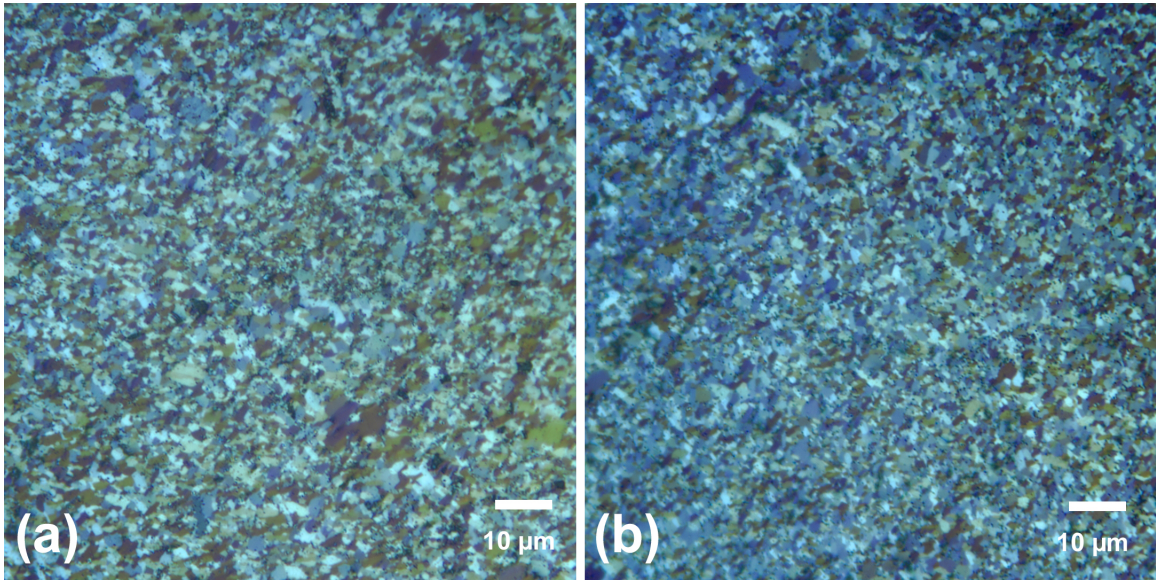


Figure 3.7. Optical micrographs showing fine grained MgB₂ microstructure after compressive creep testing at (a) 900 °C and (b) 1000 °C.

3.4. Conclusions

The most significant result presented here is the large compressive ductility to 41% without fracture at a high strain rate of $6.9 \cdot 10^{-4} s^{-1}$. The ability and degree to which superplastic deformation and high compressive strains are achieved is often engineered by reducing grain size, increasing lattice diffusion, grain boundary diffusion, or adding a second phase that forms a liquid at grain boundaries [112]. Here MgB₂ grains are surely less than 10 μm (Figure 3.3(b)) but exact sizes were not measured because the resolution of optical microscopy would not provide an accurate measurement. In the least, the 41% engineering strain result suggests superplasticity in MgB₂ may be possible and should be investigated further as these results were produced with commercial powders that received no milling, sieving, or purification.

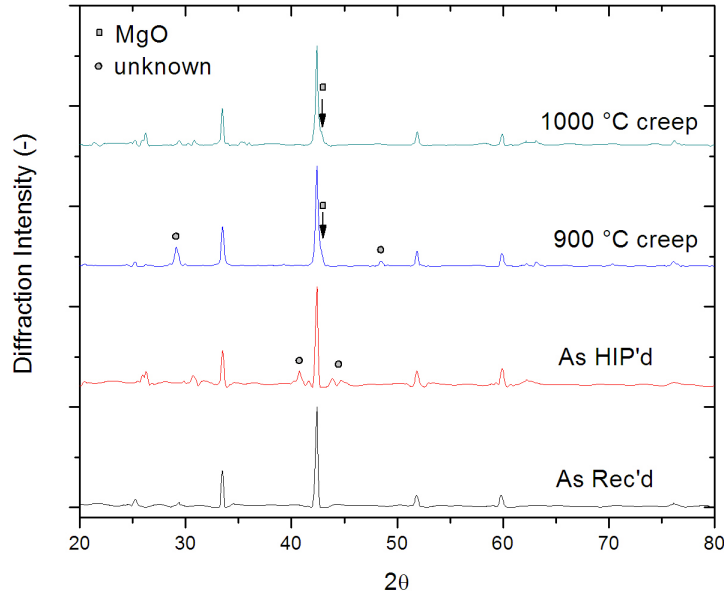


Figure 3.8. Plot of XRD patterns for as-received, as-HIP'd and creep tested MgB₂ showing some MgO in the tested samples and a few other unknown peaks likely contamination from powder preparation but not MgB₇ or MgB₄.

Most MgB₂ studied is reacted in-situ with chemical modifications to increase superconducting properties. These same chemical modifications may also prove to show improved ductility and possibly superplasticity in MgB₂. MgB₂ can be engineered to have small grain size (< 50 nm) through dopants and reduced reaction temperatures [19] without the MgO seen in commercial powders. On the other hand, it may be found that MgO at grain boundaries aids high ductility by slowing grain growth or that dopants may reduce diffusion transport but there must exist some realm where MgB₂ shows appreciable ductility as demonstrated. In that realm, ductility of MgB₂ would directly impact the

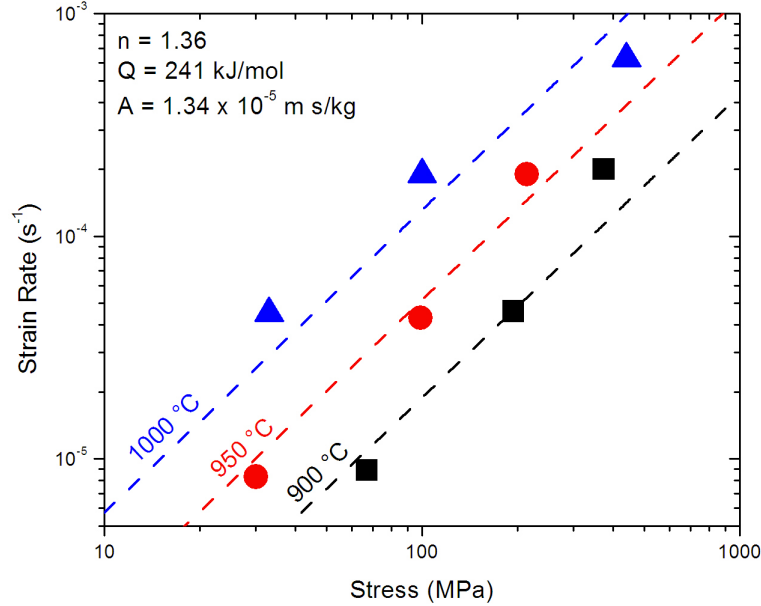


Figure 3.9. Plot of Strain Rate vs Stress in log space showing lines of predicted relationships based on the parameter fits of $n = 1.36$, $Q = 241$ kJ/mol, and $A = 1.34 \times 10^{-5}$ m·s/kg along with experimental data between 900 °C and 1000 °C.

production of superconducting wires through a few scenarios. First, PIT MgB₂ wire production could produce dense MgB₂ cores which has only been realized in HIP'd wires. Second, PIT MgB₂ could return to ex situ processing where MgB₂ powders are reacted in batch form and then added to the metal sheaths and the wire drawing process which is considered a cheaper production route.

Dense ex situ cores should result in similar properties compared to dense in situ cores. The sheath reaction with the powders would also be limited to only the time of high temperature ductile drawing which could be achieved quickly depending on how high a strain rate MgB₂ can achieve. Even if MgB₂ can only withstand 40% strain, wires could be

drawn at room temperature as they are now in several reduction steps, reacted (in the case of in situ) and then drawn at high temperature to final dimensions, fully densifying the powders. If MgB_2 can achieve superplastic forming strains and strain rates, all drawing could be done at high temperature in possibly a single step with nearly 100% deformation. Furthermore, PIT MgB_2 wires could use thinner sheath materials since powders would no longer need to be crushed under high stresses but would be ductile. A thinner wire wall would increase the overall engineering critical current density compared to a similar core with thicker sheath. The extent of ductility and effect on superconducting properties will further promote the engineering of superconducting MgB_2 wires.

CHAPTER 4

In Situ Synthesis of Mg/MgB₂ Fiber Composites

Another method for producing thin MgB₂ wires is to react B fibers with Mg vapor at 950 °C [7, 10, 51, 73, 113]. The resulting free-standing MgB₂ fibers are superconducting at 39.4 K, exhibit much lower normal-state resistivity than bulk MgB₂, and have J_c values of $4 \cdot 10^5 A/cm^2$ at 5 K and zero-field [7]. However, these reacted MgB₂ fibers are brittle and their shape is extensively deformed (warped and bent) from the original straight, cylindrical shape of the B fibers.

In this chapter, an in-situ processing route which results in an Mg matrix composite containing straight, cylindrical, continuous MgB₂ fibers is discussed. The composite is created by infiltrating a preform of B fibers with liquid Mg and subsequently reacting these two phases at elevated temperatures. For the resulting MgB₂ fibers, T_c was slightly above 39 K and J_c was $3.6 \cdot 10^5 A/cm^2$ at 5 K and zero-field.

4.1. Processing

Boron fibers (from AVCO, with a diameter of 140 μm , a 15 μm tungsten core and a nitrided surface) were cut to 25 mm length from a continuous spool. The fibers were bundled into an aligned preform which was placed in an iron tube (from Goodfellow, Lancaster, PA, with 8 mm inside diameter) crimped and welded on one end. The 670 fibers had a total mass of 0.652 g, corresponding to a preform volume fraction of 20.5%. Two magnesium cylinders (from Alfa Aesar, Ward Hill, MA, with 7.9 mm diameter and

4.411 g total mass) were placed on top of the preform of aligned fibers. The crucible was placed in a pressure infiltrator [48] where it was heated under vacuum to 800 °C and held for 30 min to ensure melting of the magnesium, which created a liquid seal above the fiber preform. Argon was then introduced in the infiltrator and its pressure was increased to 3.2 MPa in 2 min, forcing the liquid Mg into the evacuated space between the B fibers. After reducing the pressure to 0.1 MPa, the temperature was increased to 950 °C and the composite was heat-treated at that temperature for 2 h. The composite was then cooled to 650 °C in 23 min under a pressure of 1.4 MPa (to enhance cooling and feed shrinkage porosity) and subsequently cooled to 200 °C in 85 min. A control specimen was produced in a similar manner, except that cooling followed immediately after the infiltration step at 800 °C.

4.2. Characterization Procedures

The samples were sectioned and polished following standard metallographic procedures by first grinding with 400 grit SiC paper until flat followed by polishing steps with 9, 3, and 1 μm diamond paste on cloth. The microstructure was observed with an optical microscope (using normal and cross-polarized light) and with a scanning electron microscope (SEM, Hitachi S-3500N) capable of energy dispersive x-ray spectroscopy (EDS). A 2 mm thick polished cross-section of the heat-treated composite was analyzed using time-of-flight secondary-ion mass spectrometry (ToF-SIMS, Physical Electronics, PHI TRIFT III) with 25 keV energy and a 700 μm x 700 μm raster size after in-situ gallium-ion sputtering to clean the surface. X-Ray diffraction (XRD) was performed using a Rigaku D/MAX-IA diffractometer ($\lambda = 0.154\text{nm}$) on a portion of the heat-treated composite

that had been ground into powder with mortar and pestle. Individual fibers were also extracted by dissolving the Mg matrix from a 9 mm long section of the reacted composite with a 10% HCl solution. Using the same HCl solution, a section of the composite was deep-etched to reveal the morphology of the fibers protruding from the matrix. Superconducting properties were determined on a single fiber, 6.4 mm long and 192 μm in diameter, using a superconducting magnetometer (Quantum Design MPMS5). The fiber was mounted perpendicular to the applied field, cooled under 100 Gauss and then warmed under zero-field to determine T_c . Critical current densities were calculated inductively at 5 K and 20 K from M-H loops for the same fiber.

4.3. Results and Discussion

Observation by optical and electron microscopy of polished cross-sections showed that the reacted composite was dense, with no significant porosity produced through the synthesis reaction or subsequent solidification. The control specimen cooled after infiltration without heat-treatment showed no chemical reaction between the B fibers and the Mg matrix (Figure 4.1(a)), as reported previously for similar Mg/B fiber composites [114]. Fast reaction to MgB_2 using liquid Mg infiltration was observed in a study [48] with B powders at 800 °C, resulting in choking and preventing complete infiltration of the B preform. This difference in reaction rate is most likely due to the much higher specific surface area of the discontinuous B powders (less than 44 μm in size) [48], as compared to 140 μm continuous B fibers.

After the 2 h heat-treatment at 950 °C, several observations indicated that the B fibers had been converted to MgB_2 . First, the B fibers had grown to diameters of $196 \pm 6\mu\text{m}$,

(Figure 4.1(b)), equivalent to the value of $191 \pm 10 \mu\text{m}$ reported for MgB_2 fibers synthesized by reaction between free-standing $140 \mu\text{m}$ B fibers and Mg vapor [7]. This diameter compares well with a value of $190 \mu\text{m}$ calculated assuming that volume growth occurs in the radial direction only (with this assumption, the volume fraction MgB_2 fibers is calculated as 40.2% in the reacted composite). Second, the only boride in thermodynamic equilibrium with excess liquid or solid Mg is MgB_2 [45]. Indeed, only MgB_2 was found after B powders were reacted with liquid Mg at $800 \text{ }^\circ\text{C}$ [48]. Third, the cross-section of reacted fibers exhibited birefringence when observed under cross-polarized light (Figure 4.3), a characteristic of bulk MgB_2 . Fourth, the SIMS measurements showed the presence of both Mg and B within the fibers (Figure 4.4). Direct proof of MgB_2 synthesis was provided by XRD analysis of the composite, showing only Mg and MgB_2 peaks. Additionally, an extracted fiber was found to be superconducting at a critical temperature slightly above 39 K (Figure 4.2), in good agreement with the value of 39 K for bulk MgB_2 [1]. The critical current density of that fiber was calculated under zero field conditions as $3.6 \cdot 10^5 \text{ A/cm}^2$ at 5 K and $2.1 \cdot 10^5 \text{ A/cm}^2$ at 20 K. Nearly the same values were found for free-standing MgB_2 fibers synthesized by reaction of B fibers with Mg vapor [7].

Unlike the irregular shape of the MgB_2 fibers produced by reaction in gaseous Mg [7], the present MgB_2 fibers created by reaction with liquid Mg retained their original cylindrical shape (Figure 4.1(c)). Most of the fibers extracted by dissolution of the matrix had the same length as the composite specimen piece being dissolved (9 mm) and were straight. This was probably due to the much more uniform flux of Mg atoms provided by the Mg melt in direct contact with the B fibers, allowing a uniform diffusion front within the fibers, and thus a uniform volume expansion. However, this volume expansion

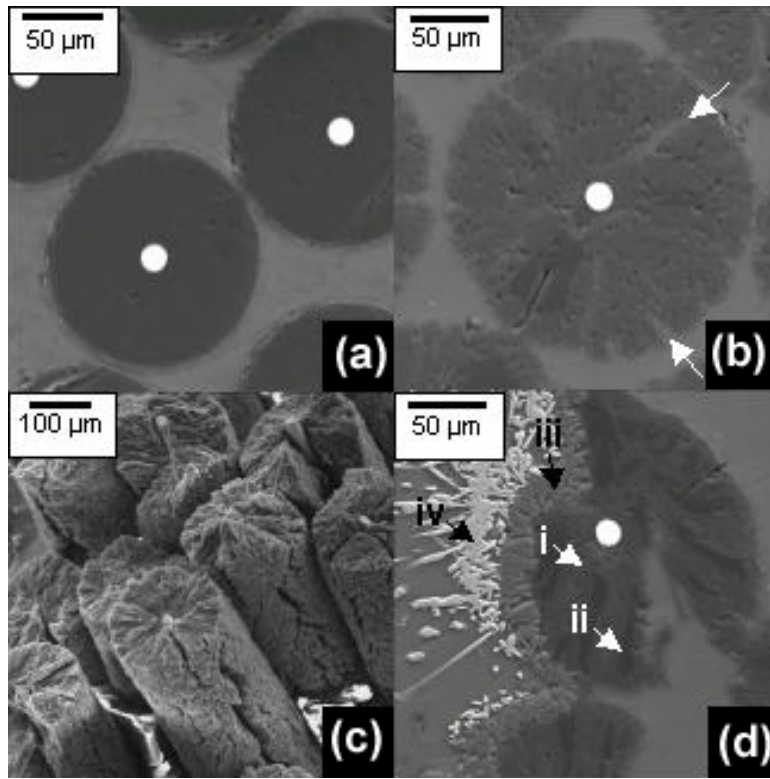


Figure 4.1. Scanning electron micrographs showing shape and morphology of infiltrated B fibers before and after heat-treatment. (a), Un-reacted composite showing magnesium matrix with 140 m diameter B fibers. (b), Reacted composite showing a 193 m diameter MgB_2 fiber in Mg matrix, with radial cracks infiltrated with Mg. (c), Deep-etched reacted composite showing parallel, cylindrical MgB_2 fibers with radial cracks. (d), Reacted fiber near iron crucible wall with (i) MgB_2 , (ii) un-reacted B, and (iii, iv) two Fe-Mg-B phases with various amounts of Mg.

($\Delta V/V = 0.90$) was also probably responsible for the radial cracks observed for most fibers (Figures 4.1(b-c) and 4.3). The cracks were filled with magnesium, which indicates that they formed during synthesis from the volumetric change, and not upon subsequent cooling from the mismatch in thermal expansion between Mg and MgB_2 . Also, most MgB_2 fibers contained un-reacted MgB_4 in small, isolated radial slivers, which were visible under cross-polarized light (Figure 4.3), but with a volume fraction too low to be measurable by

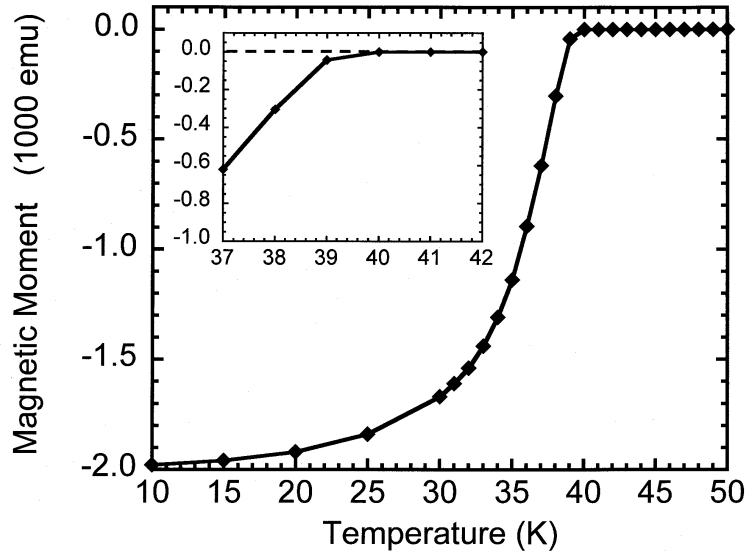


Figure 4.2. Magnetic moment vs. temperature under zero field conditions for single MgB_2 fiber extracted from the reacted composite. Inset shows T_c slightly above 39 K.

XRD. These slivers were on average $10 \mu\text{m}$ wide and $40 \mu\text{m}$ long. Finally, the fiber/matrix interface appeared well bonded (Figures 4.1(b), 4.3), of importance for the mechanical properties of these composites.

Fibers nearest to the iron crucible wall (but within the Mg matrix) were only partially reacted to MgB_2 and exhibited two other phases without birefringence (Figure 4.1(d)): (i) a phase which grew outwardly from the fiber and seemed to precipitate discontinuously from the liquid in a starburst pattern; and (ii) an inner phase with the same morphology as MgB_2 and in contact with the MgB_2 phase formed near the center of the fiber. These two phases consisted of magnesium-iron-boron ternary compounds, as observed with EDS, but were too scarce to be detectable by XRD. The EDS analysis indicated that the outer phase contained less magnesium than the inner phase. Significant transport of Fe from

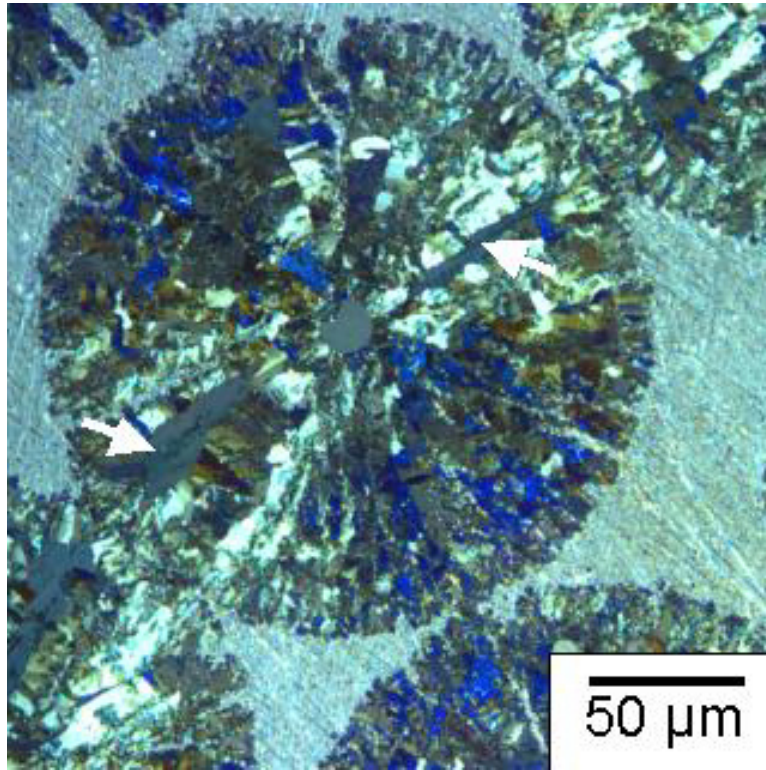


Figure 4.3. Optical micrograph of 200 m MgB_2 fiber in Mg matrix under cross-polarized light. Arrows indicate slivers of non-birefringent material (MgB_4). A $15 \mu\text{m}$ W-B core is located at the center of the MgB_2 fiber. The interface between the matrix and fiber is well bonded.

the crucible walls to the B fibers was likely during the 2h heat-treatment, since $0.10\text{at}\%$ Fe can dissolve into liquid Mg at $950 \text{ }^\circ\text{C}$ [115]. This reaction with Fe, which affects a small minority of the fibers, could be eliminated by coating the iron crucible with a ceramic layer stable with respect to liquid Mg (e.g., MgO or Y_2O_3) or by using a crucible material with much lower solubility in liquid Mg (e.g., Ti or Ta) [115].

4.4. Process Comparison

As compared to the PIT method which produces a large, monolithic MgB_2 core surrounded by a metallic casing, a composite consisting of several hundreds of fine MgB_2

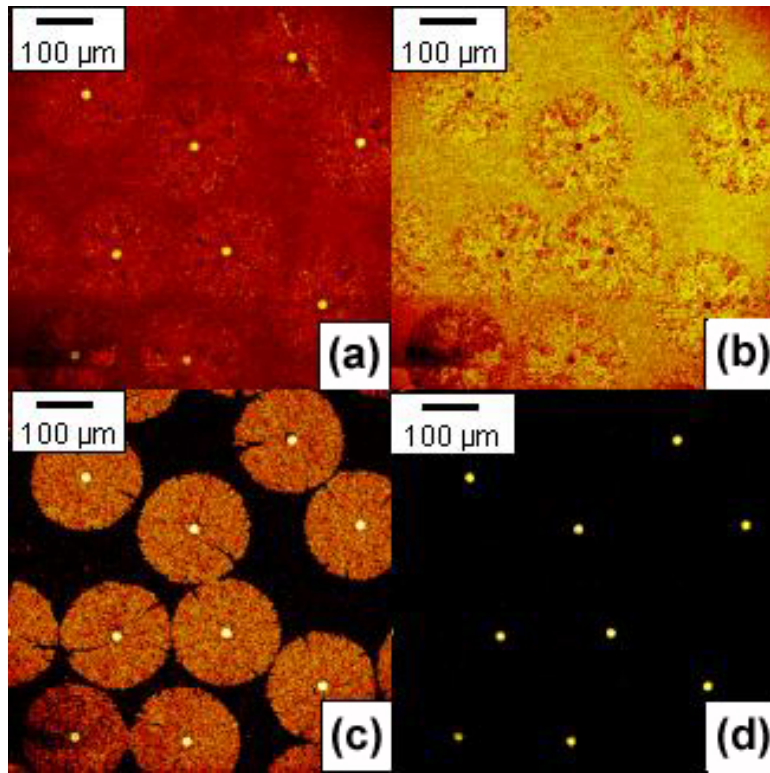


Figure 4.4. SIMS elemental maps in reacted composite. (a), Total ion image. (b), Mg ion image, showing Mg in both matrix and fibers (except fiber cores). (c), B ion image, showing B exclusively within the fibers (and fiber cores). (d), W ion image, showing fiber cores.

fibers embedded in a continuous matrix presents several advantages: damage due to mechanical overload can be distributed over a large volume between individual fibers, as compared to a single crack severing a superconductive PIT core; also, heat extraction is faster in the case of individual fibers, of importance for rapid cooling and in case of localized superconductivity break-down. Drawbacks include higher materials costs for the B fibers used in the present process, as compared to MgB_2 or $\text{Mg} + \text{B}$ powders used in the PIT process. Also, the present composite process is more complex, as liquid Mg must be infiltrated into the B fiber perform, as compared to the simple drawing of a powder

filled tube. However, when compared to the multi-step fabrication of multi-filamentary PIT wires [42, 104], the processing complexity is probably similar. The multi-filamentary PIT processes will however be unable to match the high MgB_2 fiber volume fraction of the present composite process (for which close-packed densities in excess of 90% can easily be reached) without using extremely thin wall metal tubes.

As compared to the gas-phase synthesis of MgB_2 fibers [7, 10, 51, 73, 113], the liquid-state synthesis also offers several advantages. First, straight, cylindrical fibers are synthesized and these fibers can thus be packed much more efficiently to high volume fraction composites, as compared to gas-phase fibers whose shape is deformed. Second, the fibers are synthesized in-situ within a tough, strong, conductive Mg matrix, whereas gas-phase synthesized fibers must be incorporated into a metallic or organic matrix in a separate step, raising the risks of breakage during fiber packing and matrix addition. Finally, and possibly most importantly, the present liquid-state process can easily be scaled up to the efficient and cost-effective production of continuous lengths of superconducting cables, since liquid metal infiltration is capable of creating several hundreds of meters of ceramic fiber/metal composites [85]. By contrast, the creation of long lengths of composites with undamaged gas-phase synthesized MgB_2 fibers would be very challenging.

4.5. Conclusions

The synthesis of a composite, consisting of several hundred MgB_2 continuous fibers (with 40% volume fraction) aligned within a continuous Mg matrix, was achieved by infiltration of a B fiber preform with liquid Mg and subsequent in-situ reaction at 950 °C. This processing route avoids the handling difficulties of brittle and deformed MgB_2

fibers synthesized in the vapor phase. It is adaptable to continuous infiltration techniques to produce kilometer-length composite wires where a large number of fine MgB_2 fibers are embedded within a Mg matrix, which provides enhanced strength, toughness, and thermal and electrical conductivities. The MgB_2 fibers exhibit a critical temperature slightly above 39 K and a critical current density of $3.6 \cdot 10^5 \text{ A/cm}^2$ at 5 K and zero-field, comparable with the best results of bulk MgB_2 .

CHAPTER 5

Reaction Mechanisms and Kinetics of MgB₂ Fiber Synthesis

Chapter 4 showed an in situ composite consisting of an Mg matrix containing straight continuous superconducting MgB₂ fiber could be synthesized from infiltration of commercial B fibers by liquid Mg followed by heat treatment for 2 h at 950 °C. This reaction time was similar to reported for vapor reacted fibers [7] but no other reaction times for the reaction of fibers have been reported. In this chapter, the reaction kinetics of the synthesis of MgB₂ fibers from commercial B fibers in liquid Mg is investigated and modeled to determine mechanisms and kinetic parameters such as rate constants, diffusion coefficients, and activation energy.

5.1. Experimental Procedures

Commercial B fibers with 99.999% purity and 140 μm diameter (from Specialty Materials, Inc., Lowell, MA) were placed within a 100 mm long pure titanium crucible with 8 and 9.5 mm inner and outer diameters and pressure infiltrated with liquid Mg at 800 °C [48, 116]. Titanium was selected as crucible material because it does not react with liquid or gaseous Mg vapor [115] and has much lower x-ray absorption than other metals (Fe, Ni, Cu, Nb or Ta) used as PIT tubes. A 20 mm long section at the end of the crucible was thinned to 8.5 mm outer diameter, resulting in 0.25 mm thick walls, to reduce the

absorption and scattering of X-rays by the crucible. A K-type thermocouple was introduced in a small hole machined at the lower part of the crucible which was sealed with a carbon-steel compression fit cap and placed within a quartz tube.

Diffraction experiments were performed at the Advanced Photon Source (Argonne National Laboratory, IL) using the beamline end station 5-BM-D (DuPont-Northwestern-Dow Collaborative Access Team Synchrotron Research Center). An infrared furnace heated the crucible through the evacuated quartz tube to 500 °C in 5 min, followed by a 5 minute hold. The quartz tube was then backfilled with 0.33 atm of argon, maintained constant during the experiment, and the crucible was heated in 5 min to the reaction temperature chosen in the range 885-1025 °C (i.e., above the 650 °C melting point of Mg). Heating was rapid enough to prevent any significant reaction to occur prior to reaching the final temperature, as ascertained by diffraction. The reaction was monitored in-situ by a 65 keV ($\lambda = 0.019 \text{ nm}$) synchrotron x-ray beam with a square 1 x 1 mm cross-section, positioned perpendicularly to the crucible walls and penetrating through both quartz and titanium walls, as shown schematically in Figure 2.1. Transmitted diffraction rings were recorded, after 30-120 s. exposures times, on a 150 mm diameter charge-coupled device camera (Photonic Science Limited, UK) placed at about 380 mm from the sample.

The intensity of the diffraction rings was first integrated over their circumferences to create plots of intensity vs. 2Θ as discussed in Chapter 2 (where Θ is the diffraction angle), using FIT2D software [91]. The intensity of the $(10\bar{1}1)$ MgB_2 peak (after background subtraction shown (Appendix A) and integration over a typical 2Θ range of 4.9-5.2° using JADE 6.5 powder diffraction software) was determined for each diffraction pattern. This

intensity, divided by the integrated intensity after full reaction, provides the degree of reaction representing the volume fraction of reacted B.

To further aid in determining reaction mechanisms and kinetics, microstructural evolution of reacted fibers were analyzed ex situ using optical microscopy. Thicknesses of MgB_2 and other observed boride phases (MgB_4 and MgB_7) were measured at early stages of the reaction of B fibers with liquid Mg by cooling the sample to room temperature after a particular time at temperature followed by sectioning, mounting, and metallographic grinding and polishing to a $1 \mu\text{m}$ finish. Fibers reacted at $1000 \text{ }^\circ\text{C}$ were analyzed after 1, 2, 3, and 5 minutes with fibers reacted at $900 \text{ }^\circ\text{C}$ analyzed after 15, 40, 60, and 100 minutes. Fibers reacted at $800 \text{ }^\circ\text{C}$ were studied after 1, 2, 3, 4, and 5 days while fibers reacted at $700 \text{ }^\circ\text{C}$ were studied after 21, 54, and 123 days.

5.2. Results and Discussion

5.2.1. In Situ Reaction Kinetics

In situ synchrotron diffraction experiments showed reactions completed after 1 - 10 hours at temperatures between 885 and $1025 \text{ }^\circ\text{C}$, as shown in Figure 5.1. Reaction curves appeared sigmoidal in shape with a short incubation period to a few percent reaction followed by an increase in reaction rate to about 80% reaction and then a slowing of the reaction to 100% completion which is expected since diffusion must take place through a large reaction product layer to complete the reaction to MgB_2 .

Following the derivation by Carter [92] for the reaction of spheres, the equation

$$(5.1) \quad -kt = \frac{r_0^2 \left(x \ln \left(\frac{1-x+zx}{1-x} \right) + zx \ln \left(\frac{1-x}{1-x+zx} \right) + z \ln \left(\frac{1}{1-x} \right) + \ln \left(\frac{1-x}{1-x+zx} \right) \right)}{4(z-1)}$$

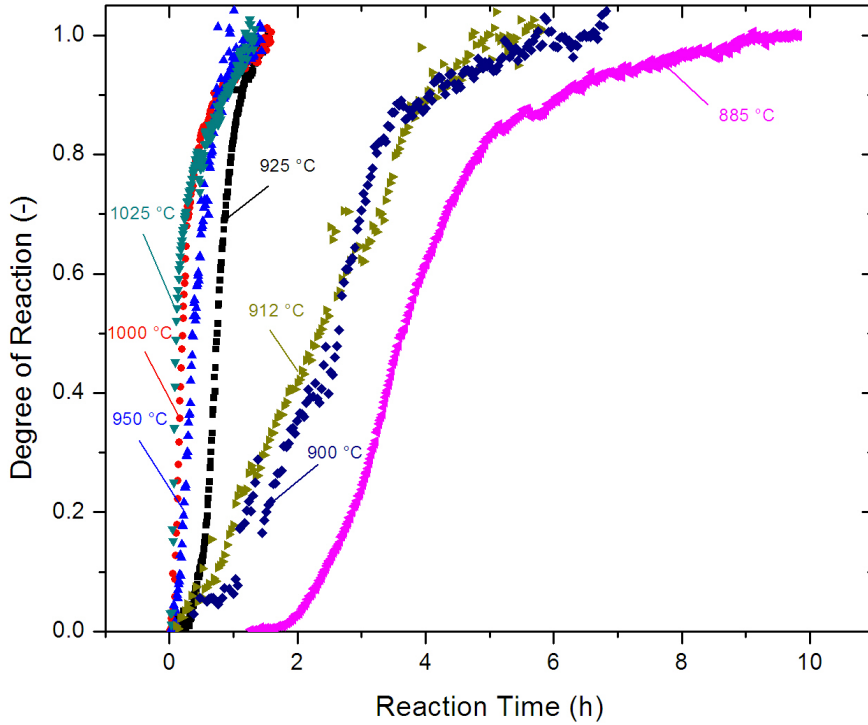


Figure 5.1. Synchrotron x-ray diffraction degree of reaction vs time curves for 140 μm diameter B fibers reacted in situ in liquid Mg.

was derived for the degree of reaction of a cylinder (Appendix B.2) where z is the volume expansion coefficient ($z = 1.90$ for MgB_2 from B [5]), r_0 is the initial fiber radius, x is the degree of reaction, t is reaction time and k is the reaction rate constant. The right hand side of the equation should linearize degree of reaction data for a cylinder and the negative slope of the equation when plotted with time is the reaction rate constant k . In situ degree of reaction data was not well fit with the equation, as expected, since degree of reaction vs time for a cylinder should be parabolic according to Equation (5.1) and measured reaction curves were sigmoidal in shape (Figure 5.1). However, after removing early reaction time

data from incubation, fits improved (Figure 5.2(a)) and the reaction rate constant was calculated from the slope. Reaction rate constants ranged from $6 \cdot 10^{-14}$ to $4 \cdot 10^{-13} m^2/s$ with the highest rate constant at 925 °C rather than the higher temperatures of 950-1025 °C. Best fits were obtained by only fitting the linear middle section of the reaction curves where the reaction rates were fastest (Figure 5.2(b)). Here reaction rate constants ranged from 10^{-13} to $10^{-12} m^2/s$ with the fastest rates at 1000 and 1025 °C. An Arrhenius plot of the rate constants on log scale vs inverse temperature shows activation energies of 106 - 180 kJ/mol for the two fits described above (Figure 5.3). The fit with early incubation data removed has two outliers corresponding to the reactions at 925 and 950 °C, while the fits to only the middle section of the reaction curves showed a more linear trend. Rate constants between 885 and 912 °C were over three orders of magnitude higher than rate constants calculated with the Carter derived sphere model for the reaction of Mg with B powders at 900 °C (Chapter 2). With rate constants from the powder study at 900 °C, fiber reaction time would be xx days instead of hours. Based on this difference in rate constants as well as the lack of fit with the model, the reaction of boron fibers in liquid Mg is likely not a typical diffusion regulated process.

5.2.2. Ex Situ Reaction Kinetics Measurements

In examining partially reacted fiber microstructures, three Mg based boride layers were observed in reactions at 900 and 1000 °C. As reported in other studies [52, 55] and according to the Mg-B phase diagram [45] (Figure 1.3), MgB_{20} , MgB_7 , MgB_4 , should form before the reaction reaches equilibrium with MgB_2 forming in the presence of excess Mg. Optical micrographs in Figures 5.4 and 5.5 show that at reactions at 900 and 1000

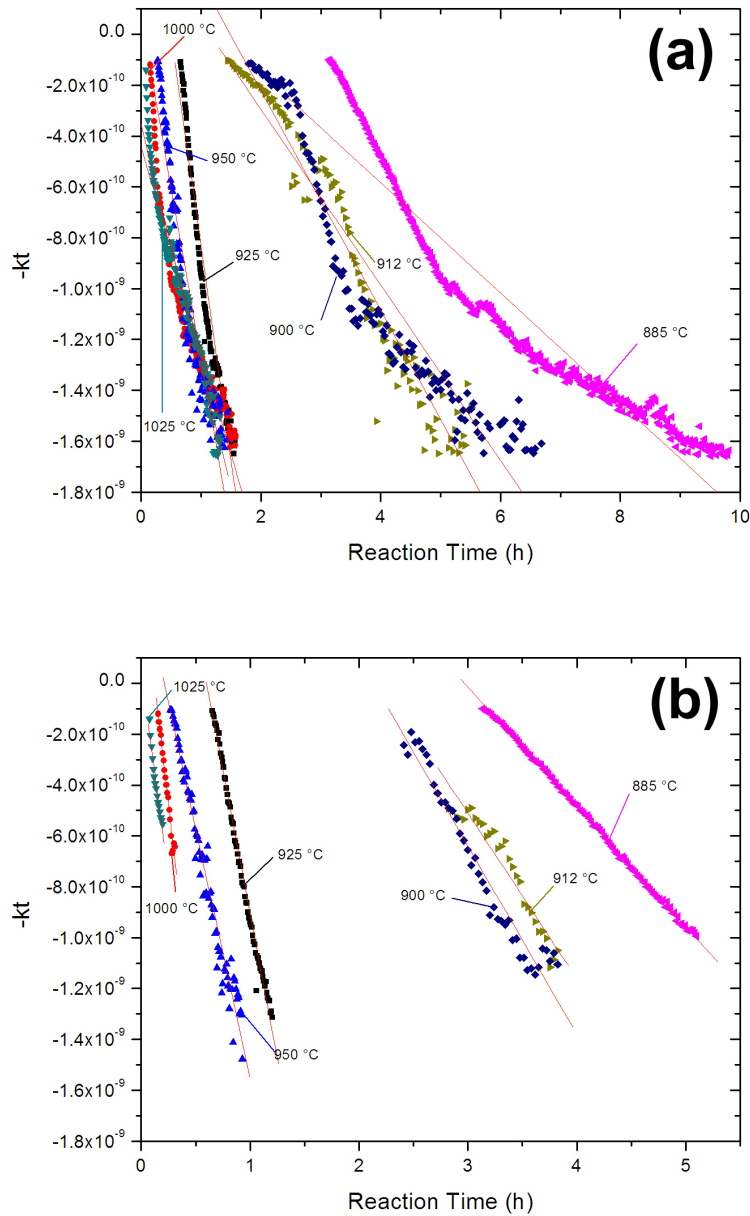


Figure 5.2. Fits of Carter cylinder model (Equation (5.1)) to in situ synchrotron data with (a) showing fits to the data after removal of incubation data and (b) showing fits to the middle most linear section of reaction curves.

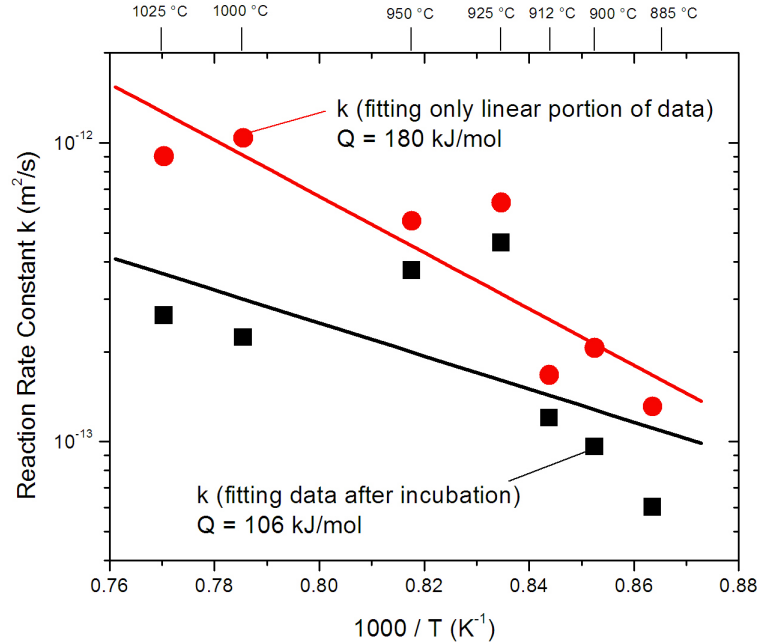


Figure 5.3. Arrhenius style plot of reaction rate constants vs inverse temperature showing activation energies between 106 and 180 kJ/mol.

°C, an MgB_2 shell grew from 1-10 μm thick on the outside of the fiber with a thicker MgB_4 layer, 10 to 40 μm in thickness, inside of it. Finally, a ring of MgB_7 layer which was only 1-2 μm thick during reactions at 1000 °C and about 15 μm thick at 900 °C did not grow faster than the MgB_4 growth front, but penetrated further into the fiber ahead of the MgB_4 growth front with a consistent thickness, was seen before the unreacted B and the W-B core. The MgB_4 growth layer was observed to contain cracks where wedges of MgB_2 span the length of the layer. This observation proved that MgB_2 did not grow with a smooth growth front and explained why the cylinder model was not a good fit for the in situ data between 885 and 1025 °C as shown in Figure 5.2. Additionally, there are wedges of magnesium infiltration into cracks in the MgB_2 and MgB_4 region, as shown in

Figure 5.4(d). At 700 and 800 °C, optical micrographs in Figures 5.6 and 5.7 showed the MgB₂ shell grew from 1-10 μm over the reaction times but a large MgB₄ layer was not seen. The MgB₇ layer grew from 25 to 50 μm ahead of the MgB₂/MgB₄ growth front. Although no significant amount of MgB₄ was observed, thermodynamically it must be present so it was assumed to be a very thin region not observed with optical microscopy. Without the MgB₄ region, no cracking front with MgB₂ wedges was observed as at 900 and 1000 °C, however, random sporadic cracking, as visible in Figure 5.6(e), with MgB₂ growing within the cracks was observed.

It is proposed that the fibers were reacting with both a diffusion mechanism and a cracking mechanism. The cracking mechanism was based on one of two theories or a combination of them. The first theory requires the MgB₄ layer to crack and be infiltrated by liquid Mg which immediately converts MgB₄ to MgB₂. As discussed, the volume expansion of forming MgB₂ from B is a 90% volume increase (volume expansion coefficient of 1.90), which is a combination of the 18% increase of forming MgB₇ from B, a 24% increase of forming MgB₄ from MgB₇, and a 29% increase from forming MgB₂ on MgB₄. The large volume change and considerable thickness of the MgB₄ layer observed at 900 and 1000 °C created large stresses and eventually cracked the MgB₄ layer allowing liquid Mg to infiltrate and react the MgB₄ into MgB₂ within the crack. For the reaction of MgB₄ and Mg to progress at the MgB₄ growth front, the continued reaction must be persistently cracking the MgB₄ and MgB₂ at the micrometer scale not seen in the micrographs allowing Mg to infiltrate and continue the reaction of MgB₄ to MgB₂ ahead of the normal MgB₂ growth front. The second theory assumes that the wedges of MgB₂ form between radial columnar grains of MgB₄ due to diffusion of Mg along the MgB₄ grain boundaries. Grain

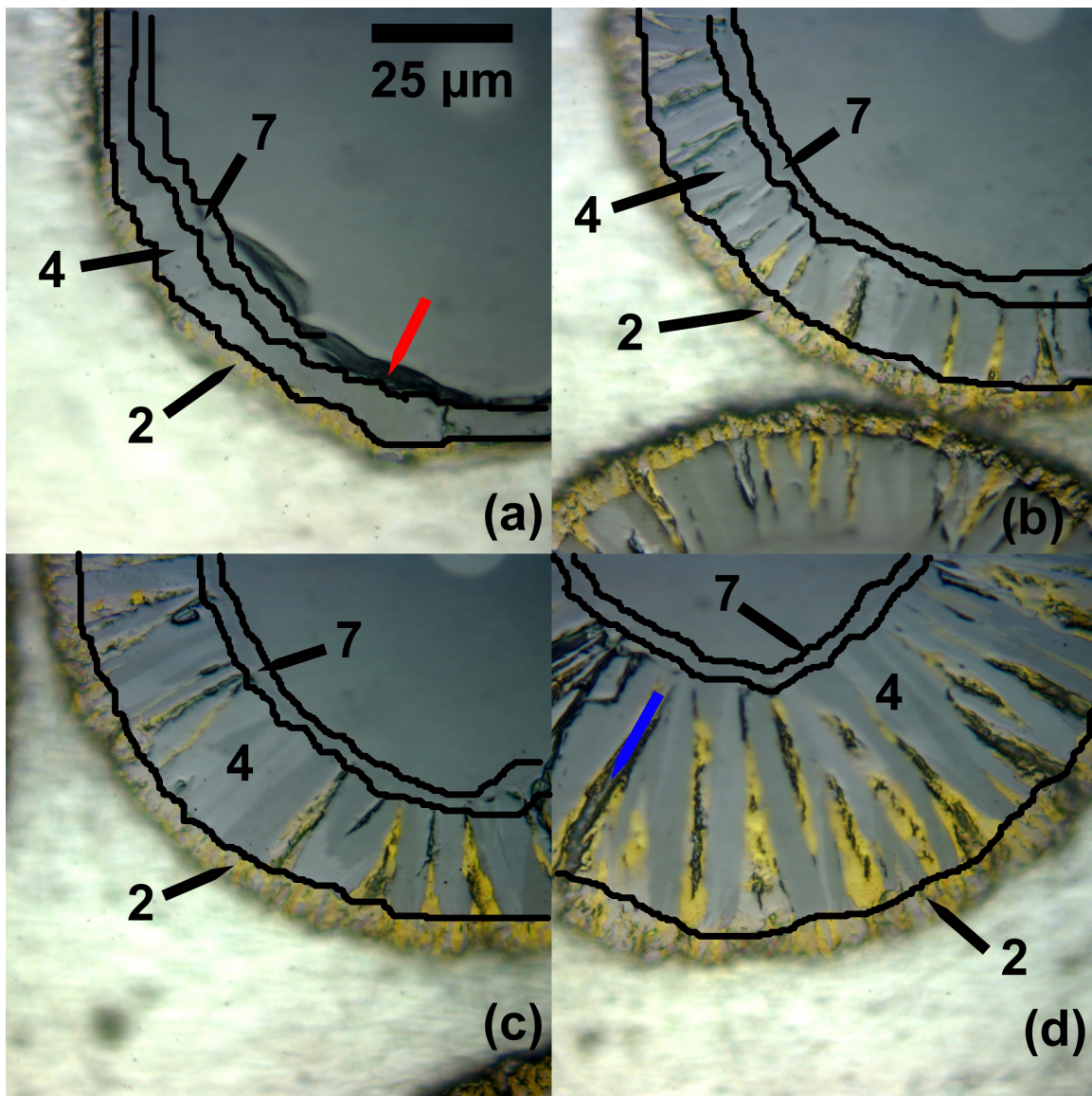


Figure 5.4. Optical micrographs of fibers reacted at 1000 °C for (a) 1 min, (b) 2 min, (c) 3 min, and (d) 5 min showing MgB₂, MgB₄, and MgB₇ growth fronts as indicated by white arrows. The blue arrow highlights a crack in the MgB₂ infiltrated by Mg with the red arrow indicating a fiber crack not due to reaction but likely from sectioning or metallographic preparation.

boundary diffusion is much faster than lattice diffusion which explains why the MgB₂ wedges span the length of the MgB₄ region. However, why only some of the grains have

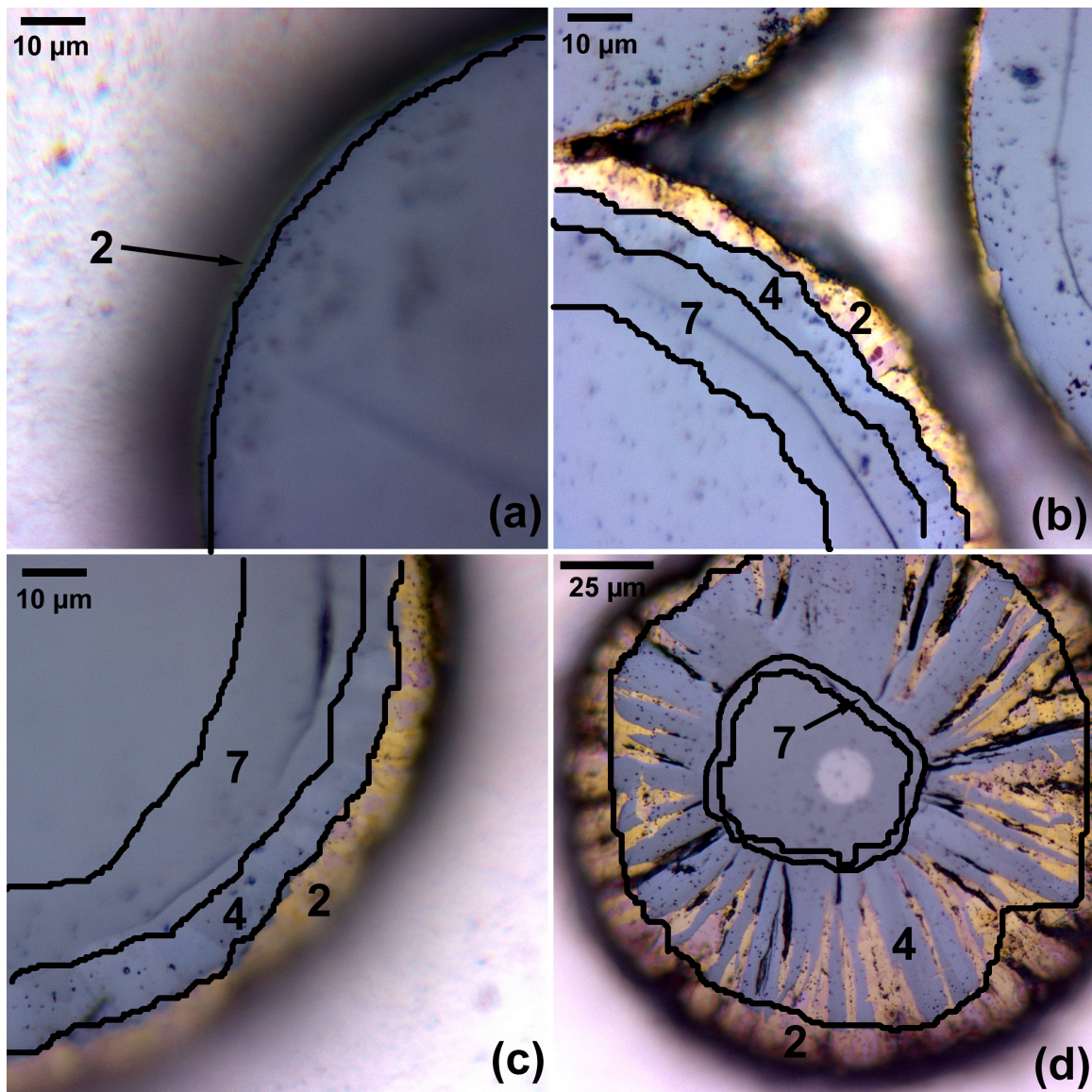


Figure 5.5. Optical micrographs of fibers reacted at 900 °C for (a) 15, (b) 40, (c) 60, and (d) 100 min showing MgB_2 , MgB_4 , and MgB_7 growth fronts.

MgB_2 growing in them is not known. It is possible that only certain pairs of MgB_4 grains have special crystalligraphic relationships that allow for fast diffusion of Mg at their grain boundaries.

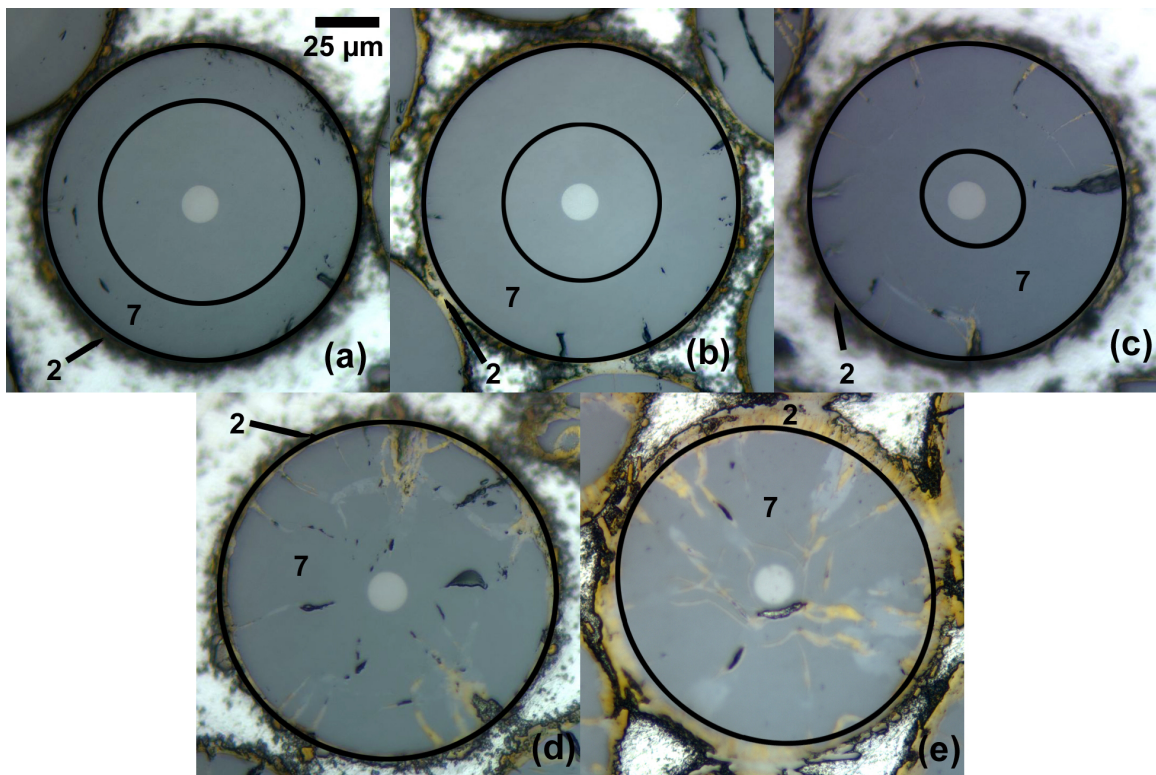


Figure 5.6. Optical micrographs of fibers reacted at 800 °C for (a) 1, (b) 2, (c) 3, (d) 4, and (e) 5 days showing only MgB_2 and MgB_7 growth fronts.

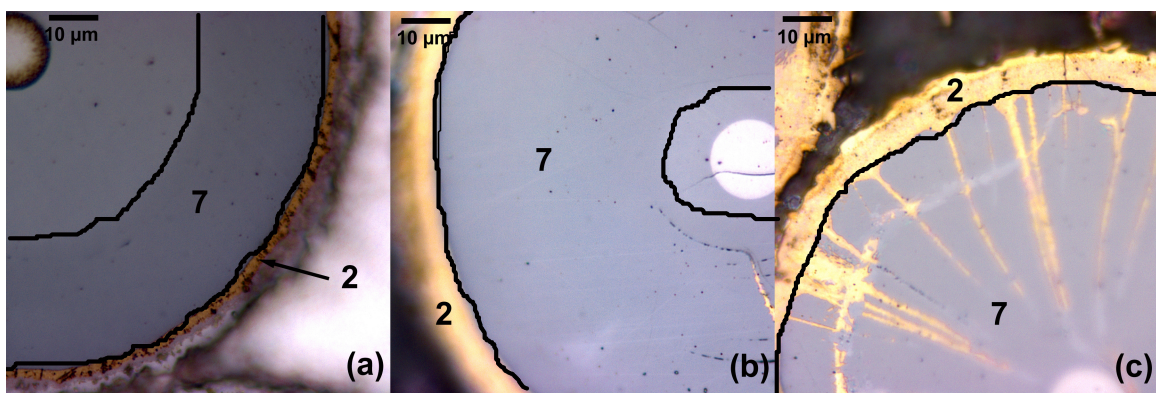


Figure 5.7. Optical micrographs of fibers reacted at 700 °C for (a) 21, (b) 54, and (c) 123 days showing only MgB_2 and MgB_7 growth fronts.

To determine the diffusion growth kinetics of MgB_2 and the other borides, thickness measurements of boride layers were made far from cracked regions where wedges of MgB_2

had grown between MgB₄ grains. Thicknesses were added cumulatively such that the MgB₇ front was a sum of the MgB₂, MgB₄, and MgB₇ thicknesses measured and the MgB₄ a sum of MgB₂ and MgB₄ thicknesses.

For all boride regions, the diffusion and reaction takes place radially in two dimensions so the thicknesses were scaled by the square root of the volume expansion coefficient (1.90 for MgB₂, 1.47 for MgB₄, and 1.18 for MgB₇) to adjust to a two-dimensional reaction and fit with a 5th degree polynomial equation from the model developed by Entchev et al [94] for the reaction of a cylinder with a volume expansion coefficient of 1. The fitting parameter was the diffusion coefficient D given the initial radius of 70 μm . Uncertainty on D was obtained by fitting to the error bars on the thickness values as shown in Figures 5.8 to 5.11.

Fits of cumulative thickness vs time for MgB₂ resulted in diffusion coefficients ranging from $2 \cdot 10^{-17} \text{m}^2/\text{s}$ at 700 °C to $6 \cdot 10^{-13} \text{m}^2/\text{s}$ at 1000 °C. Diffusion coefficients for MgB₄ growth fronts were $2 \cdot 10^{-17} \text{m}^2/\text{s}$ to $1 \cdot 10^{-11} \text{m}^2/\text{s}$ and diffusion coefficients for MgB₇ growth fronts were $1 \cdot 10^{-15} \text{m}^2/\text{s}$ to $1 \cdot 10^{-11} \text{m}^2/\text{s}$. The diffusion coefficient for MgB₂ at 800 °C was $6 \cdot 10^{-16} \text{m}^2/\text{s}$ which was close to the diffusion coefficient of $1 \cdot 10^{-16} \text{m}^2/\text{s}$ found for a thin film reacted by Kim et al [74] in Mg vapor at 800 °C, as shown in the Arrhenius plot in Figure 5.12 where the activation energy for MgB₂ growth was found to be 362 kJ/mol. Similarly, the activation energies for MgB₄ and MgB₇ were 477 kJ/mol and 319 kJ/mol respectively. The higher activation energy for MgB₄ was expected due to its large growth rate and thickness at 900 and 1000 °C compared to its lack of visibility at lower temperatures. The activation energy for growth of MgB₇ was similar to that of MgB₂. Considering the good fit of the Arrhenius plot for MgB₂, between 700 and 1000

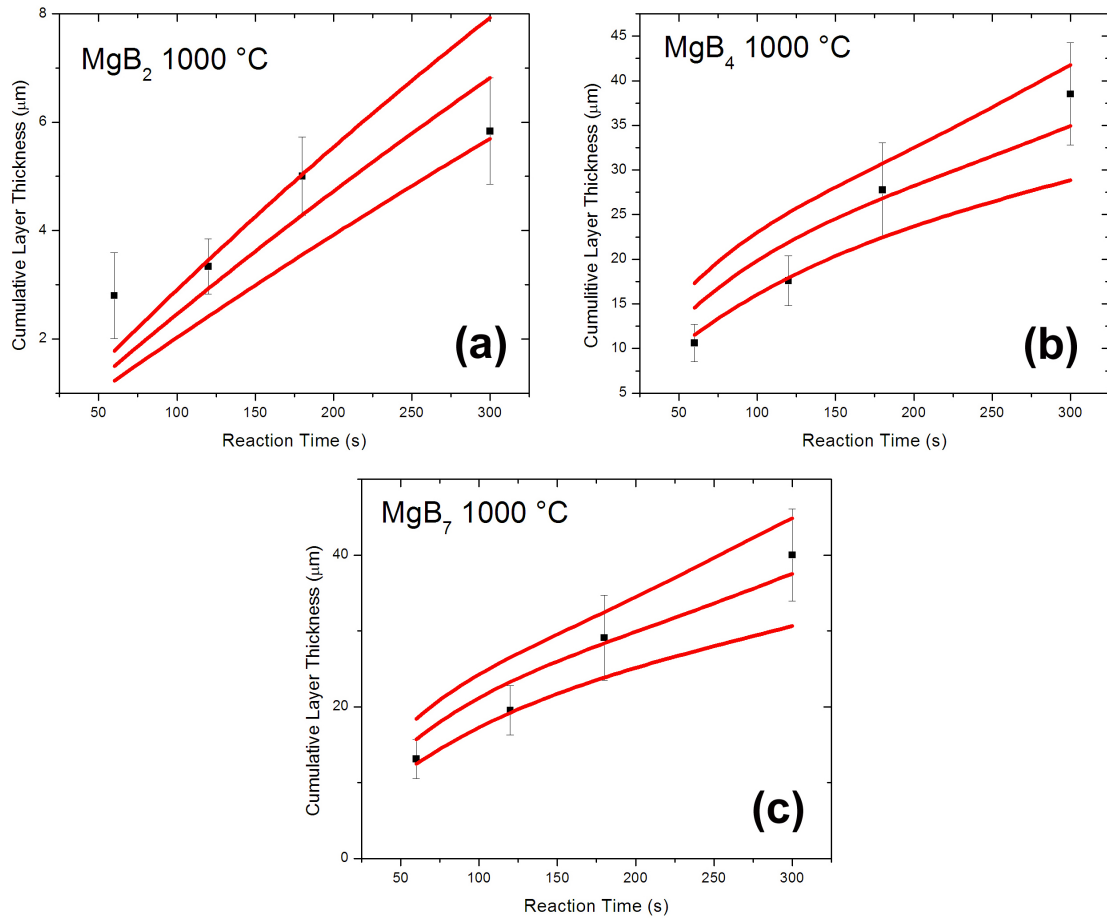


Figure 5.8. Fits of Entchev model [94] for reaction of a cylinder to ex situ thickness measurements of boride growth fronts on fibers reacted at 1000 °C.

°C (Figure 5.12) it was unlikely that MgB₂ growth was inhibited by the high activation energy for formation of MgB₄ in this temperature range.

Additionally, the Carter style derived equation for reaction of a cylinder was applied to the growth of MgB₂ with $z = 1.90$. Thickness measurements were first converted to

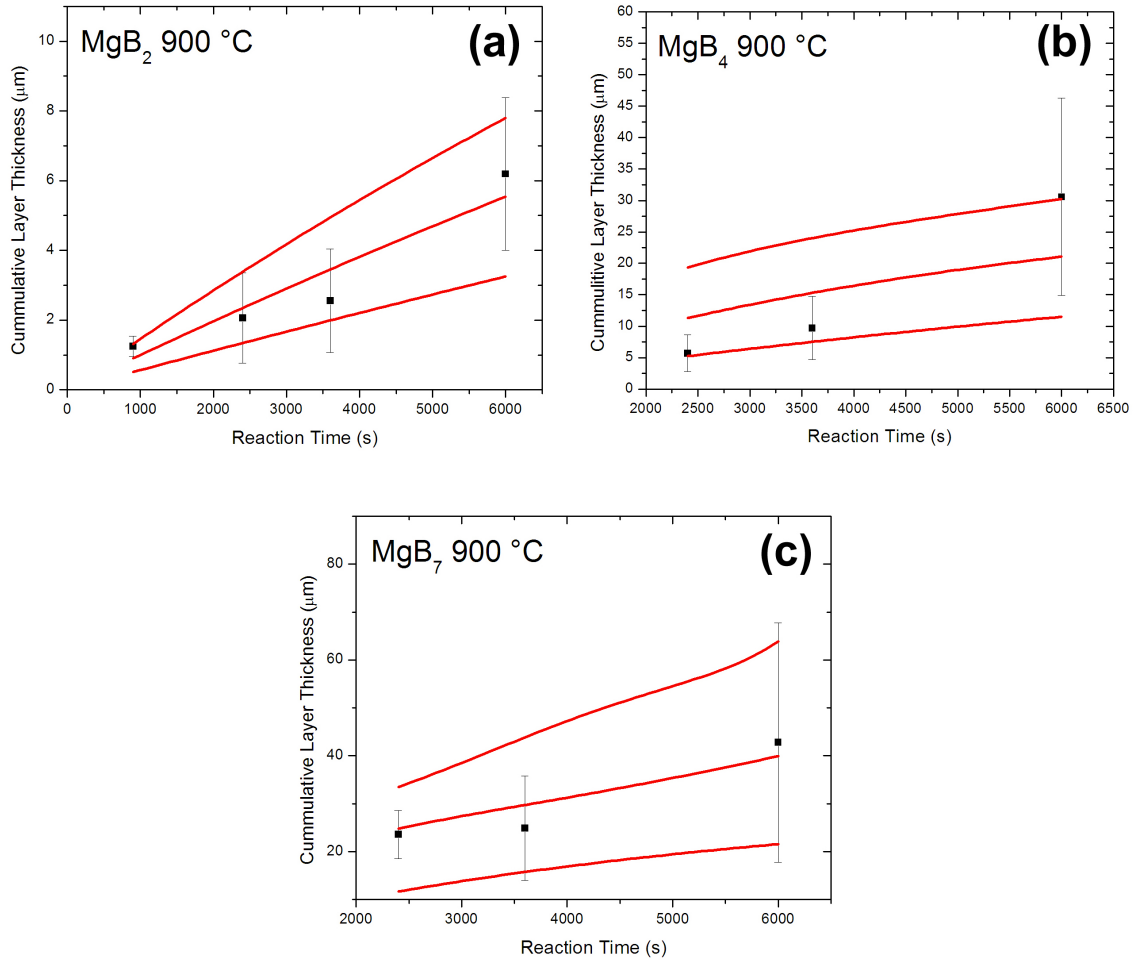


Figure 5.9. Fits of Entchev model [94] for reaction of a cylinder to ex situ thickness measurements of boride growth fronts on fibers reacted at 900°C.

degree of reaction through the equation

$$(5.2) \quad x = \frac{h \left(h + \left(\frac{-2h + 2\sqrt{h^2 - zh^2 + z^2 r_0^2}}{z} \right) \right)}{z r_0^2}$$

found assuming the degree of reaction, x , is the volume of boride formed divided by the volume of boride after completion of reaction where h is the boride layer thickness, z is the volume expansion coefficient, and r_0 is the initial fiber radius and is derived in

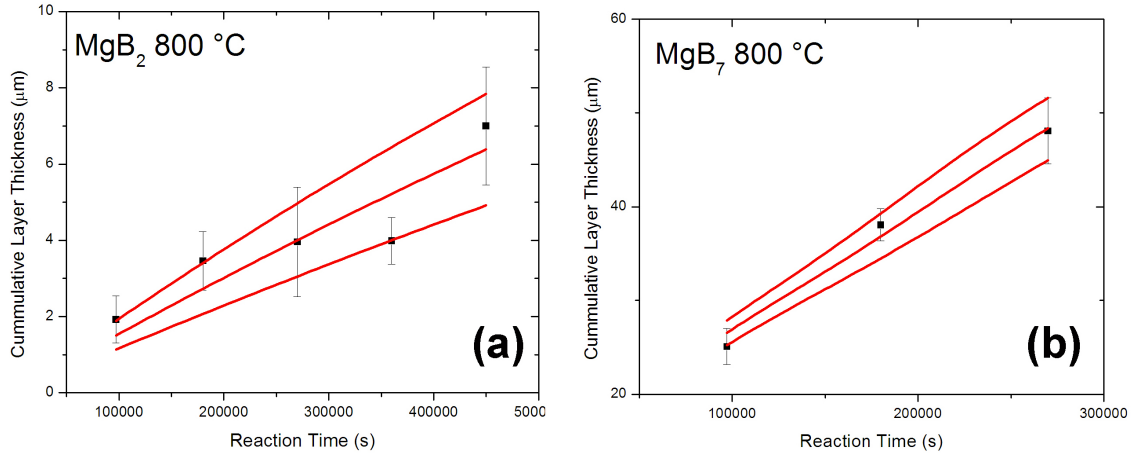


Figure 5.10. Fits of Entchev model [94] for reaction of a cylinder to ex situ thickness measurements of boride growth fronts on fibers reacted at 800 °C.

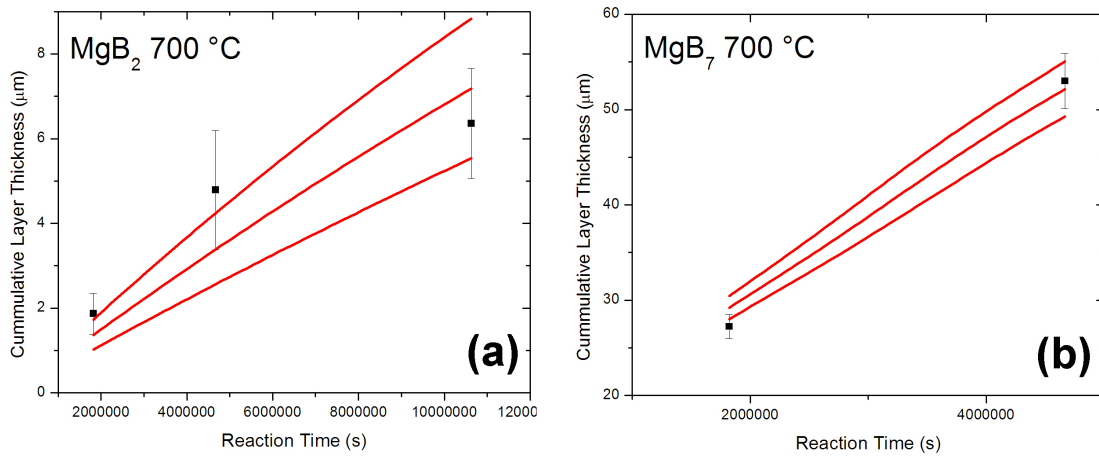


Figure 5.11. Fits of Entchev model [94] for reaction of a cylinder to ex situ thickness measurements of boride growth fronts on fibers reacted at 700 °C.

Appendix B.2. The reaction rate constant k was calculated from the slope of the $-kt$ vs reaction time plots from the Carter model (Figure 5.13). Rate constants for diffusional growth of MgB₂ from a B cylinder were $2 \cdot 10^{-18} m^2/s$ at 700 °C to $6 \cdot 10^{-14} m^2/s$ at

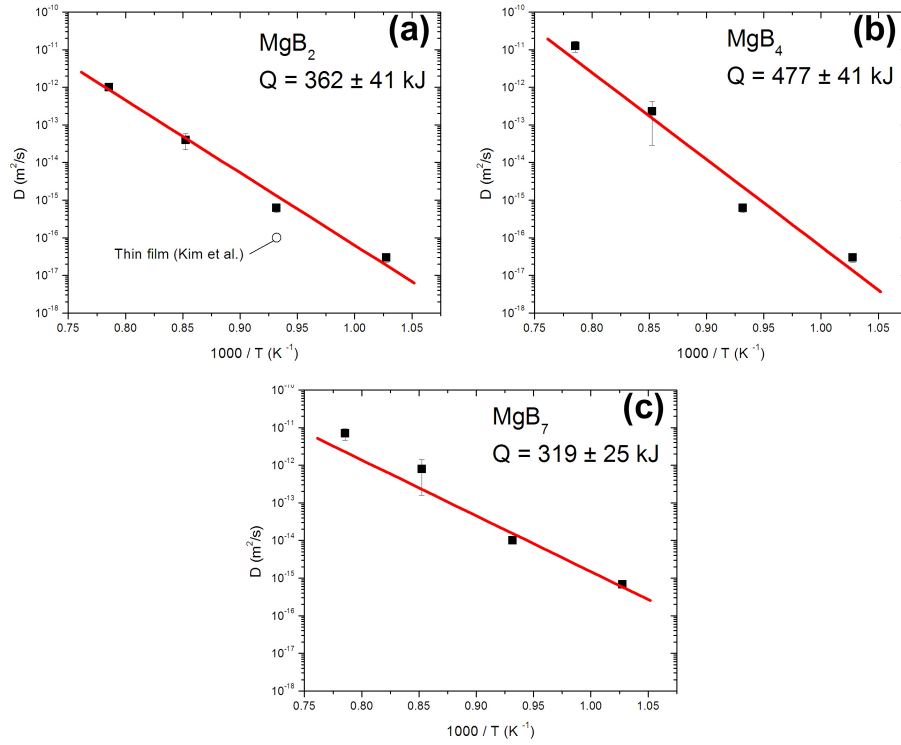


Figure 5.12. Arrhenius style plot of diffusion coefficients vs inverse temperature for the growth fronts of MgB_2 , MgB_4 , and MgB_7 showing activation energies of 362 kJ/mol, 477 kJ/mol, and 319 kJ/mol respectively.

1000 °C with a rate constant of $4 \cdot 10^{-15} \text{m}^2/\text{s}$ at 900 °C which was much higher than rate constant of $7 \cdot 10^{-17} \text{m}^2/\text{s}$ measured for powder reactions at 900 °C but less than that measured from in situ data where the cracking of the MgB_4 layer was enhancing the reaction rate. Similarly, the reaction rate constant of $6 \cdot 10^{-17} \text{m}^2/\text{s}$ at 800 °C was similar to the rate constant of $5 \cdot 10^{-17} \text{m}^2/\text{s}$ for the reaction of the thin film by Kim et al [74] when fit to a Carter style derivation of a reaction of a planar interface (Figure 2.6) as well as the reaction rate constants between $4 \cdot 10^{-18}$ and $3 \cdot 10^{-17} \text{m}^2/\text{s}$ for MgB_2 reacted from powders as discussed in Chapter 2. An Arrhenius plot of the rate constants vs inverse temperature shows an activation energy of 360 kJ/mol for MgB_2 growth (Figure 5.14),

which was the same as the activation energy found from the Entchev fit (362 kJ/mol). The activation energy was much larger than calculated for powders (70 - 146 kJ/mol) which were also based on a diffusion model. Fibers were dense perfect cylinders immersed in liquid Mg while powders were irregular agglomerates of small nanosized spheres that were likely not completely infiltrated with liquid Mg. This difference may explain the discrepancy in activation energies. Additionally, the fibers were reacted up to 1000 °C while powders were mostly reacted at 800 °C and below, with only one sample reacted at 900 °C. Only four data points were used to calculate activation energy in both the powder and fiber cases, if additional experiments showed a steeper slope at high temperature, due to additional mechanisms such as cracking in the MgB₄ region, and a shallower slope at low temperature, the difference in activation energies between powders and fibers would be explained.

Diffusion coefficients and reaction rate constants calculated above were determined from thickness measurements away from cracks in the MgB₄ layer and were close to diffusion coefficients and rate constants for powder and thin film reactions as fit by diffusion models suggesting that the measurements on fibers were also diffusion controlled. The diffusion coefficients found from MgB₂ thickness measurements predict reaction times from 65 h to 3 h from 900 - 1000 °C for 70 μm radius B fibers in liquid Mg as shown in Figure 5.15. Additionally, rate constants predict a reaction time of 7 hours at 1000 °C and 118 hours at 900 °C. Both were much slower than shown for in situ measurements (Figure 5.1) between 885 and 1025 °C confirming the likelihood that further fiber reaction was controlled by another mechanism such as cracking in addition to diffusion.

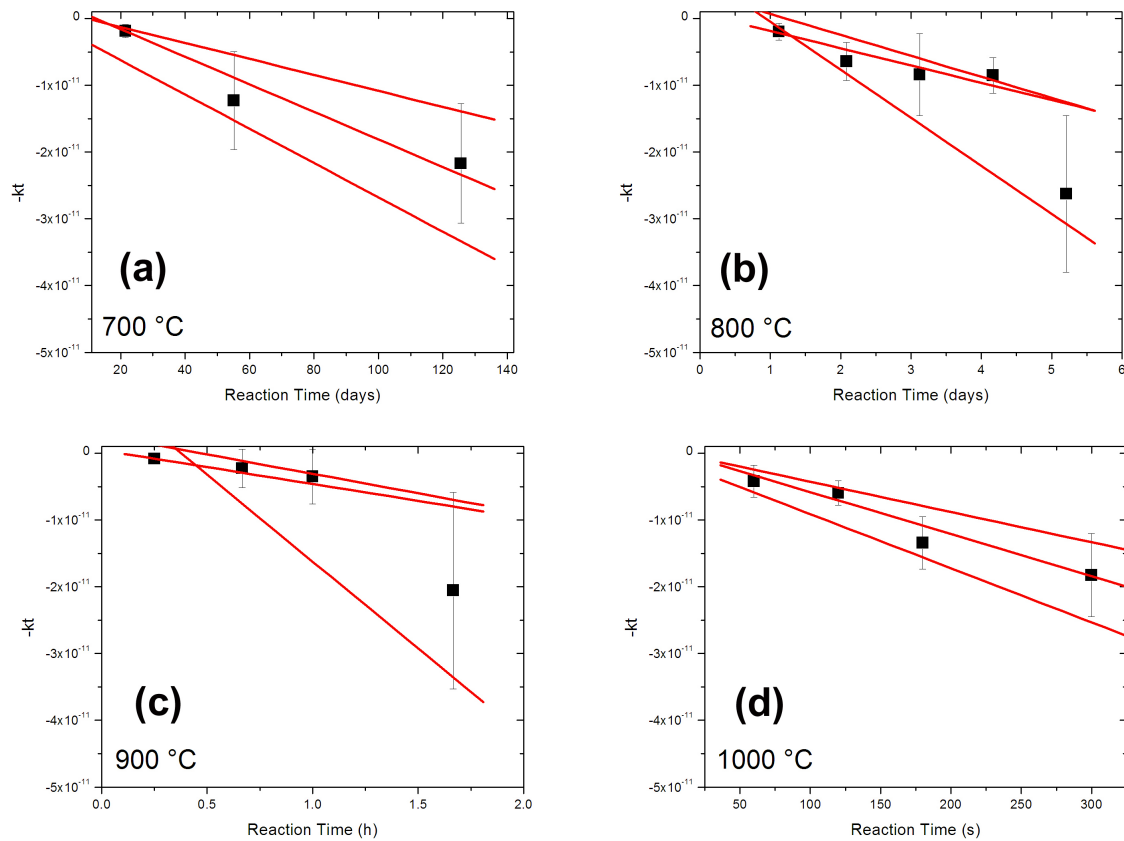


Figure 5.13. Plots of Carter cylinder derivation (Equation (5.1)) for $-kt$ vs time for ex situ thickness measurements on interrupted reactions of B fibers at 700 - 1000 °C.

5.2.3. Reaction Modeling

Fiber reactions were modeled based on the microstructural observations and diffusion coefficients calculated above. The model was divided into two parts shown in Figure 5.16, the diffusion-only shell reaction determined by the diffusion coefficient of MgB_2 and the crack or grain boundary reaction modeled by a triangular shaped half-wedge. The longer height of the wedge was modeled by the growth of MgB_4 since it was observed that MgB_2 spanned nearly the entire length of the MgB_4 region and the short base of the triangular

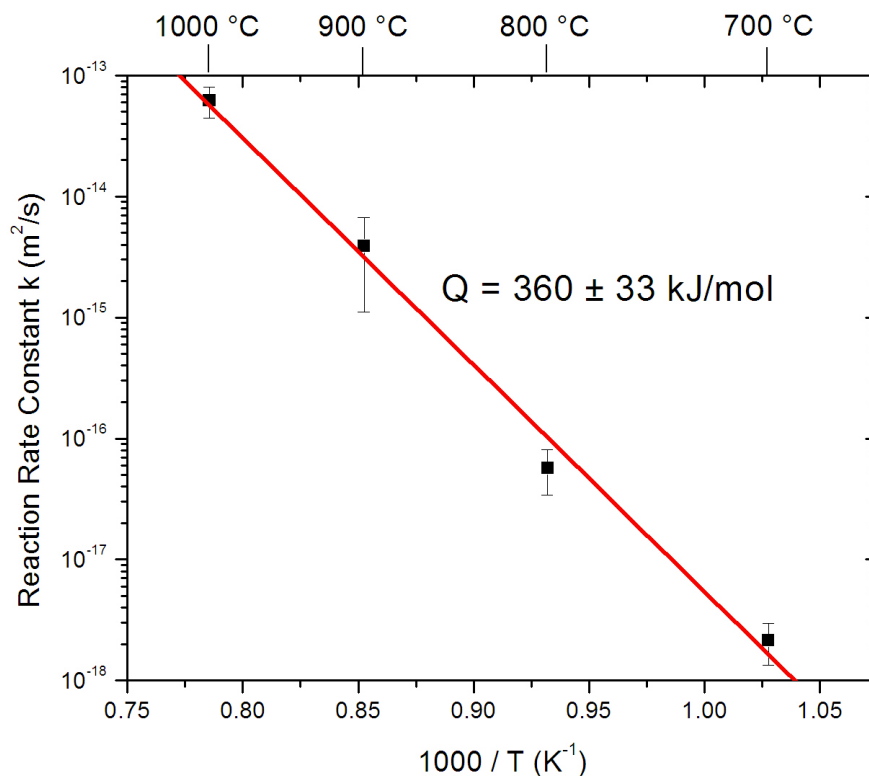


Figure 5.14. Arrhenius plot of Carter cylinder derivation fit of reaction rate constant k vs inverse temperature for ex situ MgB_2 thickness measurements on interrupted reactions of B fibers at 700 - 1000 $^{\circ}\text{C}$ showing activation energy of 360 kJ/mol.

wedge determined by the growth of MgB_2 . The model summed the contributions of the shell on the outside of the fiber with the wedges observed within the MgB_4 region. The wedge grows with the MgB_4 diffusion coefficient with lateral growth of the wedge growing with the MgB_2 diffusion coefficient. The shell grows in from the outside of the fiber with the MgB_2 diffusion coefficient. The number of wedges was determined by an input for the number of cracks, N . With the assumption of triangular wedges and diffusion determined by coefficients calculated above, the fiber reaction was modeled by the geometry shown

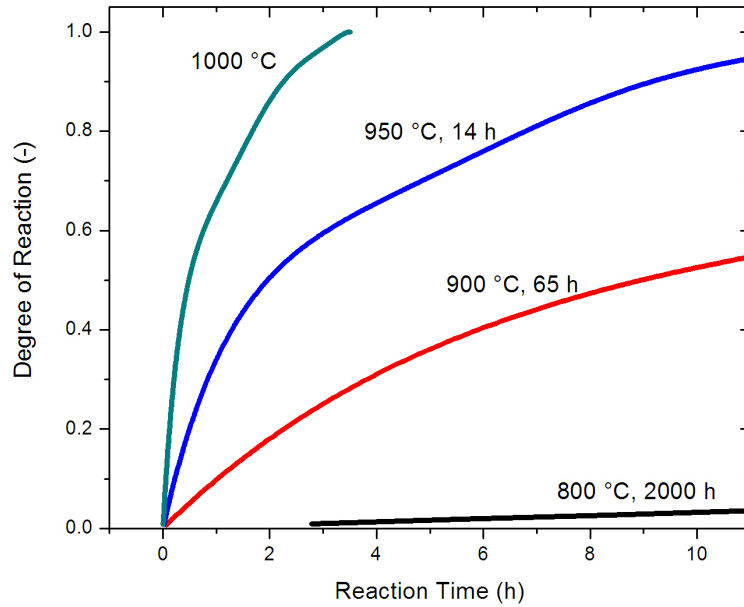


Figure 5.15. Predicted reaction curves using measured diffusion coefficients and Entchev cylinder reaction model [94] showing reaction times much longer than observed experimentally.

in Figure 5.17. The reacted shell area, A_s was calculated directly from the diffusion of MgB_2 into the cylinder and is shown as,

$$(5.3) \quad A_s = \frac{1}{2N} (\pi r_0^2 - \pi (r_0 - x)^2)$$

The reacted wedge area, A_w was calculated from the diffusion of MgB_4 into the cylinder and the diffusion of MgB_2 perpendicularly away from the crack as,

$$(5.4) \quad A_w = \frac{1}{2}fb + \frac{1}{4}r_0^2 \left(2 \sin^{-1} \left(\frac{b}{r_0} \right) - \sin \left(2 \sin^{-1} \left(\frac{b}{r_0} \right) \right) \right)$$

The wedges grow beyond the limits of the section of fiber modeled with the overlap, A_o of nearby wedges calculated for $b > a$ as,

$$(5.5) \quad A_o = (s(s-r)(s-p)(s-q))^{\frac{1}{2}} + \frac{r_0^2}{2} \left(2 \sin^{-1} \left(\frac{r}{2r_0} \right) - \sin \left(2 \sin^{-1} \left(\frac{r}{2r_0} \right) \right) \right)$$

Additionally, for calculations, the area of the wedge, A_{wf} that was in front of the reacted shell front is calculated as,

$$(5.6) \quad A_{wf} = \frac{1}{2}wz + \frac{1}{4}u^2 \left(2 \sin^{-1} \left(\frac{w}{u} \right) - \sin \left(2 \sin^{-1} \left(\frac{w}{u} \right) \right) \right)$$

The shell contribution to the total reaction, A_{stot} was then calculated as,

$$(5.7) \quad A_{stot} = A_s - A_w + A_o + A_{wf} \text{ for } \beta < \alpha$$

The wedge contribution to the total reaction, A_{wtot} was calculated as,

$$(5.8) \quad A_{wtot} = A_w - A_o$$

The total reacted area, A_{tot} was then found by addition of the wedge and shell contributions

$$(5.9) \quad A_{tot} = A_{wtot} + A_{stot}$$

with degree of reaction calculated by dividing the reacted area, A_{tot} by the area of the section of fiber modeled, A_{sect} which can be calculated by dividing the area of the fiber

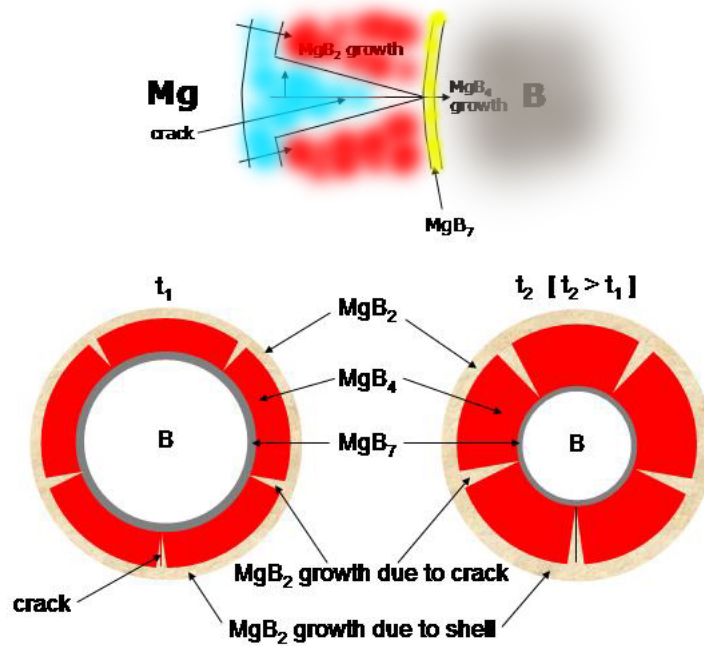


Figure 5.16. Schematics describing reaction model design where the amount of MgB_2 reacted depends on the growth front of MgB_4 where MgB_2 wedges will grow into cracks in the MgB_4 region as well as the MgB_2 growth front from diffusion through the product layer on the outside of the fiber.

by two times the number of cracks as shown by,

$$(5.10) \quad A_{sect} = \frac{1}{2} \alpha r_0^2$$

$$(5.11) \quad DegreeOfReaction = \frac{A_{tot}}{A_{sect}}$$

The degree of reaction calculation was solved exactly using Maple software and outputs from 0 to 1 for full reaction. The calculation levels off at 1 briefly and then continues to infinity but all information after 1 was neglected.

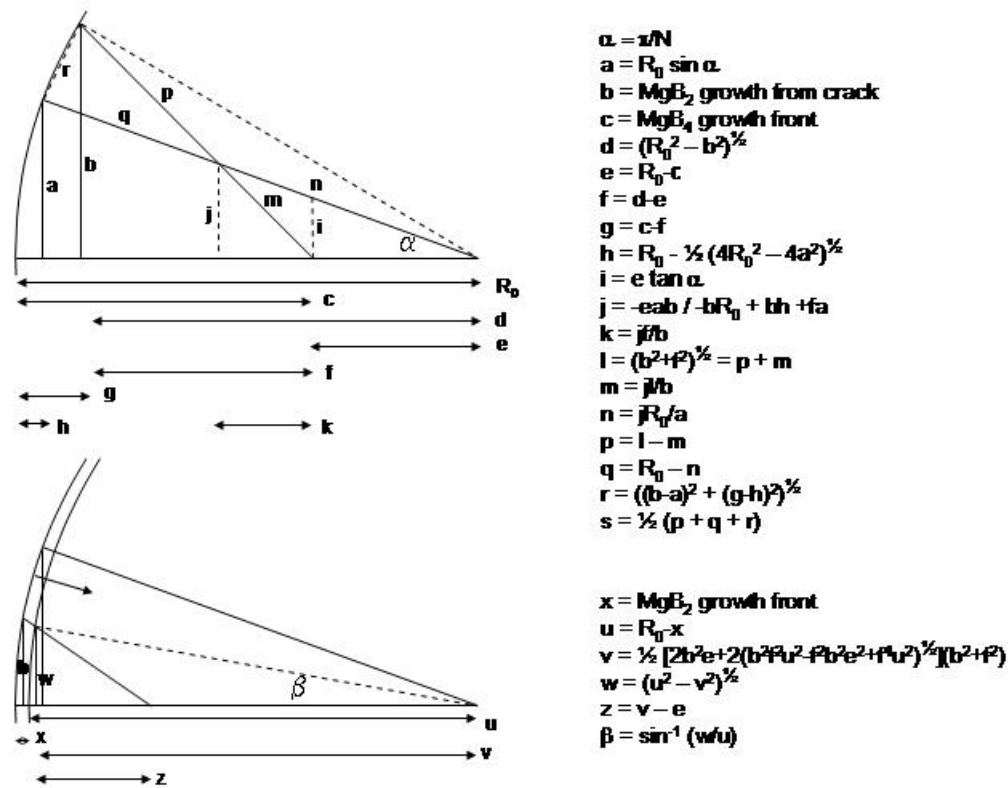


Figure 5.17. Drawings showing geometric parameters used for the calculation of degree of reaction vs time curves given the diffusion coefficients for the growth fronts of MgB_2 and MgB_4 and the number of cracks, N .

Features of model output with diffusion at 900 °C and 7 or 30 cracks per fiber are shown in Figure 5.18(a-b). With 30 cracks, the reaction proceeds quickly with the wedges controlling the reaction rate. Reaction due to the shell on the outside of the cylinder only contributes early in the reaction. With 7 cracks, the reaction proceeds quickly until an inflection point where the wedge reaches the center of the fiber and a slower rate is shown completing the reaction which is a combination of lateral growth from the wedge and the continued shell reaction front. This type of reaction is illustrated in the micrograph

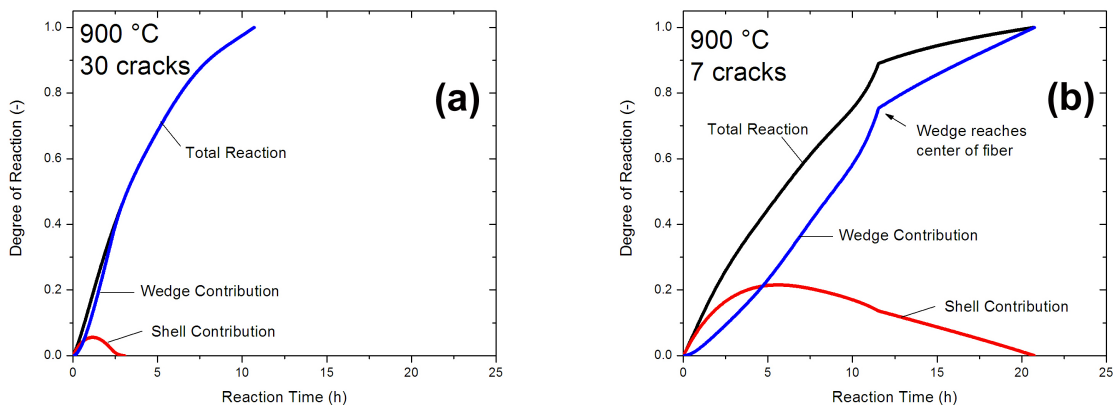


Figure 5.18. Plots of model output degree of reaction vs time showing contributions of shell and wedge reactions where (a) shows wedge reaction dominating the total reaction with 30 cracks per fiber and (b) showing the more significant contribution of the shell reaction as well as a kink in the wedge reaction curve corresponding to when the wedge reaches the center of the fiber for 7 cracks per fiber.

shown in Figure 5.19 with wedges of MgB_2 reaching the core of the fiber even though the fiber was only 50% reacted. The reaction rate after the inflection point was slow since in the absence of the cracking mechanism, only MgB_2 diffusion across large product layers is an active mechanism. More cracks is beneficial to reduce the width of the product layer that diffusion must take place across as shown by the reduction of reaction time with increasing cracks in Figure 5.20(a-b). There is an exponential relationship between the reaction time and number of cracks as shown in Fig 5.20(c) and it appears that the reaction time does not decrease significantly between 10-15 cracks.

Using the diffusion coefficients calculated from the Entchev fit discussed above (Figures 5.8 - 5.11), another strong effect is shown on reaction time as visible in Figure 5.21(a-b). Within the uncertainty of the diffusion coefficients at 900 °C, reaction time can change from 25 h to 6 h with 30 cracks and from 62 h to 24 h with 5 cracks. The effects of MgB_2

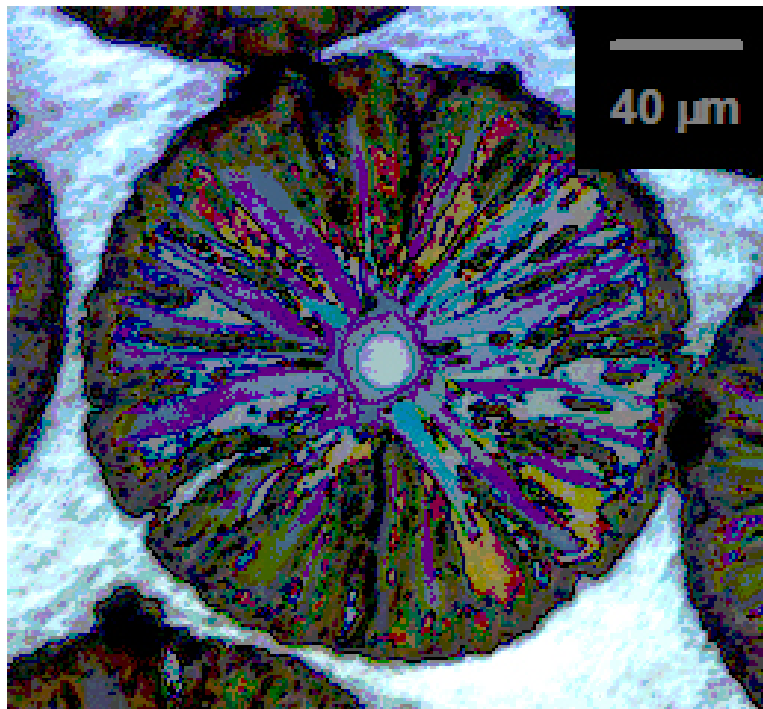


Figure 5.19. Optical micrograph showing wedges reaching center of fiber given 50% reaction at 1000 °C for 20 min.

diffusion and MgB_4 diffusion can be isolated and compared as shown in Figure 5.22(a-d). MgB_2 diffusion controls reaction time when there are fewer cracks and MgB_4 diffusion controls reaction time when there are many cracks. This was shown by holding the MgB_4 diffusion coefficient constant with 30 cracks, and adjusting the MgB_2 diffusion coefficient within the experimental uncertainty. Total reaction time was calculated to change by 1 h whereas by holding the MgB_2 diffusion coefficient constant and adjusting the MgB_4 diffusion coefficient within the uncertainty, reaction time changed by 17 h Figure 5.22(a-b). The opposite was true with 5 cracks, where holding the MgB_4 diffusion coefficient constant and adjusting the MgB_2 diffusion coefficient changed reaction time by 38 h but

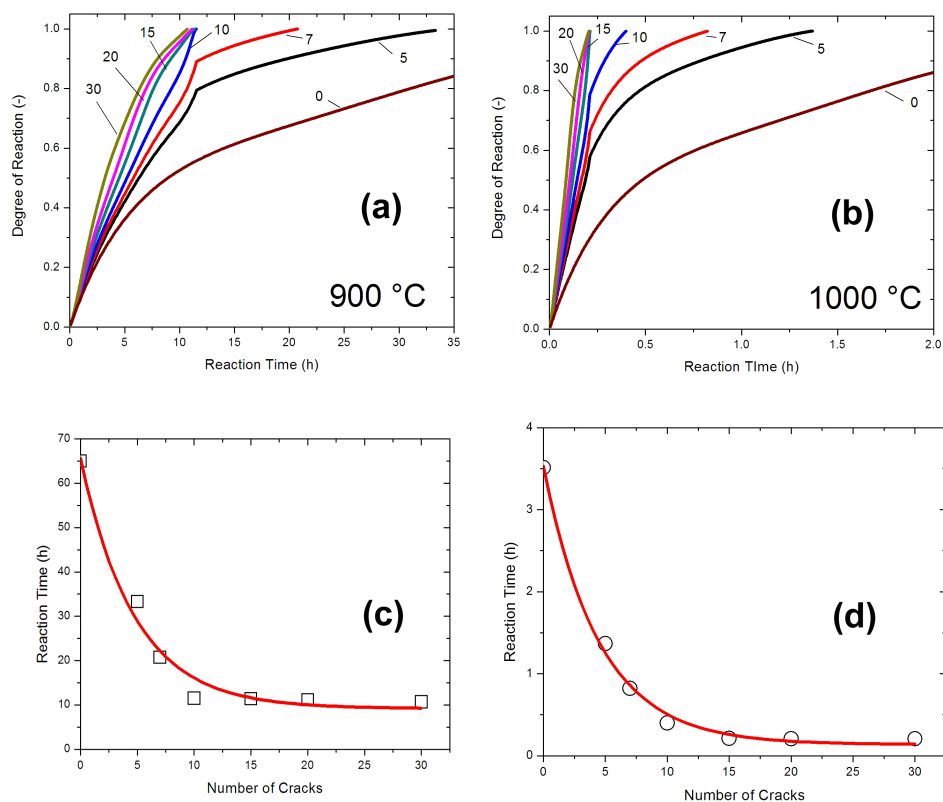


Figure 5.20. Plots of model output showing the effect of cracks on reaction time. (a) shows the effect of cracks with diffusion coefficients at 900 °C on degree of reaction, (b) shows the effect of cracks with diffusion coefficients at 1000 °C on degree of reaction, and (c) and (d) showing exponential relationship between the reaction time and number of cracks.

holding the MgB_2 diffusion coefficient constant and adjusting the MgB_4 diffusion coefficient did not change reaction time Figure 5.22(c-d). As expected, the initial reaction goes with MgB_4 diffusion as MgB_4 diffusion determines the length of the wedges but when the wedges reach the center of the fiber, which is only the case with less than 10-15 cracks, the reaction was then controlled by MgB_2 diffusion. The MgB_4 diffusion coefficient determined the initial reaction rate with the MgB_2 diffusion controlling the final reaction rate

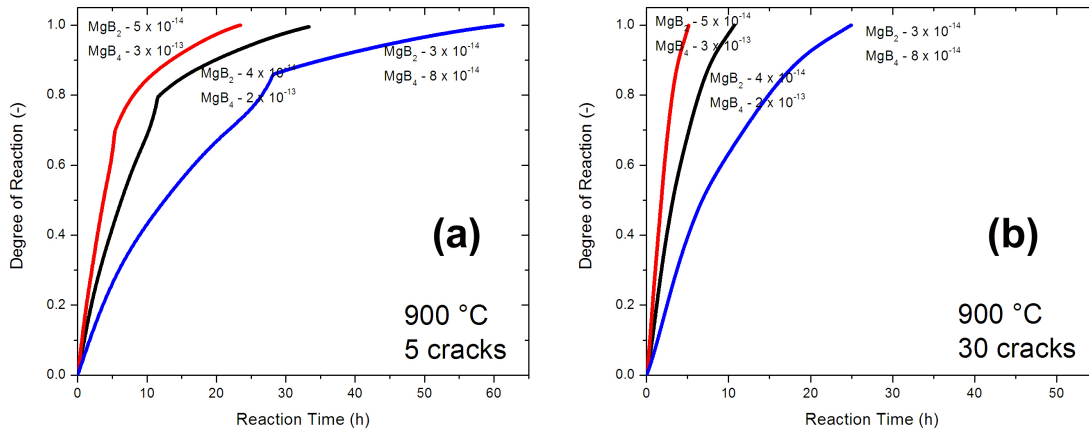


Figure 5.21. Plots of model output degree of reaction vs time showing effect of diffusion coefficient within uncertainty determined from thickness measurements on the reaction rate of B fibers in liquid Mg.

after wedges reach the fiber center. In the case of a large number of cracks, the wedges never reach the core so that was why MgB_4 controlled the total reaction time.

Using the knowledge of the effects of MgB_2 diffusion coefficient, MgB_4 diffusion coefficient, and number of cracks, experimental data was fitted with the model. The best fit of in situ data for the reaction of $140 \mu\text{m}$ fibers at $900 \text{ }^\circ\text{C}$ was obtained with an MgB_2 diffusion coefficient of $10^{-13} \text{m}^2/\text{s}$, an MgB_4 diffusion coefficient of $10^{-12} \text{m}^2/\text{s}$, and 8 cracks as shown in Figure 5.23(a). The data from reacting at $1000 \text{ }^\circ\text{C}$ was best fit by an MgB_2 diffusion coefficient of $15 \cdot 10^{-13} \text{m}^2/\text{s}$, an MgB_4 diffusion coefficient of $16 \cdot 10^{-12} \text{m}^2/\text{s}$, and 4 cracks as shown in Figure 5.23(b). Fits were improved by offset to account for incubation time. In both cases, best fits were obtained with diffusion coefficients greater than experimentally measured by ex situ studies of partially reacted fibers. Additionally, best fits used only 4-8 cracks where ex situ studies showed 20-30 cracks in fibers at 900 and $1000 \text{ }^\circ\text{C}$. These unexpected results work together to explain the model data. At the

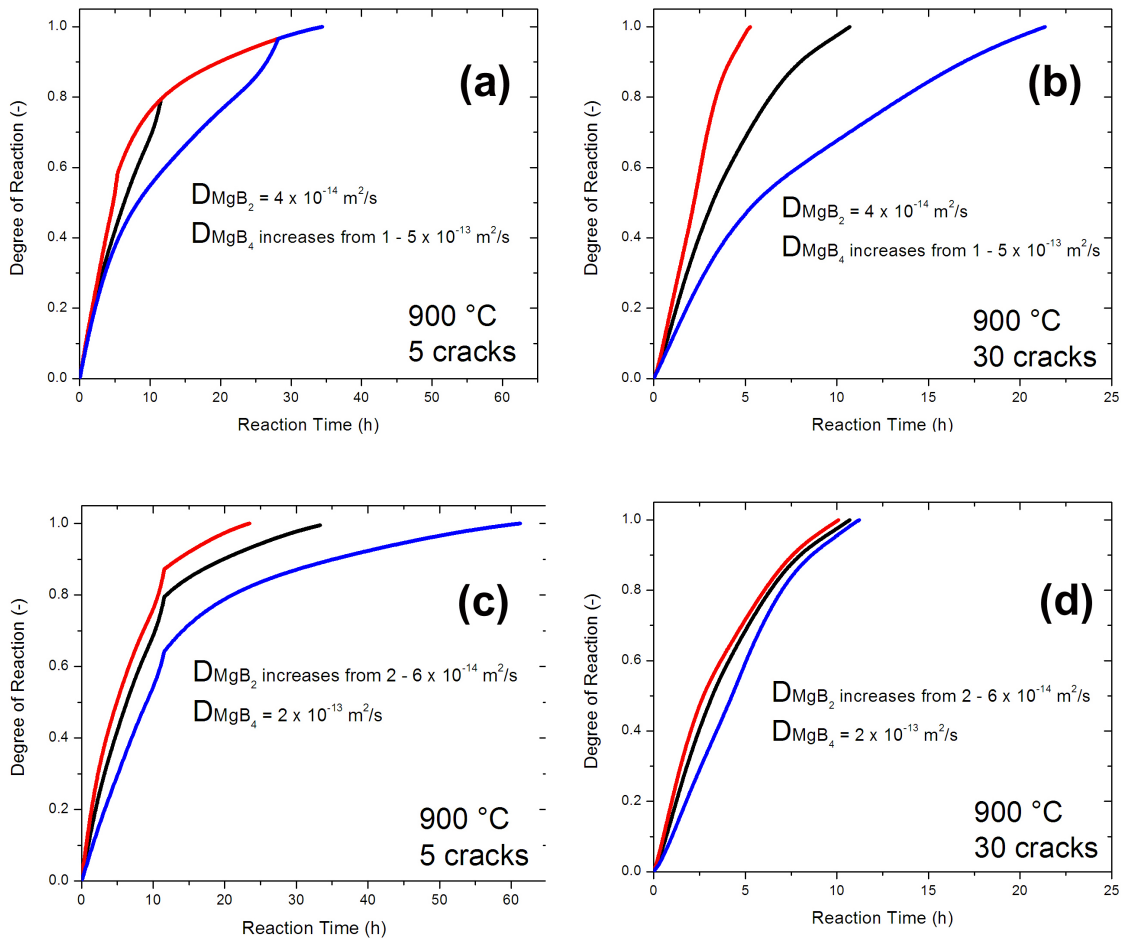


Figure 5.22. Plots of model output showing the effect of individual diffusion coefficients of MgB_2 and MgB_4 showing that the diffusion coefficient of MgB_4 controls the initial reaction rate and the MgB_2 controls the final reaction rate after wedges reach the center of fibers.

end of a reaction, only 2-10 slivers of MgB_4 were observed (Figure 5.24). These are the regions that react slowly after the wedges reach the core. The model assumes a uniform distribution of cracks where finishing the reaction with 5 slivers would require 5 cracks at the beginning of the reaction. A random distribution of cracks would have some small diffusion distances that would react quickly as well as some large wedges with longer diffusion distances between cracks which would react more slowly. The cracks merge as

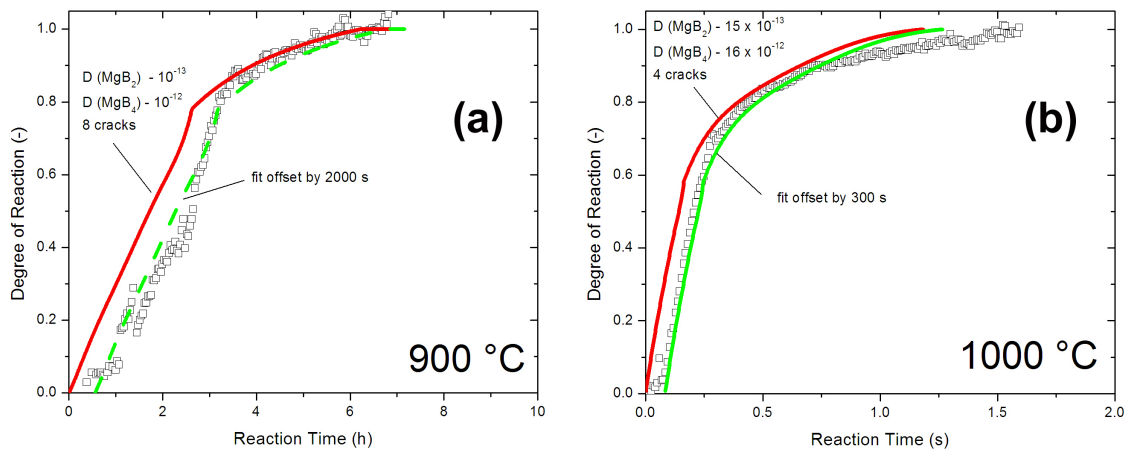


Figure 5.23. Model fits of diffusion coefficients and number of cracks to experimental in situ data from Figure 5.1.

shown in Figure 5.25 creating large MgB_4 regions that must be reacted without further crack assistance. The effect was simulated by adjusting the model so 30 cracks reacted 50% of the fiber area leaving 3 non-cracked wedges where only MgB_2 diffusion finishes the reaction. Here the 1000 °C in situ reaction data was fit by an MgB_2 diffusion coefficient of $9 \cdot 10^{-13} \text{m}^2/\text{s}$ and an MgB_4 diffusion coefficient of $12 \cdot 10^{-12} \text{m}^2/\text{s}$ (Figure 5.26). Both values were well within the uncertainties calculated by ex situ thickness measurements.

While data were represented with the adjustment to the model, two additional fitting parameters (the fraction reacted by cracks and the number of non-cracked wedges) add degrees of freedom that aid in fitting the data. Both reacting 50% by cracks and having only 3 wedges were reasonable as observed by experiment. Reacting only 50% by cracks appears to be a low number but as a microstructure, when all 50% is reacted, the volume expansion would make it appear as if nearly 75% was reacted, in addition the wedges would react likewise and would result in 3 thin slivers seen in the microstructure near the

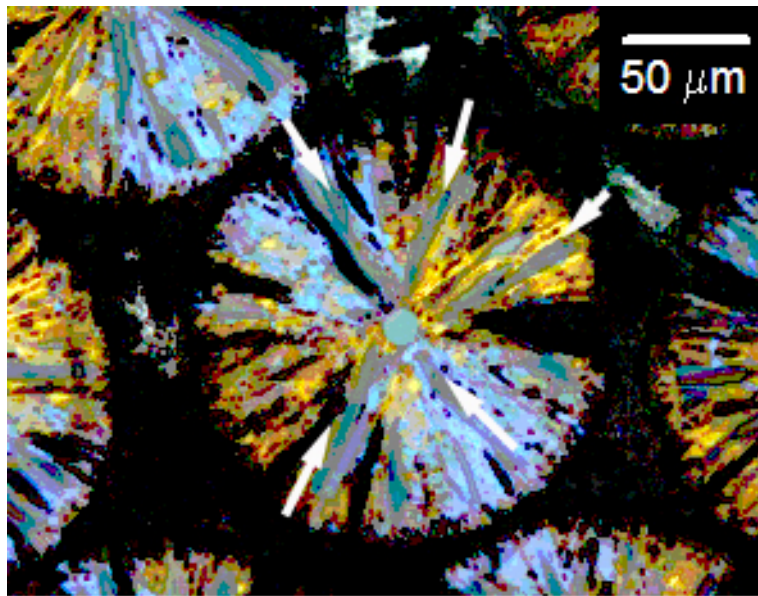


Figure 5.24. Optical micrograph showing unreacted slivers of MgB_4 near end of reaction which does not correlate to the 20-30 cracks seen early in reactions.

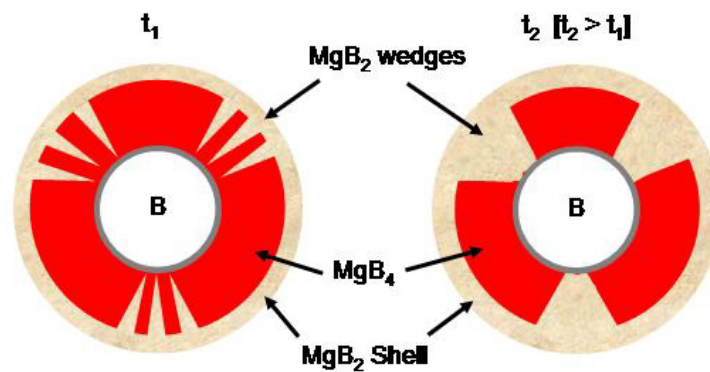


Figure 5.25. Illustration of 9 non uniformly distributed cracks merging into 3 wedge regions showing short distances between cracks reacting quickly to form the merged wedge with large distances between cracks remaining.

end of the reaction. As previously discussed, 2-10 slivers were often seen at the end of reactions.

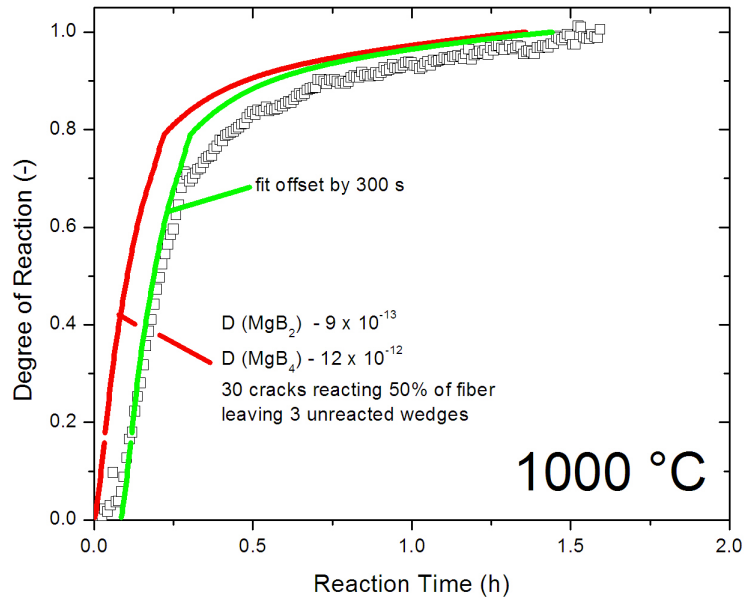


Figure 5.26. Fit of adjusted model where 50% of fiber reacted by cracks to experimental in situ data to simulate the effect of cracks merging during the reaction of fibers.

5.3. Conclusions

The reaction of liquid Mg and 140 μm B fibers to form MgB_2 fibers was studied both in situ and ex situ to determine reaction kinetic parameters and reaction mechanisms. Ex situ experiments measured kinetic parameters for the diffusion mechanism and found diffusion coefficients for MgB_2 between $2 \cdot 10^{-17} \text{m}^2/\text{s}$ at 700 $^\circ\text{C}$ and $6 \cdot 10^{-13} \text{m}^2/\text{s}$ at 1000 $^\circ\text{C}$ by fitting to a cylinder reaction model. Diffusion coefficients were in agreement with previous results for powders as well as published data for the reaction of a boron thin film. The activation energy for reaction of MgB_2 by diffusion was 362 kJ/mol. In situ experiments were not well fit with diffusion models due to the presence of an additional

cracking mechanism in the full reaction of fibers. The cracking mechanism was modeled numerically according to microstructural observations with in situ experiment reaction curves fitted based on the number of cracks and diffusion coefficients.

CHAPTER 6

Processing Variable Effects on the Reaction Kinetics of MgB₂ Fibers

In this Chapter, processing variables such as fiber diameter, fiber doping, fiber surface treatment, Mg phase, and thermal treatments are examined to determine their effects on the reaction kinetics of converting B fibers into MgB₂ fibers. Chapter 5 examined only 140 μm diameter fibers in liquid Mg to determine reaction kinetic parameters and model the reaction. This chapter examines the extent to which reaction modeling applies to other processing procedures and how reaction mechanisms can be used to enhance reaction rates.

6.1. Experimental Procedures

Reactions of liquid Mg and B fibers were studied in situ and ex situ using synchrotron radiation and optical microscopy as described in previous chapters. In this chapter, several processing variables were varied to investigate their effects on reaction rates and MgB₂ microstructure. Reactions of 100 μm diameter B fibers were studied in liquid Mg to compare to the larger 140 μm diameter fibers discussed in Chapter 5. Reaction of these 100 μm B fibers was also studied with Mg vapor to compare to reactions with liquid Mg and determine what flux of Mg is sufficient to react B fibers to MgB₂. Fibers of 140 μm diameter with a thin 1-2 μm shell of nitride created by first oxidizing the fiber then reacting with ammonia [117] were studied and compared to the non-nitrided 140 μm B

fibers of Chapter 5. Reactions of C-doped B fibers have been reported to react much slower than reaction of un-doped B fibers with reactions completed in 72 hours at 1000 °C or 48 hours at 1200 °C [56]. Fibers with 0.4 at% C created by co-deposition of C from CH₄ gas with B from BCl₃ gas during the CVD process [54] were studied ex situ after reaction at 1000 °C for 5 min and 2.5 hrs in liquid Mg to investigate the effect C upon reaction rate.

Due to the overall slow reactions of fibers compared to powders, the possibility of increasing reaction rate through enhanced cracking of the MgB₄ layer using thermal expansion mismatch was investigated by reacting fibers under thermal cycling conditions and compared to isothermal reactions at the maximum cycle temperature. Reaction temperature was cycled between 668-900 °C ($\Delta T = 232$ °C) and 737-900 °C ($\Delta T = 163$ °C). The cycles were meant to be square with an example shown in Figure 6.1 with as fast of heating rate as possible to 900 °C and as fast of cooling as possible to the lower bound cycle temperature without overshooting. Besides the change in the ΔT of the cycle, the cycle time was also studied by comparing reactions with 10 cycles to reactions with 30 cycles. Finally, to eliminate the geometry effect, 100 μm fibers were ground into 25 - 45 μm powders and reacted at 900 °C and compared to powder and fiber reactions at 900 °C.

6.2. Results and Discussion

6.2.1. Effect of Fiber Diameter

100 μm B fibers exposed to liquid Mg between 900 and 1000 °C reacted in 1-5 hrs as shown in Figure 6.2. Reaction times were similar to 140 μm fibers despite the fact that 100 μm

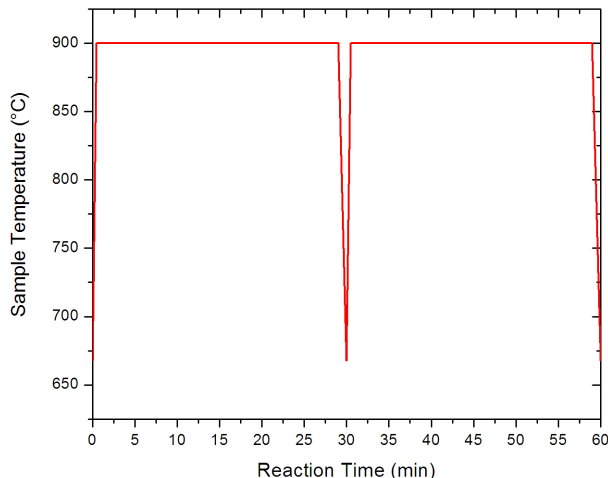


Figure 6.1. Sample temperature vs time plot showing two cycles for reactions under thermal cycling conditions.

fibers have about half of the volume of the larger $140\ \mu\text{m}$ fibers. The Entchev diffusion model would predict a $100\ \mu\text{m}$ fiber would react to MgB_2 in 51% of the time to react a $140\ \mu\text{m}$ fiber due to the smaller diameter fiber being half the total volume. The cracking model of Chapter 5 also predicted reaction of the smaller fiber in 51% of time of the larger $140\ \mu\text{m}$ fiber, given 4 cracks and the diffusion coefficients required for the fit shown in Figure 5.23. Cracking model fits to $100\ \mu\text{m}$ fiber data at $900\ \text{°C}$ were best achieved with 9 cracks, an MgB_2 diffusion coefficient of $6 \cdot 10^{-14}\text{m}^2/\text{s}$ and an MgB_4 diffusion coefficient of $5 \cdot 10^{-13}\text{m}^2/\text{s}$. These values were on the high end of the uncertainty range found for diffusion coefficients of MgB_2 in Chapter 5. Similarly, $1000\ \text{°C}$ data for reaction of $100\ \mu\text{m}$ fibers was best fit by 6 cracks, an MgB_2 diffusion coefficient of $1 \cdot 10^{-12}\text{m}^2/\text{s}$, and an MgB_4 diffusion coefficient of $12 \cdot 10^{-12}\text{m}^2/\text{s}$ as shown in Figure 6.2 which were the average values calculated from ex situ measurements in Chapter 5. The $950\ \text{°C}$ reaction curve of

100 μm fibers was best fit by 12 cracks, an MgB_2 diffusion coefficient of $8 \cdot 10^{-14} \text{m}^2/\text{s}$, and an MgB_4 diffusion coefficient of $8 \cdot 10^{-13} \text{m}^2/\text{s}$ as shown in Figure 6.2 which were near the values predicted by the Arrhenius plot for diffusion coefficients (Figure 5.12) in Chapter 5. The large number of cracks is expected for the best fit due to very linear nature of the reaction curve.

Microstructurally, fibers reacted at 1000 °C for 3 minutes (Figure 6.3) were also similar to 140 μm fibers (Figure 5.4). Growth thicknesses of MgB_2 and MgB_4 reaction fronts (4 and 22 μm , respectively) were similar to reactions of 140 μm fibers with MgB_2 growing into cracks as shown in Figure 5.4(c). Stresses due to the volume expansion of forming MgB_2 may be less for a smaller fiber reducing the amount of cracking in the MgB_4 layer but microstructures were comparable. Overall, reactions of smaller diameter fibers, although predicted by pure diffusion to react in half the time due to half the volume, react in similar time compared to 140 μm fibers within the uncertainty of diffusion coefficients and cracks measured on larger fibers. The merging of cracks may explain why the reactions occur in similar time despite the volume difference but the current simulation of that model has too many input parameters to allow for a predictive comparison.

6.2.2. Effect of Mg Vapor

Reactions of 100 μm B fibers under Mg vapor pressure reacted between 2 and 6.5 hours at temperatures between 900 and 1000 °C and were similar to reactions in liquid as seen in Figure 6.4. At such high temperatures the vapor pressure ranges from 0.2 atm at 900 °C to 0.64 atm at 1000 °C [93]. The similarity of the reaction curves between liquid and

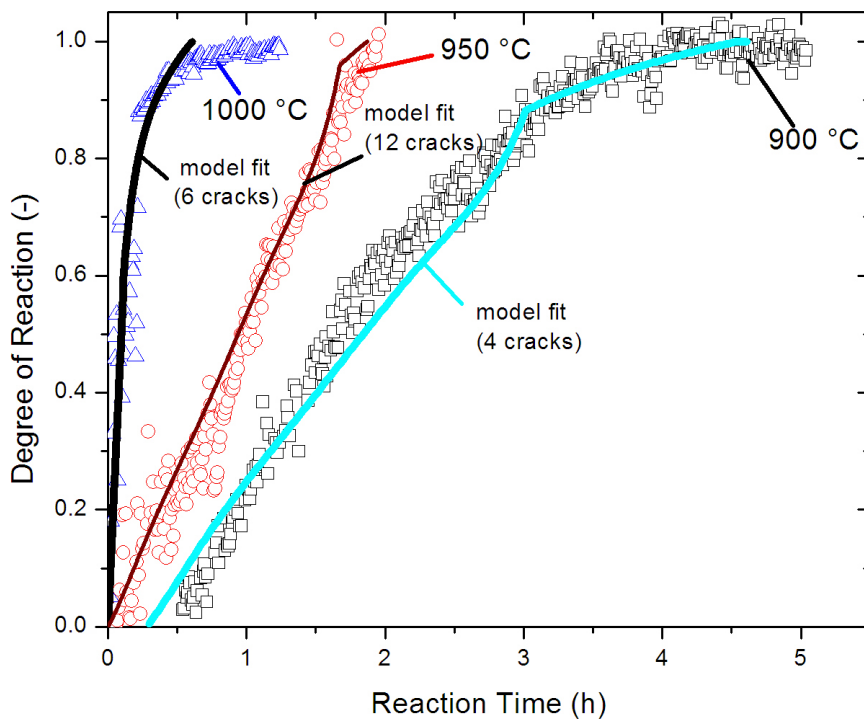


Figure 6.2. Degree of reaction vs time plot for 100 μm B fibers reacted in liquid Mg between 900 and 1000 $^{\circ}\text{C}$ with diffusion and cracking model fits using diffusion coefficients within the uncertainty measured in Chapter 5.

vapor suggested that the flux of Mg due to vapor pressure between 900 and 1000 $^{\circ}\text{C}$ was sufficient to achieve the maximum possible reaction rate.

6.2.3. Effect of Nitrided Surface

Reactions of nitride coated 140 μm B fibers were also similar to non-nitride coated fibers as shown by the degree of reaction vs time curves in Figure 6.5 except for a slight incubation time difference at the higher temperatures where non-nitrided fibers reacted quickly

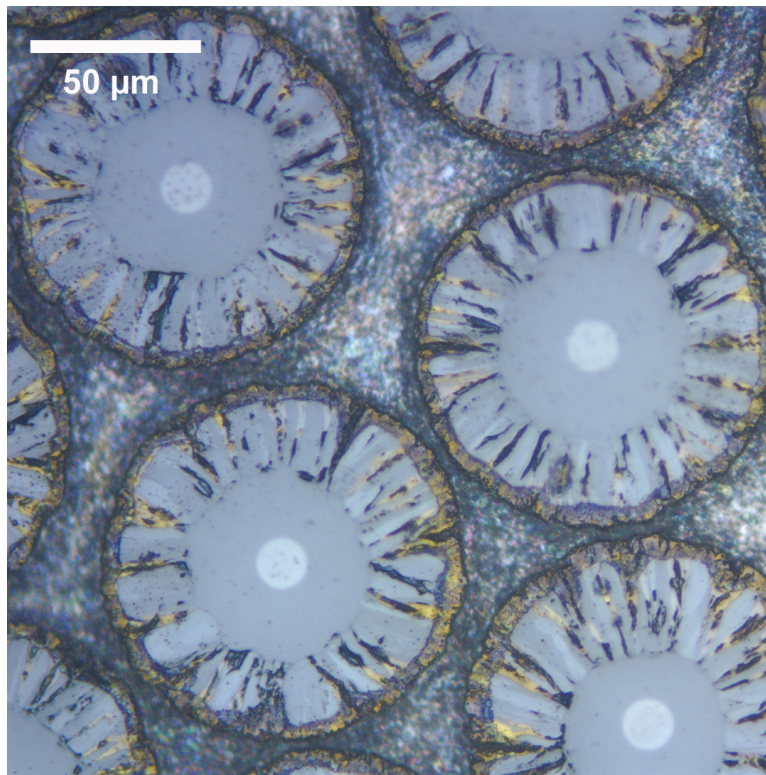


Figure 6.3. Optical micrograph showing 100 μm B fibers reacted for 3 min at 1000 $^{\circ}\text{C}$.

and nitrified fibers show a short delay where a slow reaction proceeds for about 15 min before faster reaction to completion. The nitride coating was visible as a lighter shade in backscattered SEM and was 1.8 - 2.2 μm thick (Figure 6.6(a-b)). Although nitrifying of B fibers was developed to prevent reaction of the B fibers, the technology was developed for use with Al. Mg forms nitrides according to the Mg-N phase diagram [115], and the nitride layer was only 2 μm thick so the nitride layer was reacted quickly resulting in reaction times similar to non-nitrified fibers.

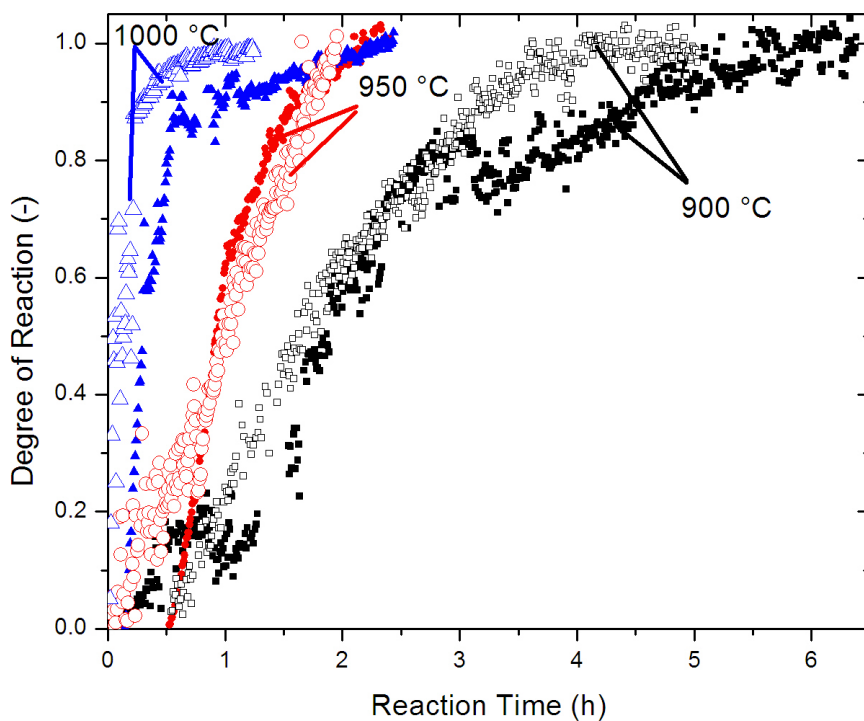


Figure 6.4. Degree of reaction vs time showing reactions of 100 μm B fibers reacted between 900 and 1000 $^{\circ}\text{C}$ in Mg vapor (closed symbols) compared to fibers reacted in Mg liquid (open symbols).

6.2.4. Effect of 0.4 at% C-doping

Thicknesses of MgB_2 reaction shells on 0.4 at% C-doped B fibers were 1.6 μm after reaction in Mg liquid at 1000 $^{\circ}\text{C}$ for 3 min and 3.6 μm after reaction in Mg liquid for 2.5 hrs as shown in Figure 6.7(a-b). Additionally, a fiber reacted for 16.5 h had a reaction layer of 3.9 μm . In contrast, un-doped B fibers fully reacted in 2.5 hrs at 950-1000 $^{\circ}\text{C}$ as discussed in Chapters 4-5 and as shown by Canfield et al [7]. Fit of the Entchev model as shown in Figure 6.8 to these three datapoints resulted in a diffusion coefficient

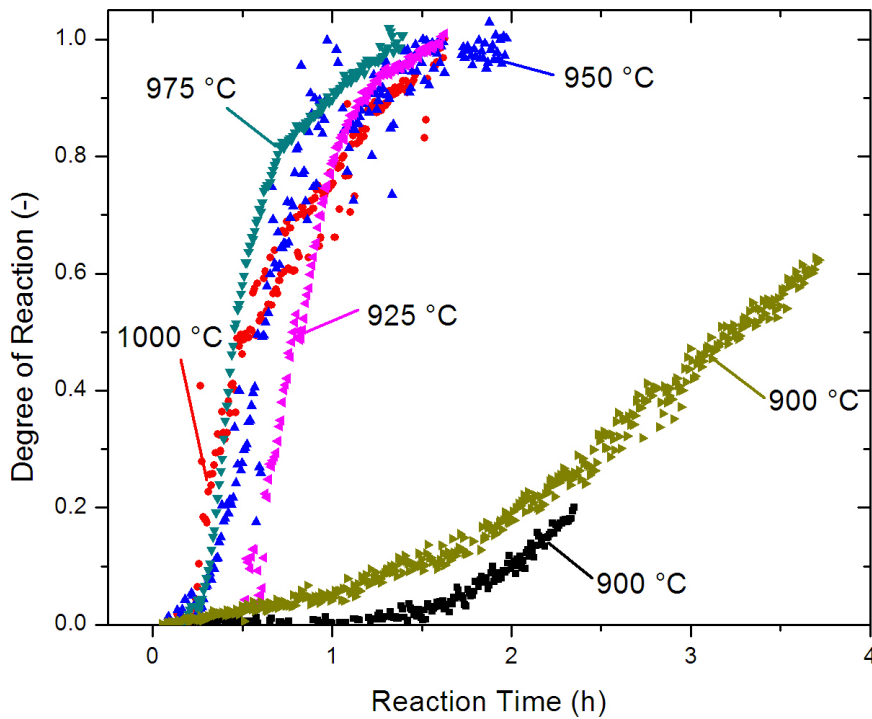


Figure 6.5. Degree of reaction vs time plots showing 140 μm B fibers with nitrided surface reacted between 900 and 1000 $^{\circ}\text{C}$ in Mg liquid.

of $1.4 \cdot 10^{-15} \text{m}^2/\text{s}$ suggesting the C slowed the diffusion as compared to the diffusion coefficient of $9 \cdot 10^{-13} \text{m}^2/\text{s}$ for the reaction of un-doped fibers. The fit was not very accurate suggesting that a mechanism other than diffusion was involved. The MgB_4 reaction front was also not visible as was the case with the reaction fronts of un-doped fibers at 700 and 800 $^{\circ}\text{C}$ temperatures which have similar slower diffusion coefficients.

Possible explanations for the much slower reaction of C-doped fibers include the formation of B_4C , the reduction of the cracking mechanism, and the improved adhesion of

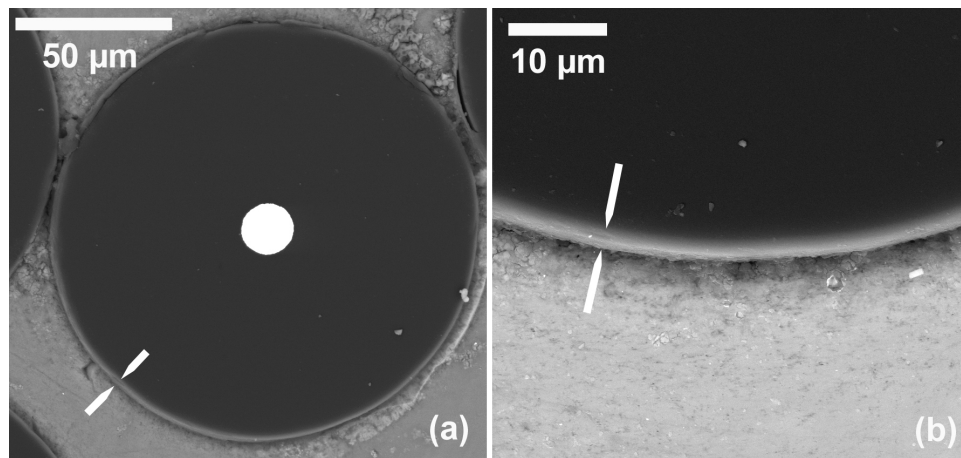


Figure 6.6. Scanning electron micrographs showing (a) 140 μm B fiber with lighter shaded nitride ring on the outer edge of the fiber. (b) shows a higher magnification image of the nitride layer that was determined to be 1.8 - 2.2 μm thick.

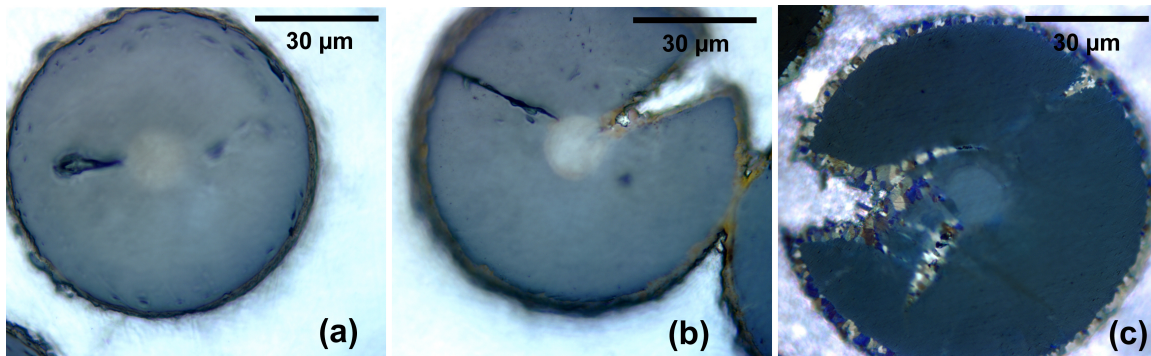


Figure 6.7. Optical micrographs showing 0.4 *at%* C-doped 85 μm B fibers reacted in Mg liquid at 1000 $^{\circ}\text{C}$ for (a) 5 min, (b) 2.5 h, and (c) 16.5 h.

interfaces similar to the effect of rare earth elements on oxide layers in alloys such as Fe-Cr-Al. Long reaction times at high temperatures were reported for the reaction of B_4C to carbon doped MgB_2 [90,118] as well as the reaction of Ti- and C-doped fibers [52,54-56]. B_4C is a highly stable carbide which resists reaction to MgB_2 , but no B_4C was reported for the synthesis of C-doped B fibers by CVD [54]. The cracking of C-doped fibers was not visible but this was likely due to slow diffusion and growth of the MgB_4 front. Similar

reaction fronts were shown with slow diffusion coefficients at 700 and 800 °C (Figures 5.6 - 5.7). The addition of small amounts of C may be similar to the addition of small amount of Y and other rare earth elements to Fe-Cr-Al, and other alumina and chromia forming alloys, which improves adhesion between alloy and oxide layers and resists cracking thus preventing the additional diffusion of oxygen to fully oxidize the alloys [119]. The diffusion of Mg in reacting B fibers to MgB₂ may follow a similar process. If C-doping works by a similar mechanism, it could slow or even prevent the diffusional process, thus slowing the reaction rate. Addition of Y changes oxide growth in Fe-Cr-Al alloys from parabolic to near asymptotic where oxidation proceeds early and then nearly stops, as seen here where reaction thickness at 16.5 h was similar to the reaction thickness after 2.5 h. This would also explain why C-doped powders (Chapter 2) react in similar time to un-doped powders. The powder agglomerates were only 400 nm in size and made up of 10-50 nm spheres so the diffusion of Mg is not necessarily prohibited to react powders in a short amount of time. As shown with fibers, in 5 minutes, a 1.6 μm thick shell of MgB₂ was visible on the outside of the fiber which would be more than enough to react the small powders.

6.2.5. Effect of Thermal Cycling

Fibers reacted under thermal cycling conditions between 668-900 °C were compared to isothermal reactions at 900 °C as shown in Figure 6.9. Although reaction rates in the middle of the curves between 10 and 80% reaction were not significantly increased, it was observed that the fibers reacted under thermally cycled conditions did not have the slow shallower sloped finish to the reaction curve associated with the MgB₂ wedges reaching

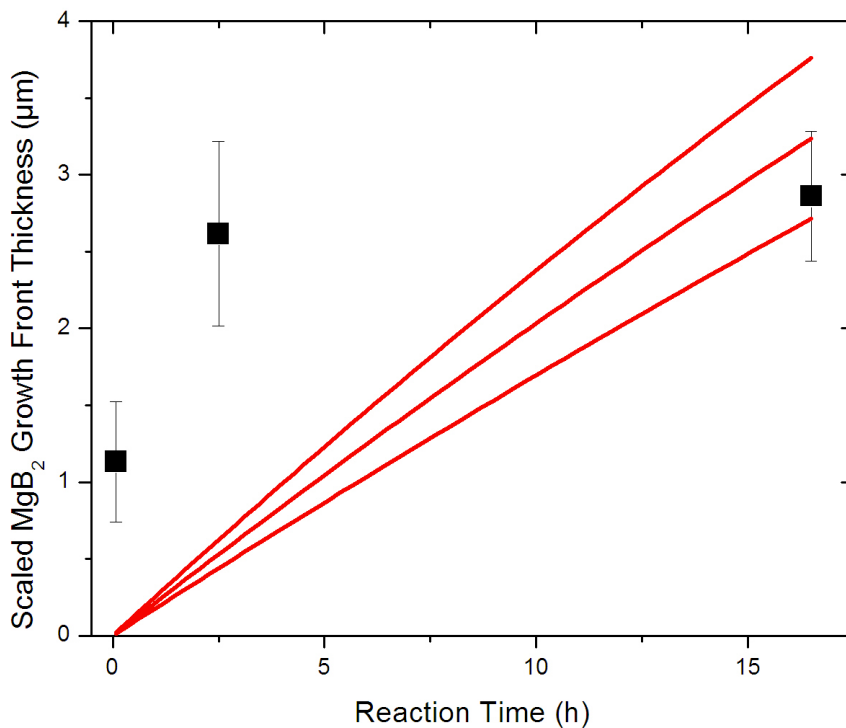


Figure 6.8. Measured MgB₂ thickness vs time for 85 μm C-doped B fibers reacted in liquid Mg at 1000 $^{\circ}\text{C}$. Lines show poor fits of Entchev et al [94] cylinder reaction model.

the fiber core followed by the slow diffusion only reaction of MgB₄ islands. It appeared as though the fibers reacted under thermally cycled conditions finished conversion to MgB₂ in 3.5 hours which was half the time for isothermally reacted fibers as shown in Figure 6.9. This supported the hypothesis that the thermal cycling would aid in enhancing cracking of the MgB₄ due to thermal mismatch and therefore enhance the reaction rate. Changes to the cycling conditions including the cycle amplitude (ΔT) as well as the number of cycles

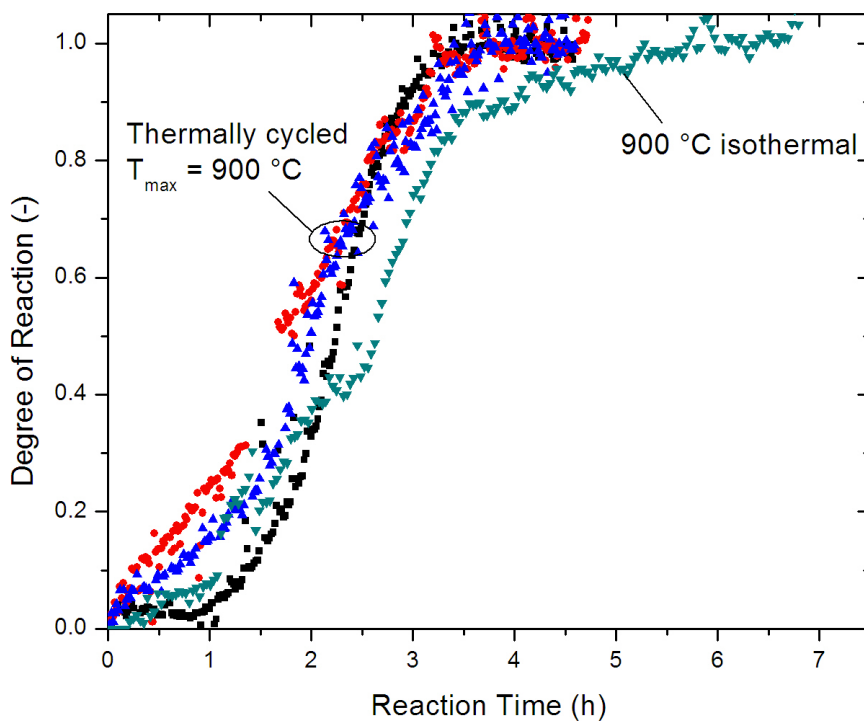


Figure 6.9. Degree of reaction vs time plots showing $140\ \mu\text{m}$ B fibers reacted under thermally cycled conditions compared to isothermal reaction at $900\ ^\circ\text{C}$ where thermal cycling enhanced cracking and reduced the reaction time.

did not show systematic effects in changing the reaction time, as shown in Figure 6.10(a-b). Cracking of the MgB_4 layer occurs in non-thermal cycling conditions as discussed in Chapter 5 and the results suggests that very minimal thermal cycling can enhance this process.

Reactions under thermal cycling conditions between 700 and $1000\ ^\circ\text{C}$ for $24\ \text{h}$ were also performed on C-doped fibers but no enhanced reaction rate was seen likely due to the lack of an MgB_4 reaction front and thus no significant cracking. As discussed above,

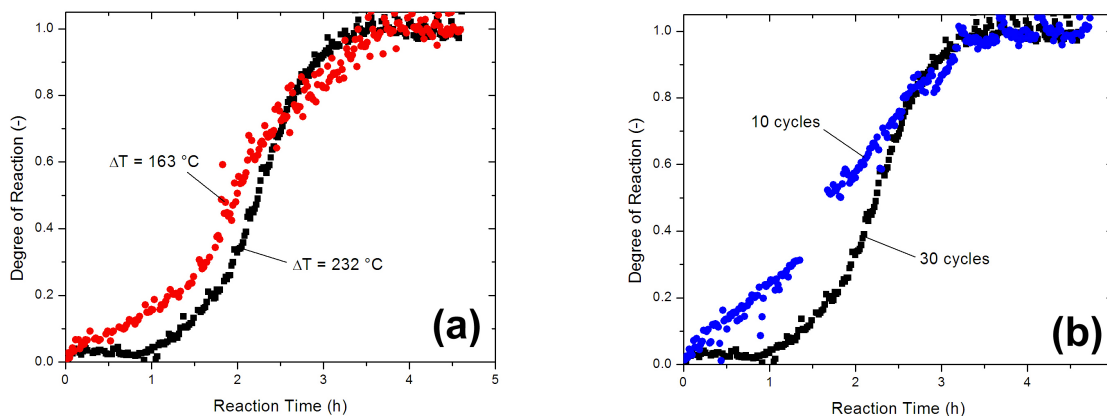


Figure 6.10. Degree of reaction vs time plots comparing different thermal cycling conditions. (a) shows the effect of cycle amplitude (ΔT) on reaction and (b) shows the effect of cycle time on the reaction.

no large MgB_4 diffusion front was observed in reactions of C-doped fibers and thus the cracking mechanism described in Chapter 5 could not be activated.

6.2.6. Broken Fibers

Broken fibers reacted at $900\text{ }^{\circ}\text{C}$ in 5 h less time than full cylindrical fibers and with a more parabolic reaction curve shown in Figure 6.11. Ground fiber pieces were sieved to $25 - 45\text{ }\mu\text{m}$ and resembled powders so the reaction curves, being more parabolic, were well fit by the Carter sphere reaction model (Equation 2.1) as shown in Figure 6.12. Using the characteristic radii r_0 of 12.5 to $22.5\text{ }\mu\text{m}$ as lower and upper bounds, the reaction rate constant from the Carter model was between 6.8×10^{-15} and $2.2 \times 10^{-14}\text{ m}^2/\text{s}$. The reaction rate constant is at least an order of magnitude larger than found for 400 nm powders at $900\text{ }^{\circ}\text{C}$ in Chapter 2. Although the fibers were ground to a finer size, it is likely that cracking was enhancing the reaction rate. MgB_2 was observed growing into cracks in large crystalline B powders ($60 - 140\text{ }\mu\text{m}$) reacted at $800\text{ }^{\circ}\text{C}$ for 2 h as shown

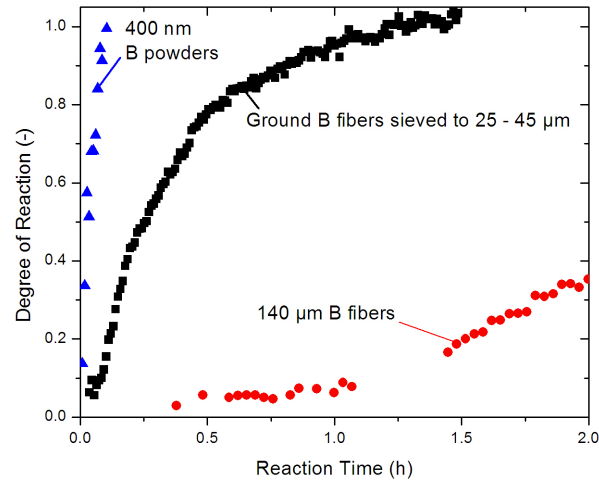


Figure 6.11. Degree of reaction vs time plot showing 100 μm diameter B fibers that were ground and sieved to 25 - 45 μm and reacted at 900 $^{\circ}\text{C}$. Reactions of unbroken 140 μm diameter cylindrical B fibers and 400 nm B powders are shown for comparison.

in Figure 6.13. Powders with a characteristic radius of 200 nm were not large enough for this effect to be significant.

6.3. Conclusions

The effect of B fiber size, fiber surface treatment, fiber doping, Mg vapor, and thermal treatments were investigated to determine effects on reaction kinetics of converting B fibers in MgB_2 . Smaller 100 μm fibers reacted in similar time to 140 μm fibers despite the 50% reduction of volume but expected as shown by fitting to the diffusion and cracking model developed in Chapter 5. A nitride surface treatment and the use of Mg vapor instead of liquid Mg did not affect reaction times. Doping B fibers with 0.4 at% C dramatically decreased reaction rates although the exact mechanism was not determined.

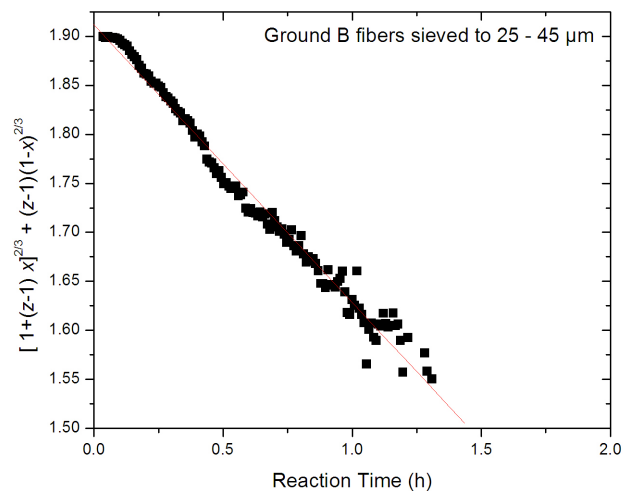


Figure 6.12. Degree of reaction vs time plot using data converted to the Carter sphere model [92] where the slope is related to the reaction rate constant k .

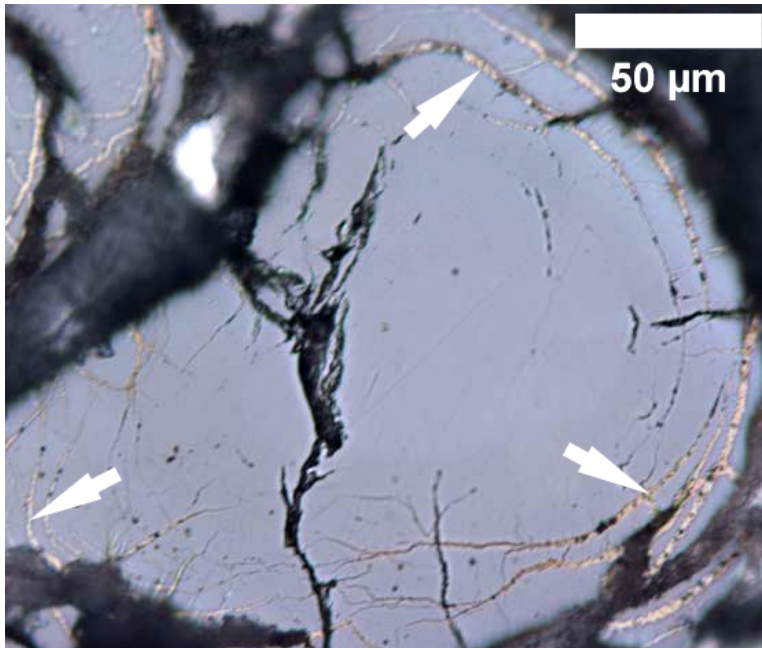


Figure 6.13. Optical micrograph of large crystalline B powders (60 - 140 μm) reacted with liquid Mg at 800 $^{\circ}\text{C}$ for 2 h with arrows indicating regions where MgB_2 grew into cracked regions of a single particle.

Thermal cycling enhanced reaction time through enhanced cracking of the MgB_4 layer in un-doped fibers but did not improve C-doped fiber reaction time due to the lack of MgB_4 growth front. Broken fibers fit well to a model used for powders but a higher reaction rate constant suggested that cracking was increasing reaction rates.

CHAPTER 7

Future Research

The previous chapters have described the processing of MgB_2 from B powder and B fibers and the reactive process application to superconducting metal/ MgB_2 composites whether powder processing within a metallic sheath or infiltration processing with liquid magnesium. This chapter discusses the implications of and questions that arise due to the results of the previous chapters and the future research that will further develop the scientific and technological MgB_2 research fields.

7.1. MgB_2 from powder

7.1.1. Reactions in the solid state

In Chapter 2, the reaction kinetics of synthesizing MgB_2 from Mg and B powders for applications of PIT technology were determined above the melting point of Mg. Recent studies in reaction MgB_2 from powders have reduced reaction temperatures to as low as 450 °C [16] by mechanically milling powders. Additionally, many reactions have occurred at 550 [18] or 600 °C [19] which are also below the 650 °C melting point of Mg. The desire for low temperature is due to the formation of smaller grain size which increases critical current density [19] as well as reduces reaction with sheath materials. These reactions take place from 1200 h time at 550 to 1 h at 600 °C. While 1200 h may be too long for study by in situ synchrotron diffraction, 1 h is possible and would allow the study of the solid state reaction of synthesizing MgB_2 . While it is possible the reaction rates would

be an extrapolation of studies in liquid Mg, the solid state reaction may show deviation from the liquid trend due to the lack of liquid flow wetting the powder agglomerates. Considering low temperature reactions are the current state of the art in MgB₂ PIT synthesis, determining reaction kinetics in the solid state should be investigated.

In synthesizing MgB₂ from powders, especially in the solid state, blending with small Mg powders is as necessary as small B powders to reduce diffusion distances. Two Mg precursors have been used to improve the properties of in situ MgB₂ including the use of thermal plasma processed Mg to form nanoscale powders and the use of MgH₂ as the Mg source [35, 36, 87]. Studies of the reaction using differential thermal analysis show the hydrogen liberated at 500 °C leaving the Mg to react with the B. The hydrogen reacts with oxygen in the system to minimize the formation of MgO and create very clean MgB₂. Creating high quality MgB₂ requires a clean source of Mg and either of these processing methods can create small sized clean Mg for reaction with B in the solid state and should be investigated to determine reaction rates.

7.1.2. Superplastic Forming

Probably the most significant result of this work was presented in Chapter 3, where the possibility of improving PIT MgB₂ by creating dense MgB₂ cores was proposed based on the discovery of high compressive ductility in commercial MgB₂ powders. The significance of the work extends beyond the technological application of possible superplastic forming of PIT MgB₂ wires but also to the scientific questions that arise and the technological potential if the scientific questions are answered.

The biggest question is to whether true tensile superplasticity is possible and by what mechanism is it occurring. Superplasticity has only been seen in a few ceramics as listed in Chapter 3 so the observation of high ductility in MgB_2 may extend to yet another ceramic, or possibly to a class of ceramics considering the family of boride isostructural to MgB_2 including technologically significant borides such as TiB_2 and ZrB_2 . High ductility and superplasticity is always associated with a fine grain size. Here MgB_2 was deformed with as-received powders. While polarized light images showed a fine grain structure, the exact grain size was not known. An interesting study would be to engineer a grain size and measure by analyzing peak widths using x-ray diffraction or image analysis using electron backscattered diffraction (EBSD) in an SEM to identify the orientation of neighboring grains. By using higher reaction temperatures and large B powders, large grained MgB_2 would be produced as opposed to lower reactions temperatures and smaller powders. The powders could then be densified by HIP and tested mechanically and compared to the commercial powders. Additionally, superplastic deformation by grain boundary sliding also requires diffusional accommodation. Doping of MgB_2 by carbon has proved to enhance superconducting properties such as upper critical field [36,54,65] but as shown in Chapter 6, also reduces diffusion in fibers. Although this effect was not significant in powders as shown in Chapter 2, the addition of elements such as C could prove to affect the high ductility. Since doping elements such as C are technologically significant, they must be investigated to determine the feasibility of continuous hot drawing of MgB_2 for PIT wires. Another issue in superplastic deformation is grain growth due to high temperatures. The commercial powders discussed in Chapter 3 did not increase in grain size after testing between 900 and 1000 °C. This might be do to a low homologous temperature but could

also be due to MgO at grain boundaries preventing grain growth at high temperature. Studies with commercial MgB₂ powders typically report 2 – 5% MgO by x-ray diffraction [89, 104]. To investigate this possibility, MgB₂ should be synthesized with very pure compounds such as using the powders in Chapter 2, which were 99.99% to 99.999% pure B reacted with MgH₂ or distilled Mg vapor. Reaction temperatures should be low to produce a small grain size then HIP'd to density at high temperature and determine any grain growth followed by mechanical testing at high temperature to again assess ductility and grain growth with MgO. If the processing parameters to facilitate high ductility in MgB₂ can be determined, MgB₂ should also be tested in tension to determine if real superplasticity exists.

While demonstrating high ductility and superplasticity and determining the processing techniques and mechanisms that result in these properties in MgB₂ is an important scientific study, the overall technical application is for creating dense core PIT MgB₂ wires and should be demonstrated. As discussed in Chapter 3, the stress state of extrusion or wire drawing is different than the uniaxial compression testing where the high ductility was demonstrated. There are many studies as highlighted in Chapter 1 that vary the deformation technique, precursor powders, and reaction temperature and result in different MgB₂ superconducting properties. Both in situ and ex situ techniques should be examined to determine the feasibility in each case of applying a high temperature heat treatment to densify the MgB₂ core. For in situ processing, Mg and B powders should be drawn and then reacted at low temperature to produce the desired fine grain structure. This should be compared to a similarly reacted PIT MgB₂ wire where the wire is then additionally deformed at high temperature to produce a dense core. For ex situ processing,

the comparisons between as-drawn, drawn + annealed, and drawn + high temperature densification should be compared to determine what happens at each stage of the reaction and how it affects the core density and superconducting properties.

In the studies presented in this work, experiments were focused on the processing of MgB_2 but not correlated to superconducting properties. Experiments were developed to determine reaction kinetics but not to optimize or determine variance in superconducting properties that are of importance to the technological development of MgB_2 . While other studies report smaller grain size at lower reaction temperatures [19, 120], a systematic study has not been completed also correlating to critical current density as a function of grain size and reaction temperature. Grain size will also be important to the ductility at high temperature. Combining the work of powders presented in this work, as well as the proposed research above, the full technological assessment of reacting powders and deforming into dense wire should include the study of grain size and growth, carbon doping, and high temperature deformation. The assessment should measure the superconducting transition temperature which should decrease with the C [54] as well as critical current density under applied magnetic field since showing high J_c under self field does not necessarily correlate to high J_c under higher applied fields, which are important to the further development of MgB_2 in applications beyond small fields.

7.2. MgB_2 from fibers

The largest unanswered question that comes from the study of fiber reactions presented in Chapter 6 is the mechanism by which C is acting to prevent reaction of C-doped fibers. Ex situ reaction kinetics should be done on C-doped fibers similarly to un-doped fibers

in Chapter 5 to determine whether the reaction is by diffusion, diffusion with cracking, or some other mechanism. Additionally the mechanism by which diffusion or cracking is slowed should first be assessed by determining where the carbon is located in the MgB_2 . Due to the small amount of C, atom by atom resolution may be needed as found with local electron atom probe (LEAP) tomography where individual atoms are evaporated from a sample using an electrical pulse with position and composition determined using a time of flight detector. The largest difficulty with LEAP on MgB_2 is the sample preparation. The formation of MgB_2 from carbon doped fibers is difficult enough, then the fiber needs to be developed into a nanoscale tip through chemical or mechanical processes. The fiber begins around $100 \mu\text{m}$ in diameter. Dual beam FIB has shown the ability to make fine tips from MgB_2 (Figure 7.1) but such a small tip on a large fiber was difficult to find and perform the LEAP experiment on. If the location of C is determined to be segregating to interfaces, the mechanism may prove to be similar to the effect of Y in alumina and chromia forming alloys as discussed in Chapter 6. Additionally, C-doped fibers are produced with higher dopant levels of carbon (up to 5.2 at%). Superconducting transition temperature was shown to decrease with additional C [54] but upper critical field was increased to 36 T [55] at the highest C-dopant level. Reactions were performed at similar time and temperature whether there was a lot of carbon or little. The amount of C may also affect the reaction kinetics and would be an interesting study with the techniques outlined above.

The model developed in Chapter 5 to show the effects of cracking and diffusion in the degree of reaction vs time curves for the reaction of un-doped B fibers into MgB_2 had limitations that could be further developed into a more robust model. In Chapter

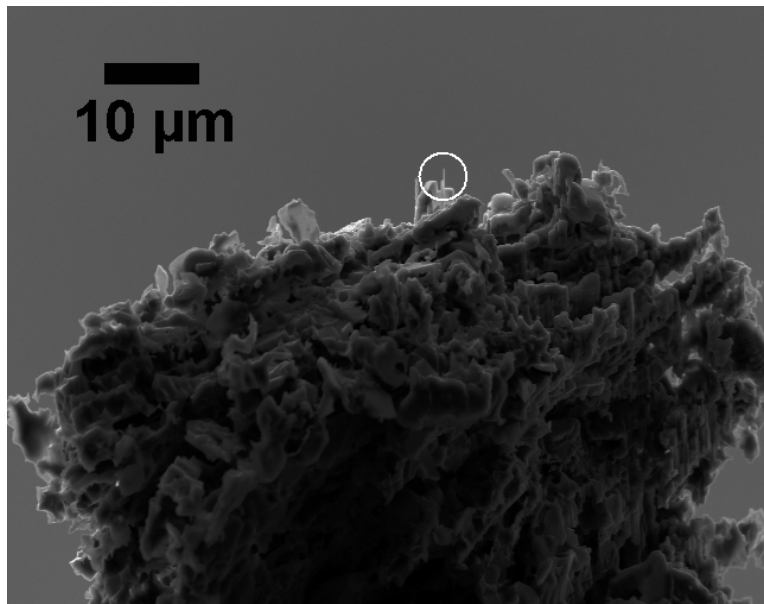


Figure 7.1. Needle shaped tip (circled) of MgB₂ created by dual beam FIB of a section of a 190 μm MgB₂ fiber.

5, an adjustment to the model was made that simulated the effect of cracks merging where a certain fraction of the fiber was reacted by cracking and diffusion and the other wedges reacted by only diffusion. The next iteration of the model would be to include a random position of reacted wedges around the fiber based on the number of cracks, calculating the reaction time for each wedge and summing all the wedges to determine the reaction of a full fiber. Some wedges will be thin and react quickly while others will be wider and react more slowly. The equations for the reaction of a single wedge of a fiber assuming a uniform crack distribution was developed in this work and just needs to be extended to calculating multiple cracks. This will illuminate the idea that the many cracks seen early in ex situ analyzed fiber reactions as shown in Chapter 5 merge to create the reaction curves seen with in situ experiments which were best fit with only 4-8 cracks. The model of this work was based on assumptions observed in microstructure development.

The next iteration of the model should be based on earlier principals that led to the microstructure development. The issue of the wedge growth into cracks was attributed to both stresses caused by volume expansion as well as the possibility of diffusion along grain boundaries. The stresses created by the volume expansion could be calculated by finite element modeling. Strength of MgB_4 could be estimated from hardness measurements on the partially reacted fibers and the amount of growth required to crack the MgB_4 layer incorporated into the model. To further assess the grain boundary diffusion contribution such as why all the MgB_4 grains do not show MgB_2 growth between them, microstructures could be studied using EBSD mapping where individual grains orientations of MgB_4 would be determined. Grain boundary angle and spacing calculated from the known orientations would provide additional information into how the wedge growth of MgB_2 ahead of the diffusion reaction front proceeds. Instead of inputting the number of cracks into the model, the model would proceed based only on diffusion coefficients with the orientation and size of MgB_4 grains determining the number and spacing of cracks in the fiber.

7.3. Reaction of fibers under stress

Further development of the use of commercial B fibers to create Mg/MgB_2 composites must consider the possibility of winding the wires into a coil for magnets. Due to the brittleness of MgB_2 , it is unlikely that wires could be wound to small radii of curvatures without fracturing the individual fibers. An alternative processing route where the strong and flexible B fibers are placed within tubing with one end sealed and then wound into the coil before infiltration would solve the problem of winding the wires. However, the large cracks that develop may create problems with this processing route. The reaction

of B fibers under stress was investigated by winding a B fiber around 6.35 mm Ti tube and placing within a 12.7 mm inner diameter carbon steel tube with one end welded shut. Mg was added and the sample sealed by welding the top closed as well. The sample was heated to 950 °C for 2.5 h to react the B fiber. After the experiment, it was observed that the Mg melted and infiltrated everywhere in the carbon steel crucible. However, after machining off the steel and dissolving the Mg in HCl, no B fiber coil was observed. It was possible that the fiber broke during dissolution as the violent dissolution of Mg by HCl caused the sample to fall over or the fiber was in the acid too long and dissolved. Future attempts to react fibers under stress can duplicate this reaction process but the Mg should be evaporated by placing a closed end metal tube over the reaction crucible and heating the crucible in vacuum at 900 °C with the closed end of the metal tube below the melting point of Mg which causes the Mg to condense onto the metal tube and gently removes it from the sample. Additionally, fibers could be placed into a small diameter metal tube with one end welded shut and then bent before infiltration with Mg and then reaction under the stress within the liquid Mg. After reaction, the bent section of the tube could be sectioned and examined to observe the microstructure of a fiber reacted under stress or the metal tube and Mg dissolved to show a bent MgB₂ fiber.

7.4. Improving Reaction Rates

Thermal cycling showed some improvement to the reaction time of un-doped fibers but did not improve the more technologically important doped fiber reaction time. This was likely due to the lack of an MgB₄ growth front that would crack due to the slow diffusion in the doped fiber. The microstructure development of C-doped fibers reacted

at higher temperatures has not been studied. The formation of an MgB_4 front at a higher temperature would provide an upper bound to a thermal cycling reaction procedure that may prove to show an improvement in reaction rate of doped fibers. However, the reaction rate will likely not rival that of powders which react in under 2 hours at a range of lower temperatures near the melting point of Mg. The technological race for the production of high critical current density and high field MgB_2 wires is between the fiber processing technique which has the desired properties but not the ease of fabrication and if the powder-in-tube procedure which has the ease of fabrication but not the properties. However, properties are close and if the procedures discussed above work, the PIT process will have both the properties and ease of fabrication.

7.5. MgB_2 from liquid

Another method for creating composites through in situ routes is by directional solidification where the composition is a liquid at high temperature but upon solidification typically through a eutectic point, the liquid becomes two solids and in some cases fibers are grown [121]. Ternary and higher component phase diagrams involving Mg and B are uncommon so synthesizing MgB_2 from the liquid state does not have a solid scientific foundation. However, in examining binary phase diagrams, it is known that Cu does not form a boride and dissolves up to 2% B at fairly accessible temperatures around 1000 °C [115]. The system was investigated by Souptel et al [122] and MgB_2 was precipitated from the melt, but at high boron compositions where MgB_4 and MgB_7 were also observed. Investigations near the B eutectic point with Cu were not completed. One experiment was performed in this range using a eutectic Cu-B alloy and Mg. The metals were sealed

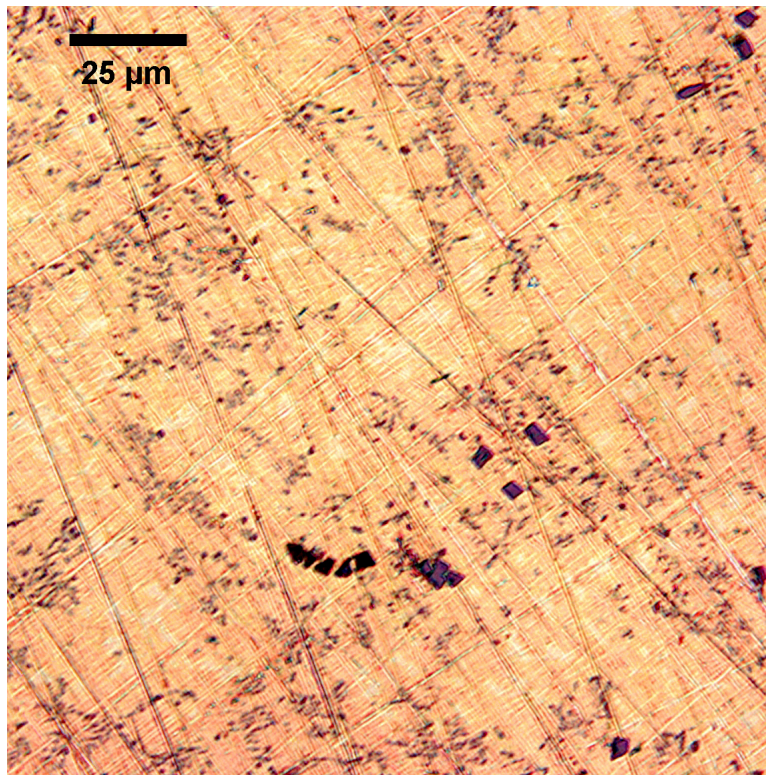


Figure 7.2. Optical micrograph showing microstructure of Cu-Mg-B melt quenched from 1200 °C determined by XRD to be a copper alloy matrix with MgB_4 and MgB_7 precipitates.

in Y_2O_3 coated stainless steel and heated to 1200 °C for 4 h and then quenched. Composition showed a copper alloy matrix with two different precipitates as shown in Figure 7.2 which were confirmed to be MgB_4 and MgB_7 in a Cu alloy matrix by XRD. This result suggested that more Mg was needed to balance what alloys with Cu and what forms the boride as well as any losses due to the high vapor pressure or reactions with the steel or Y_2O_3 .

References

- [1] J. Nagamatsu, N. Nakagawa, T. Muranaka, Y. Zenitani, and J. Akimitsu. Superconductivity at 39 k in magnesium diboride. *Nature*, 410(6824):63–64, 2001.
- [2] S. L. Bud'ko, G. Lapertot, C. Petrovic, C. E. Cunningham, N. Anderson, and P. C. Canfield. Boron isotope effect in superconducting mgb_2 . *Physical Review Letters*, 86(9):1877–1880, 2001.
- [3] S. Souma, Y. Machida, T. Sato, T. Takahashi, H. Matsui, S. C. Wang, H. Ding, A. Kaminski, J. C. Campuzano, S. Sasaki, and K. Kadowaki. The origin of multiple superconducting gaps in mgb_2 . *Nature*, 423(6935):65–67, 2003.
- [4] H. J. Choi, D. Roundy, H. Sun, M. L. Cohen, and S. G. Louie. The origin of the anomalous superconducting properties of mgb_2 . *Nature*, 418(6899):758–760, 2002.
- [5] M.L. Young, J. DeFouw, J.D. Almer, and D.C. Dunand. Load partitioning during compressive loading of a mg/mgb_2 composite. *Acta Materialia*, page doi:10.1016/j.actamat.2007.01.046, 2007.
- [6] P. C. Canfield and G. Crabtree. Magnesium diboride: Better late than never. *Physics Today*, 56(3):34–40, 2003.
- [7] P. C. Canfield, D. K. Finnemore, S. L. Bud'ko, J. E. Ostenson, G. Lapertot, C. E. Cunningham, and C. Petrovic. Superconductivity in dense mgb_2 wires. *Physical Review Letters*, 86(11):2423–2426, 2001.
- [8] William D. Callister. *Materials science and engineering : an introduction*. John Wiley & Sons, New York, NY, 6th edition, 2003.
- [9] D. C. Larbalestier, L. D. Cooley, M. O. Rikel, A. A. Polyanskii, J. Jiang, S. Patnaik, X. Y. Cai, D. M. Feldmann, A. Gurevich, A. A. Squitieri, M. T. Naus, C. B. Eom, E. E. Hellstrom, R. J. Cava, K. A. Regan, N. Rogado, M. A. Hayward, T. He, J. S. Slusky, P. Khalifah, K. Inumaru, and M. Haas. Strongly linked current flow

- in polycrystalline forms of the superconductor mgb_2 . *Nature*, 410(6825):186–189, 2001.
- [10] X. Y. Song, S. E. Babcock, C. B. Eom, D. C. Larbalestier, K. A. Regan, R. J. Cava, S. L. Bud'Ko, P. C. Canfield, and D. K. Finnemore. Anisotropic grain morphology, crystallographic texture and their implications for flux pinning mechanisms in mgb_2 pellets, filaments and thin films. *Superconductor Science & Technology*, 15(4):511–518, 2002.
- [11] D. Larbalestier, A. Gurevich, D. M. Feldmann, and A. Polyanskii. High-t-c superconducting materials for electric power applications. *Nature*, 414(6861):368–377, 2001.
- [12] S. H. Zhou, A. V. Pan, H. K. Liu, and S. X. Dou. Single- and multi-filamentary fe-sheathed mgb_2 wires. *Physica C-Superconductivity and Its Applications*, 382(4):349–354, 2002.
- [13] D. K. Aswal, S. Sen, A. Singh, T. V. C. Rao, J. C. Vyas, L. C. Gupta, S. K. Gupta, and V. C. Sahni. Synthesis and characterization of mgb_2 superconductor. *Physica C*, 363(3):149–154, 2001.
- [14] A. Gumbel, J. Eckert, G. Fuchs, K. Nenkov, K. H. Muller, and L. Schultz. Improved superconducting properties in nanocrystalline bulk mgb_2 . *Applied Physics Letters*, 80(15):2725–2727, 2002.
- [15] A. Handstein, D. Hinz, G. Fuchs, K. H. Muller, K. Nenkov, O. Gutfleisch, V. N. Narozhnyi, and L. Schultz. Fully dense mgb_2 superconductor textured by hot deformation. *Journal of Alloys and Compounds*, 329(1-2):285–289, 2001.
- [16] N. M. Strickland, R. G. Buckley, and A. Otto. High critical current densities in cu-sheathed mgb_2 formed from a mechanically-alloyed precursor. *Applied Physics Letters*, 83(2):326–328, 2003.
- [17] N. N. Kolesnikov and M. P. Kulakov. Synthesis of mgb_2 from elements. *Physica C*, 363(3):166–169, 2001.
- [18] A. Yamamoto, J. Shimoyama, S. Ueda, Y. Katsura, I. Iwayama, S. Horii, and K. Kishio. Effects of sintering conditions on critical current properties and microstructures of mgb_2 bulks. *Physica C-Superconductivity and Its Applications*, 426:1220–1224, 2005.

- [19] A. Yamamoto, J. Shimoyama, S. Ueda, Y. Katsura, S. Horii, and K. Kishio. Improved critical current properties observed in mgb_2 bulks synthesized by low-temperature solid-state reaction. *Superconductor Science & Technology*, 18(1):116–121, 2005.
- [20] T. C. Shields, K. Kawano, D. Holdom, and J. S. Abell. Microstructure and superconducting properties of hot isostatically pressed mgb_2 . *Superconductor Science & Technology*, 15(2):202–205, 2002.
- [21] Y. Takano, H. Takeya, H. Fujii, H. Kumakura, T. Hatano, K. Togano, H. Kito, and H. Ihara. Superconducting properties of mgb_2 bulk materials prepared by high-pressure sintering. *Applied Physics Letters*, 78(19):2914–2916, 2001.
- [22] S. S. Indrakanti, V. F. Nesterenko, M. B. Maple, N. A. Frederick, W. H. Yuhasz, and S. Li. Hot isostatic pressing of bulk magnesium diboride: mechanical and superconducting properties. *Philosophical Magazine Letters*, 81(12):849–857, 2001.
- [23] N. A. Frederick, S. Li, M. B. Maple, V. F. Nesterenko, and S. S. Indrakanti. Improved superconducting properties of mgb_2 . *Physica C*, 363(1):1–5, 2001.
- [24] C. U. Jung, M. S. Park, W. N. Kang, M. S. Kim, K. H. P. Kim, S. Y. Lee, and S. I. Lee. Effect of sintering temperature under high pressure on the superconductivity of mgb_2 . *Applied Physics Letters*, 78(26):4157–4159, 2001.
- [25] X. L. Wang, S. Soltanian, J. Horvat, A. H. Liu, M. J. Qin, H. K. Liu, and S. X. Dou. Very fast formation of superconducting mgb_2/fe wires with high $j(c)$. *Physica C*, 361(3):149–155, 2001.
- [26] H. Kitaguchi, A. Matsumoto, H. Hatakeyama, and H. Kumakura. High temperature performance of mgb_2 powder-in-tube composite tapes. *Superconductor Science & Technology*, 17(9):S486–S489, 2004.
- [27] A. V. Pan, S. H. Zhou, H. K. Liu, and S. X. Don. Properties of superconducting mgb_2 wires: in situ versus ex situ reaction technique. *Superconductor Science & Technology*, 16(5):639–644, 2003.
- [28] Y. Feng, Y. Zhao, A. K. Pradhan, L. Zhou, P. X. Zhang, X. H. Liu, P. Ji, S. J. Du, C. F. Liu, Y. Wu, and N. Koshizuka. Fabrication and superconducting properties of mgb_2 composite wires by the pit method. *Superconductor Science & Technology*, 15(1):12–15, 2002.

- [29] S. I. Schlachter, A. Frank, B. Ringsdorf, H. Orschulko, B. Obst, B. Liu, and W. Goldacker. Suitability of sheath materials for mgb_2 powder-in-tube superconductors. *Physica C-Superconductivity and Its Applications*, 445:777–783, 2006.
- [30] J. Horvat, X. L. Wang, S. Soltanian, and S. X. Dou. Improvement of critical current in mgb_2/fe superconducting wires by a ferromagnetic sheath. *Applied Physics Letters*, 80(5):829–831, 2002.
- [31] S. Soltanian, X. L. Wang, I. Kusevic, E. Babic, A. H. Li, M. J. Qin, J. Horvat, H. K. Liu, E. W. Collings, E. Lee, M. D. Sumption, and S. X. Dou. High-transport critical current density above 30 k in pure fe-clad mgb_2 tape. *Physica C*, 361(2):84–90, 2001.
- [32] H. Yamada, M. Hirakawa, H. Kumakura, A. Matsumoto, and H. Kitaguchi. Critical current densities of powder-in-tube mgb_2 tapes fabricated with nanometer-size mg powder. *Applied Physics Letters*, 84(10):1728–1730, 2004.
- [33] H. Yamada, N. Uchiyama, A. Matsumoto, H. Kitaguchi, and H. Kumakura. Superconducting properties of in situ powder-in-tube-processed mgb_2 tapes fabricated with sub-micrometre mg powder prepared by an arc-plasma method. *Superconductor Science & Technology*, 20(1):1–4, 2007.
- [34] T. Nakane, H. Kitaguchi, H. Fujii, and H. Kumakura. Improvement of ex-situ mgb_2 powder in tube processed tapes using mgh_2 powder. *Physica C-Superconductivity and Its Applications*, 445:784–787, 2006.
- [35] H. Fujii, K. Togano, and H. Kumakura. Enhancement of critical current densities of powder-in-tube processed mgb_2 tapes by using mgh_2 as a precursor powder. *Superconductor Science & Technology*, 15(11):1571–1576, 2002.
- [36] A. Matsumoto, H. Kumakura, H. Kitaguchi, and H. Hatakeyama. Effect of siO_2 and sic doping on the powder-in-tube processed mgb_2 tapes. *Superconductor Science & Technology*, 16(8):926–930, 2003.
- [37] A. Matsumoto, H. Kumakura, H. Kitaguchi, B. J. Senkowicz, M. C. Jewell, E. E. Hellstrom, Y. Zhu, P. M. Voyles, and D. C. Larbalestier. Evaluation of connectivity, flux pinning, and upper critical field contributions to the critical current density of bulk pure and sic-alloyed mgb_2 . *Applied Physics Letters*, 89(13):–, 2006.
- [38] H. L. Suo, C. Beneduce, X. D. Su, and R. Flukiger. Fabrication and transport critical currents of multifilamentary mgb_2/fe wires and tapes. *Superconductor Science & Technology*, 15(7):1058–1062, 2002.

- [39] P. Kovac, I. Husek, W. Pachla, T. Melisek, R. Diduszko, K. Frohlich, A. Morawski, A. Presz, and D. Machajdik. Structure, grain connectivity and pinning of as-deformed commercial mgb_2 powder in cu and fe/cu sheaths. *Superconductor Science & Technology*, 15(7):1127–1132, 2002.
- [40] G. Grasso, A. Malagoli, C. Ferdeghini, S. Roncallo, V. Braccini, A. S. Siri, and M. R. Cimberle. Large transport critical currents in unsintered mgb_2 superconducting tapes. *Applied Physics Letters*, 79(2):230–232, 2001.
- [41] A. Serquis, L. Civale, D. L. Hammon, X. Z. Liao, J. Y. Coulter, Y. T. Zhu, M. Jaime, D. E. Peterson, F. M. Mueller, V. F. Nesterenko, and Y. Gu. Hot isostatic pressing of powder in tube mgb_2 wires. *Applied Physics Letters*, 82(17):2847–2849, 2003.
- [42] H. Kumakura, A. Matsumoto, H. Fujii, and K. Togano. High transport critical current density obtained for powder-in-tube-processed mgb_2 tapes and wires using stainless steel and cu-ni tubes. *Applied Physics Letters*, 79(15):2435–2437, 2001.
- [43] A. Sharoni, O. Millo, G. Leitus, and S. Reich. Spatial variations of the superconductor gap structure in mgb_2/al composite. *Journal of Physics-Condensed Matter*, 13(22):L503–L508, 2001.
- [44] S. N. Ermolov, M. V. Indenbom, A. N. Rossolenko, I. K. Bdikin, L. S. Uspenskaya, N. S. Stepakov, and V. G. Glebovskii. Superconducting mgb_2 films obtained by magnetron sputtering. *Jetp Letters*, 73(10):557–561, 2001.
- [45] G. Balducci, S. Brutti, A. Ciccioi, G. Gigli, P. Manfrinetti, A. Palenzona, M. F. Butman, and L. Kudin. Thermodynamics of the intermediate phases in the mg-b system. *Journal of Physics and Chemistry of Solids*, 66(2-4):292–297, 2005.
- [46] Q. Li, G. D. Gu, and Y. Zhu. High critical-current density in robust mgb_2/mg nanocomposites. *Applied Physics Letters*, 82(13):2103–2105, 2003.
- [47] G. Giunchi, S. Ceresara, G. Ripamonti, A. Di Zenobio, S. Rossi, S. Chiarelli, M. Spadoni, R. Wesche, and P. L. Bruzzone. High performance new mgb_2 superconducting hollow wires. *Superconductor Science & Technology*, 16(2):285–291, 2003.
- [48] D. C. Dunand. Synthesis of superconducting mg/ mgb_2 composites. *Applied Physics Letters*, 79(25):4186–4188, 2001.
- [49] J. S. Rhyee, C. A. Kim, B. K. Cho, and J. T. Kim. Enhancement of mechanical and superconducting properties of mgb_2 . *Applied Physics Letters*, 80(23):4407–4409, 2002.

- [50] Krishan Kumar Chawla. *Fibrous materials*. Cambridge solid state science series. Cambridge University Press, Cambridge, England ; New York, 1998.
- [51] Y. Y. Wu, B. Messer, and P. D. Yang. Superconducting mgb_2 nanowires. *Advanced Materials*, 13(19):1487–+, 2001.
- [52] D. K. Finnemore, W. E. Straszheim, S. L. Bud'ko, P. C. Canfield, N. E. Anderson, and R. J. Suplinskas. Cvd routes to mgb_2 conductors. *Physica C-Superconductivity and Its Applications*, 385(1-2):278–285, 2003.
- [53] N. E. Anderson, W. E. Straszheim, S. L. Bud'ko, P. C. Canfield, D. K. Finnemore, and R. J. Suplinskas. Titanium additions to mgb_2 conductors. *Physica C-Superconductivity and Its Applications*, 390(1):11–15, 2003.
- [54] R. H. T. Wilke, S. L. Bud'ko, P. C. Canfield, D. K. Finnemore, R. J. Suplinskas, and S. T. Hannahs. Systematic effects of carbon doping on the superconducting properties of $\text{mg}(\text{b1-xcx})(2)$. *Physical Review Letters*, 92(21):–, 2004.
- [55] R. H. T. Wilke, S. L. Bud'ko, P. C. Canfield, D. K. Finnemore, R. J. Suplinskas, and S. T. Hannahs. Synthesis and optimization of $\text{mg}(\text{b1-xcx})(2)$ wire segments. *Physica C-Superconductivity and Its Applications*, 424(1-2):1–16, 2005.
- [56] R. H. T. Wilke, S. L. Bud'ko, P. C. Canfield, M. J. Kramer, Y. Q. Wu, D. K. Finnemore, R. J. Suplinskas, J. C. Marzik, and S. T. Hannahs. Superconductivity in mgb_2 doped with ti and c. *Physica C-Superconductivity and Its Applications*, 418(3-4):160–167, 2005.
- [57] R. J. Cava, H. W. Zandbergen, and K. Inumaru. The substitutional chemistry of mgb_2 . *Physica C-Superconductivity and Its Applications*, 385(1-2):8–15, 2003.
- [58] S. X. Dou, S. Soltanian, J. Horvat, X. L. Wang, S. H. Zhou, M. Ionescu, H. K. Liu, P. Munroe, and M. Tomsic. Enhancement of the critical current density and flux pinning of mgb_2 superconductor by nanoparticle sic doping. *Applied Physics Letters*, 81(18):3419–3421, 2002.
- [59] Y. Zhao, Y. Feng, C. H. Cheng, L. Zhou, Y. Wu, T. Machi, Y. Fudamoto, N. Koshizuka, and M. Murakami. High critical current density of mgb_2 bulk superconductor doped with ti and sintered at ambient pressure. *Applied Physics Letters*, 79(8):1154–1156, 2001.
- [60] Y. Zhao, Y. Feng, D. X. Huang, T. Machi, C. H. Cheng, K. Nakao, N. Chikamoto, Y. Fudamoto, N. Koshizuka, and M. Murakami. Doping effect of zr and ti on

- the critical current density of MgB_2 bulk superconductors prepared under ambient pressure. *Physica C-Superconductivity and Its Applications*, 378:122–126, 2002.
- [61] S. Jin, H. Mavoori, C. Bower, and R. B. van Dover. High critical currents in iron-clad superconducting MgB_2 wires. *Nature*, 411(6837):563–565, 2001.
- [62] M. N. Kunchur, S. I. Lee, and W. N. Kang. Pair-breaking critical current density of magnesium diboride. *Physical Review B*, 68(6):–, 2003.
- [63] X. H. Zeng, A. V. Pogrebnyakov, A. Kotcharov, J. E. Jones, X. X. Xi, E. M. Lysczek, J. M. Redwing, S. Y. Xu, J. Lettieri, D. G. Schlom, W. Tian, X. Q. Pan, and Z. K. Liu. In situ epitaxial MgB_2 thin films for superconducting electronics. *Nature Materials*, 1(1):35–38, 2002.
- [64] S. K. Chen, K. S. Tan, B. A. Glowacki, W. K. Yeoh, S. Soltanian, J. Horvat, and S. X. Dou. Effect of heating rates on superconducting properties of pure MgB_2 , carbon nanotube- and nano-sic-doped in situ MgB_2/Fe wires. *Applied Physics Letters*, 87(18):–, 2005.
- [65] M. D. Sumption, M. Bhatia, M. Rindfleisch, M. Tomsic, S. Soltanian, S. X. Dou, and E. W. Collings. Large upper critical field and irreversibility field in MgB_2 wires with sic additions. *Applied Physics Letters*, 86(9):–, 2005.
- [66] S. X. Dou, W. K. Yeoh, J. Horvat, and M. Ionescu. Effect of carbon nanotube doping on critical current density of MgB_2 superconductor. *Applied Physics Letters*, 83(24):4996–4998, 2003.
- [67] J. H. Kim, W. K. Yeoh, M. J. Qin, X. Xu, and S. X. Dou. The doping effect of multiwall carbon nanotube on MgB_2/Fe superconductor wire. *Journal of Applied Physics*, 100(1):–, 2006.
- [68] S. X. Dou, W. K. Yeoh, O. Shcherbakova, D. Weyler, Y. Li, Z. M. Ren, P. Munroe, S. K. Chen, K. S. Tan, B. A. Glowacki, and J. L. MacManus-Driscoll. Alignment of carbon nanotube additives for improved performance of magnesium diboride superconductors. *Advanced Materials*, 18(6):785–+, 2006.
- [69] Y. W. Ma, X. P. Zhang, G. Nishijima, K. Watanabe, S. Awaji, and X. D. Bai. Significantly enhanced critical current densities in MgB_2 tapes made by a scaleable nanocarbon addition route. *Applied Physics Letters*, 88(7):–, 2006.
- [70] P. Lezza, C. Senatore, and R. Flukiger. Improved critical current densities in B_4C doped MgB_2 based wires. *Superconductor Science & Technology*, 19(10):1030–1033, 2006.

- [71] A. Yamamoto, J. Shimoyama, S. Ueda, I. Iwayama, S. Horii, and K. Kishio. Effects of b_4c doping on critical current properties of mgb_2 superconductor. *Superconductor Science & Technology*, 18(10):1323–1328, 2005.
- [72] J. V. Marzik, R. J. Suplinskas, R. H. T. Wilke, P. C. Canfield, D. K. Finnemore, M. Rindfleisch, J. Margolies, and S. T. Hannahs. Plasma synthesized doped b powders for mgb_2 superconductors. *Physica C-Superconductivity and Its Applications*, 423(3-4):83–88, 2005.
- [73] C. E. Cunningham, C. Petrovic, G. Lapertot, S. L. Bud'ko, F. Laabs, W. Straszheim, D. K. Finnemore, and P. C. Canfield. Synthesis and processing of mgb_2 powders and wires. *Physica C*, 353(1-2):5–10, 2001.
- [74] H. M. Kim, S. S. Yim, K. B. Kim, S. H. Moon, Y. W. Kim, and D. H. Kang. Growth kinetics of mgb_2 layer and interfacial mgo layer during ex situ annealing of amorphous boron film. *Journal of Materials Research*, 19(10):3081–3089, 2004.
- [75] J. W. Elmer, T. A. Palmer, S. S. Babu, W. Zhang, and T. DebRoy. Phase transformation dynamics during welding of ti-6al-4v. *Journal of Applied Physics*, 95(12):8327–8339, 2004.
- [76] S. E. Offerman, N. H. van Dijk, J. Sietsma, S. Grigull, E. M. Lauridsen, L. Margulies, H. F. Poulsen, M. T. Rekveldt, and S. van der Zwaag. Grain nucleation and growth during phase transformations. *Science*, 298(5595):1003–1005, 2002.
- [77] P. Barnes. The use of synchrotron energy-dispersive diffraction for studying chemical-reactions. *Journal of Physics and Chemistry of Solids*, 52(10):1299–1306, 1991.
- [78] H. Giefers, F. Porsch, and G. Wortmann. Kinetics of the disproportionation of sno. *Solid State Ionics*, 176(1-2):199–207, 2005.
- [79] M. R. Sharafutdinov, B. P. Tolochko, and N. Z. Lyakhov. Usage of the synchrotron radiation diffraction for "in situ" kinetics study of the nickel tungstenate solid state synthesis. *Nuclear Instruments & Methods in Physics Research Section a-Accelerators Spectrometers Detectors and Associated Equipment*, 470(1-2):228–231, 2001.
- [80] U. Ruschewitz, C. Bahtz, and M. Knapp. On the kinetics of the formation of na_2pdc_2 . *Zeitschrift Fur Anorganische Und Allgemeine Chemie*, 629(9):1581–1584, 2003.

- [81] S. Shaw, C. M. B. Henderson, and S. M. Clark. In-situ synchrotron study of the kinetics, thermodynamics, and reaction mechanisms of the hydrothermal crystallization of gyrolite, $\text{Ca}_{16}\text{Si}_{24}\text{O}_{60}(\text{OH})_8 \cdot 14\text{H}_2\text{O}$. *American Mineralogist*, 87(4):533–541, 2002.
- [82] H. F. Poulsen, L. G. Andersen, T. Frello, S. Prantontep, N. H. Andersen, S. Garbe, J. Madsen, A. Abrahamsen, M. D. Bentzon, and M. von Zimmermann. In situ study of equilibrium phenomena and kinetics in a biscco ag tape. *Physica C-Superconductivity and Its Applications*, 315(3-4):254–262, 1999.
- [83] A. N. Baranov, V. L. Solozhenko, C. Lathe, V. Z. Turkevich, and Y. W. Park. Synchrotron radiation study of MgB_2 formation under high pressure. *Superconductor Science & Technology*, 16(10):1147–1151, 2003.
- [84] J. C. Grivel, R. Pinholt, N. H. Andersen, P. Kovac, I. Husek, and J. Homeyer. In situ investigations of phase transformations in Fe-sheathed MgB_2 wires. *Superconductor Science & Technology*, 19(1):96–101, 2006.
- [85] J. T. Blucher, U. Narusawa, M. Katsumata, and A. Nemeth. Continuous manufacturing of fiber-reinforced metal matrix composite wires - technology and product characteristics. *Composites Part A-Applied Science and Manufacturing*, 32(12):1759–1766, 2001.
- [86] B. A. Glowacki, M. Majoros, M. Vickers, J. E. Evetts, Y. Shi, and I. McDougall. Superconductivity of powder-in-tube MgB_2 wires. *Superconductor Science & Technology*, 14(4):193–199, 2001.
- [87] H. Kumakura, H. Kitaguchi, A. Matsumoto, and H. Hatakeyama. Upper critical fields of powder-in-tube-processed MgB_2/Fe tape conductors. *Applied Physics Letters*, 84(18):3669–3671, 2004.
- [88] H. Fang, S. Padmanabhan, Y. X. Zhou, and K. Salama. High critical current density in iron-clad MgB_2 tapes. *Applied Physics Letters*, 82(23):4113–4115, 2003.
- [89] W. Goldacker, S. I. Schlachter, B. Obst, and M. Eisterer. In situ MgB_2 round wires with improved properties. *Superconductor Science & Technology*, 17(9):S490–S495, 2004.
- [90] R. H. T. Wilke, S. L. Bud'ko, P. C. Canfield, D. K. Finnemore, and S. T. Hannahs. Synthesis of $\text{Mg}(\text{B}_{1-x}\text{C}_x)_2$ powders. *Physica C-Superconductivity and Its Applications*, 432(3-4):193–205, 2005.

- [91] A. P. Hammersley, S. O. Svensson, M. Hanfland, A. N. Fitch, and D. Hausermann. Two-dimensional detector software: From real detector to idealised image or two-theta scan. *High Pressure Research*, 14(4-6):235–248, 1996.
- [92] R. E. Carter. Kinetic model for solid-state reactions. *Journal of Chemical Physics*, 34(6):2010–&, 1961.
- [93] R.E. Honig and D.A. Kramer. Vapor pressure data for the solid and liquid elements. *RCA Rev.*, 30(2):285–305, 1969.
- [94] P. B. Entchev, D. C. Lagoudas, and J. C. Slattery. Effects of non-planar geometries and volumetric expansion in the modeling of oxidation in titanium. *International Journal of Engineering Science*, 39(6):695–714, 2001.
- [95] T. G. Nieh, Jeffrey Wadsworth, and Oleg D. Sherby. *Superplasticity in metals and ceramics*. Cambridge solid state science series. Cambridge University Press, Cambridge [England] ; New York, NY, USA, 1997.
- [96] Y. Shinoda, T. Nagano, H. Gu, and F. Wakai. Superplasticity of silicon carbide. *Journal of the American Ceramic Society*, 82(10):2916–2918, 1999.
- [97] K. R. Venkatachari and R. Raj. Superplastic flow in fine-grained alumina. *Journal of the American Ceramic Society*, 69(2):135–138, 1986.
- [98] G. D. Zhan, M. Mitomo, T. Nishimura, R. J. Xie, T. Sakuma, and Y. Ikuhara. Superplastic behavior of fine-grained beta-silicon nitride material under compression. *Journal of the American Ceramic Society*, 83(4):841–847, 2000.
- [99] M. Mitomo, Y. W. Kim, and H. Hirotsuru. Fabrication of silicon carbide nanoceramics. *Journal of Materials Research*, 11(7):1601–1604, 1996.
- [100] X. Z. Liao, A. Serquis, Y. T. Zhu, L. Civale, D. L. Hammon, D. E. Peterson, F. M. Mueller, V. F. Nesterenko, and Y. Gu. Defect structures in MgB_2 wires introduced by hot isostatic pressing. *Superconductor Science & Technology*, 16(7):799–803, 2003.
- [101] A. Serquis, X. Z. Liao, Y. T. Zhu, J. Y. Coulter, J. Y. Huang, J. O. Willis, D. E. Peterson, F. M. Mueller, N. O. Moreno, J. D. Thompson, V. F. Nesterenko, and S. S. Indrakanti. Influence of microstructures and crystalline defects on the superconductivity of MgB_2 . *Journal of Applied Physics*, 92(1):351–356, 2002.
- [102] A. Serquis, L. Civale, J. Y. Coulter, D. L. Hammon, X. Z. Liao, Y. T. Zhu, D. E. Peterson, F. M. Mueller, V. F. Nesterenko, and S. S. Indrakanti. Large field generation

- with a hot isostatically pressed powder-in-tube MgB_2 coil at 25 k. *Superconductor Science & Technology*, 17(10):L35–L37, 2004.
- [103] X. P. Zhang, Z. S. Gao, D. L. Wang, Z. G. Yu, Y. W. Ma, S. Awaji, and K. Watanabe. Improved critical current densities in MgB_2 tapes with ZrB_2 doping. *Applied Physics Letters*, 89(13):–, 2006.
- [104] P. Kovac, I. Husek, and T. Melisek. Transport currents of two-axially rolled and post-annealed MgB_2/Fe wires at 4.2 k. *Superconductor Science & Technology*, 15(9):1340–1344, 2002.
- [105] Chemical Rubber Company. *CRC handbook of chemistry and physics*, volume 58th ed. (1977/78)- . CRC Press, Cleveland, 1977.
- [106] S. Brutti, G. Balducci, G. Gigli, A. Cicciola, P. Manfrinetti, and A. Palenzona. Thermodynamic and kinetic aspects of decomposition of MgB_2 in vacuum: Implications for optimization of synthesis conditions. *Journal of Crystal Growth*, 289(2):578–586, 2006.
- [107] Z. Y. Fan, D. G. Hinks, N. Newman, and J. M. Rowell. Experimental study of MgB_2 decomposition. *Applied Physics Letters*, 79(1):87–89, 2001.
- [108] J. R. Ramberg, C. F. Wolfe, and W. S. Williams. Resistance of titanium diboride to high-temperature plastic yielding. *Journal of the American Ceramic Society*, 68(3):C78–C79, 1985.
- [109] J. R. Ramberg and W. S. Williams. High-temperature deformation of titanium diboride. *Journal of Materials Science*, 22(5):1815–1826, 1987.
- [110] J. S. Haggerty and D. W. Lee. Plastic deformation of ZrB_2 single crystals. *Journal of the American Ceramic Society*, 54(11):572–&, 1971.
- [111] J. J. Melendez-Martinez, A. Dominguez-Rodriguez, F. Monteverde, C. Melandri, and G. de Portu. Characterisation and high temperature mechanical properties of zirconium boride-based materials. *Journal of the European Ceramic Society*, 22(14-15):2543–2549, 2002.
- [112] I. W. Chen and L. A. Xue. Development of superplastic structural ceramics. *Journal of the American Ceramic Society*, 73(9):2585–2609, 1990.
- [113] R. A. Ribeiro, S. L. Bud’ko, C. Petrovic, and P. C. Canfield. Effects of stoichiometry, purity, etching and distilling on resistance of MgB_2 pellets and wire segments. *Physica C-Superconductivity and Its Applications*, 382(2-3):194–202, 2002.

- [114] I. Ahmad and J. M. Barranco. Reinforcement of magnesium with boron and tantalum filaments. *Metallurgical Transactions*, 4(3):793–797, 1973.
- [115] T. B. Massalski and ASM International. *Binary alloy phase diagrams*. ASM International, Materials Park, Ohio, 2nd edition, 1990.
- [116] J. D. DeFouw and D. C. Dunand. In situ synthesis of superconducting MgB_2 fibers within a magnesium matrix. *Applied Physics Letters*, 83(1):120–122, 2003.
- [117] R. J. Suplinskas. Personal communication with d.c. dunand. 2003.
- [118] R. A. Ribeiro, S. L. Bud'ko, C. Petrovic, and P. C. Canfield. Carbon doping of superconducting magnesium diboride. *Physica C-Superconductivity and Its Applications*, 384(3):227–236, 2003.
- [119] D. P. Whittle and J. Stringer. Improvements in high-temperature oxidation resistance by additions of reactive elements or oxide dispersions. *Philosophical Transactions of the Royal Society of London Series a-Mathematical Physical and Engineering Sciences*, 295(1413):309–&, 1980.
- [120] S. X. Dou, X. L. Wang, J. Horvat, D. Milliken, A. H. Li, K. Konstantinov, E. W. Collings, M. D. Sumption, and H. K. Liu. Flux jumping and a bulk-to-granular transition in the magnetization of a compacted and sintered MgB_2 superconductor. *Physica C*, 361(2):79–83, 2001.
- [121] J. C. Williams and G. Garmong. Microstructural studies of a ni-w directionally solidified eutectic composite. *Metallurgical Transactions a-Physical Metallurgy and Materials Science*, 6(9):1699–1709, 1975.
- [122] D. Souptel, G. Behr, W. Loser, W. Kopylov, and M. Zinkevich. Crystal growth of MgB_2 from mg-cu-b melt flux and superconducting properties. *Journal of Alloys and Compounds*, 349(1-2):193–200, 2003.
- [123] John Crank. *The mathematics of diffusion*. Clarendon Press, Oxford, 2d edition, 1975.

APPENDIX A

Java Codes for Synchrotron Data Analysis**A.1. Background Subtraction**

This program was designed to perform background subtraction on data collected from in situ studies of reaction kinetics in the formation of MgB₂ from powders in Chapter 2 and from fibers in Chapters 5 and 6. After conversion to 1D, a file from the ramp up in temperature, after Mg melts, is chosen to be the background and is subtracted from the rest of the files in the data set. The converted files were then analyzed with JADE powder diffraction software as discussed in the text.

Program: FileBaseConvert.java

Java coded by Scott Oppenheimer

```
import java.io.*;
import java.util.*;

public class FileConvertBase {
    public static void main(String[] args) throws IOException {
//error check the inputs
if (args.length != 3)
System.out.println("Usage: [input dir] [output dir] [basefile]");
else {
```

```
String c = new String();
String temp = new String();

//take the inputs and get them into usable formats
File dir = new File(args[0]);
String[] files = dir.list();
//Get the baseline file
BufferedReader bIn = new BufferedReader(new FileReader(args[0]+"\\ "+args[2]));
float[] baseAngles = new float[1500];
int[] baseCounts = new int[1500];
int entry = 0;

bIn.readLine();
bIn.readLine();
bIn.readLine();
bIn.readLine();

while ((c = bIn.readLine()) != null) {
StringTokenizer st = new StringTokenizer(c);

baseAngles[entry] = Float.parseFloat(st.nextToken());
st.nextToken(); //eat random middle colum
```

```
baseCounts[entry] = Integer.parseInt(st.nextToken());
entry = entry + 1;
}

//for each file
for(int x=0; x<files.length; x++) {
entry = 0;
System.out.println("Working on: " +files[x]);

BufferedReader in = new BufferedReader(new FileReader(args[0]+"\\\\"+files[x]));
FileWriter out = new FileWriter(args[1]+"\\\\"+"sub"+files[x]);

float[] angles = new float[1500];
int[] counts = new int[1500];

out.write(in.readLine()+'\r'+'\n');
out.write(in.readLine()+'\r'+'\n');
out.write(in.readLine()+'\r'+'\n');
out.write(in.readLine()+'\r'+'\n');

//read the file, find the min, put into arrays
while ((c = in.readLine()) != null) {
```

```
StringTokenizer st = new StringTokenizer(c);

angles[entry] = Float.parseFloat(st.nextToken());
st.nextToken(); //eat random middle colum
counts[entry] = Integer.parseInt(st.nextToken());
entry = entry + 1;
}

//Subtract baseline
for (int i=0;i<entry;i++) {
counts[i] = counts[i] - baseCounts[i];
if (counts[i] < 0)
counts[i] = 0;
}

//output the file
for (int i=0;i<entry;i++) {
String outputAngle = new String(Float.toString(angles[i]));
out.write(outputAngle);
out.write('\t');
String outputCounts = new String(Integer.toString(counts[i]));
out.write(outputCounts);
out.write('\r');
out.write('\n');
}
```

```
        in.close();
        out.close();
    }
} //else
}
}
```

A.2. Combining XRD Peak Analysis Files

After background subtraction and diffraction peak analysis, each file corresponding to reaction time has its own peak analysis file. This program combines the peak analysis files into one file where spreadsheet programs can be used to sort and select the appropriate peaks for generation of degree of reaction vs. time plots.

Program: DataFiler.java Java coded by Scott Oppenheimer

```
import java.io.*;
import java.util.*;

public class DataFiler {
    public static void main(String[] args) throws IOException {
        System.out.println(args[0]);

        File dir = new File(args[0]);
```

```
String[] files = dir.list();

FileWriter out = new FileWriter("AllData.data");
String c = new String();

for(int x=0; x<files.length; x++) {
System.out.println("Working on "+files[x]);

BufferedReader in = new BufferedReader(new FileReader(args[0]+"\\\\"+files[x]));

in.readLine();
in.readLine(); //Eat first 8 lines
in.readLine();
in.readLine();
in.readLine();
in.readLine();
in.readLine();
in.readLine();

while ((c = in.readLine()) != null) {
out.write(files[x]);
out.write('\t');
out.write(c);
```

```
out.write('\r');
out.write('\n');
}
in.close();
}
    out.close();
}
}
```

APPENDIX B

Carter Style Derivation of Film and Cylinder Reactions**B.1. Film Reaction**

Following Carter [92] for the reaction model of a sphere of A with B, the model for a film of thickness r_0 is derived below. At any time the amount of unreacted A in the film is calculated as

$$(B.1) \quad Q_A = r_1 L^2$$

where r_1 is the thickness of unreacted A and L are other dimensions of a square film. The rate of change of Q_A for a film is given by Crank [123] as,

$$(B.2) \quad \frac{dQ_A}{dt} = \frac{-kL^2}{r_2 - r_1}$$

where k is the reaction rate constant, r_2 is the total film thickness of reactant plus product layers. Differentiating the equation B.1 with respect to time and setting equal to equation B.2,

$$(B.3) \quad \frac{dr_1}{dt} = \frac{-k}{r_2 - r_1}$$

Substituting $r_2 = zr_0 + r_1(1 - z)$ where z is the volume expansion coefficient,

$$(B.4) \quad kdt = z(r_1 - r_0) dr_1$$

Integrating both sides of the equation,

$$(B.5) \quad kt = \frac{z(r_2^2 - r_1^2)}{2} - zr_0(r_1 - r_0)$$

Substitution $r_1 = (1 - x)r_0$ where x is the degree of reaction, the final equation is,

$$(B.6) \quad kt = \frac{zr_0^2x^2}{2}$$

Additionally, substituting $x = \frac{h}{zr_0}$ where h is the thickness of the film reaction product, the thickness h is related to the reaction rate constant k as,

$$(B.7) \quad h = \sqrt{2zkt}$$

B.2. Cylinder Reaction

Following Carter [92] for the reaction model of a sphere of A with B, the model for a cylinder of initial radius r_0 is derived below. At any time the amount of unreacted A in the cylinder is calculated as,

$$(B.8) \quad Q_A = \pi r_1^2 L$$

where r_1 is the radius of unreacted A and L is the length of the cylinder. The rate of change of Q_A for a cylinder is given by Crank [123] as

$$(B.9) \quad \frac{dQ_A}{dt} = \frac{-2\pi k}{\ln\left(\frac{r_2}{r_1}\right)}$$

where k is the reaction rate constant, r_2 is the total radius of reactant plus product layers. Differentiating equation B.8 with respect to time and setting equal to the equation B.9,

$$(B.10) \quad r_1 \frac{dr_1}{dt} = \frac{-k}{\ln\left(\frac{r_2}{r_1}\right)}$$

Substituting $r_2 = \sqrt{zr_0^2 + r_1^2(1-z)}$ where z is the volume expansion coefficient,

$$(B.11) \quad -k dt = r_1 \ln\left(\frac{\sqrt{zr_0^2 + (1-z)r_1^2}}{r_1}\right) dr_1$$

After integration and substitution of $r_1 = r_0\sqrt{1-x}$, the final equation relating the reaction rate constant to the degree of reaction in terms of the initial radius and volume expansion coefficient is,

$$(B.12) \quad -kt = \frac{r_0^2 \left(x \ln\left(\frac{1-x+zx}{1-x}\right) + zx \ln\left(\frac{1-x}{1-x+zx}\right) + z \ln\left(\frac{1}{1-x}\right) + \ln\left(\frac{1-x}{1-x+zx}\right) \right)}{4(z-1)}$$

Additionally, the degree of reaction is found from the measured thickness of the reaction layer $h = r_2 - r_1$ starting with $r_2 = \sqrt{zr_0^2 + r_1^2(1-z)}$ as shown above and substituting in $r_2 = h + r_1$ to find

$$(B.13) \quad (h + r_1)^2 = zr_0^2 + r_1^2(1-z)$$

Then $r_1^2 = (1-x)r_0^2$ is substituted in and the equation rearranged to show the quadratic relation

$$(B.14) \quad 2h(\sqrt{1-x})r_0 - zxr_0^2 + h^2 = 0$$

which is solved to form Equation 5.2 in Chapter 5 to convert reaction layer thickness to degree of reaction for a cylinder.

$$(B.15) \quad x = \frac{h \left(h + \left(\frac{-2h + 2\sqrt{h^2 - zh^2 + z^2 r_0^2}}{z} \right) \right)}{z r_0^2}$$